Final Scientific/Technical Report

Title: *Catalyst layer design, manufacturing and in-line quality control*

PI: Radenka Maric[1]

Co-PIs: Katherine Ayers,[2] Andrew Wagner,[3] Stoyan Bliznakov[1]

[1]University of Connecticut, Storrs, CT 06269

[2]Nel Hydrogen, Wallingford, Connecticut 06492

[3]Mainstream Engineering Corporation, Rockledge, FL 32955

1. Introduction.

The main goal of this project is to demonstrate the capability of the Reactive Spray Deposition Technology (RSDT) to fabricate large-scale membrane electrode assemblies (MEAs) for proton exchange membrane water electrolyzers (PEMWEs) that meet and exceed the DOE cost reduction, and activity and durability performance targets. RSDT is an innovative flame-assisted dry-spraying method that allows fast and facile manufacturing of high-performance large-scale nanostructured catalyst layers for MEAs for PEMWEs. The RSDT is a one-step, continuous and open-to-air manufacturing process that combines the synthesis and deposition of the catalyst directly on PEM membrane. Thus, starting from cost-effective organic chemical precursors, the MEAs are fabricated in hours, avoiding expensive and time-consuming slurry deposition and drying steps that the state-of-the-art electrode manufacturing processes currently use. Important advantages of the RSDT method include: (1) scalability for fabrication of large-scale (up to 1000 cm^2) MEAs, and (2) adaptiveness to roll-to-roll manufacturing process which has been successfully proved in this project. In addition, the RSDT offers precise engineering of desired composition and structure of the electrodes at nanoscale level. In the frame of this project, the team has successfully developed and integrated in-line optical quality control and in-situ laser diagnostics systems in the RSDT setup that ensure in-situ precise control of the electrode's composition, thickness, porosity, and homogeneity.

This technology uses low-cost methane, propane, and oxygen as pilot gases and has extremely low electric power consumption (less than 1 kW), which reduces the cost of electrode fabrication by 60%. More importantly, RSDT enables effective control of the material properties via manipulation of the processing conditions. For example, by adjusting the precursor concentration, the synthesized catalysts can be finetuned to the desired surface morphology and particle size distribution. Also, no hazardous waste is generated from this synthesis route due to the complete combustion of the organic precursors. By using this methodology, we have fabricated MEAs with one order of magnitude lower platinum group metals (PGM) loadings in the catalyst layers of the MEAs for PEMWEs and demonstrated equivalent activity performance with the state-of-the-art commercial MEAs operating at conditions, typical for industrial electrolyzers. Furthermore, a stable performance for over 5000 hours has been successfully demonstrated with the RSDT fabricated MEAs. Another unique capability of the RSDT that has been demonstrated for the first time in this project is its ability to fabricate single and duo recombination layers (RLs) on large scale, which are integrated within the volume of the Nafion® membrane. The RSDT fabricated RLs have been proved to efficiently suppress the hydrogen crossover in the MEAs, and hence eliminate the safety concerns related to the PEMWEs.

The project has been executed in two steps, corresponding to two budget periods. In budget period 1 (BP1), we have demonstrated the capability of the RSDT to fabricate subscale MEAs (active area of 86 cm^2) with the desired properties. The RSDT conditions for the fabrication of anode catalyst layers (CLs), as well as the Pt/C cathode CLs, and Pt RLs, have been optimized, and stable performance for over 5000 hours have been achieved. We have demonstrated that the RSDT fabricated MEAs with Ir and Pt loading in their CLs of less than 0.3 mg_{PGM}/cm^2 have the same activity and durability performance as the commercial MEAs with one order of magnitude higher PGM loadings (3 mg_{PGM}/cm^2) in each catalyst layer. In this BP1, we demonstrated a stable performance for over 1,000 hours on as fabricated 86 cm^2 MEAs and achieved the Go/No-Go decision of the project. In budget period 2 (BP2), the team applied the accumulated knowledge to successfully scale up the manufacturing process, and fabricated MEAs with geometric area of 680 cm^2, which is the desired size that fits the MW-scale PEMWE stack, fabricated by our industrial collaborator - Nel Hydrogen. Also, in this BP we demonstrated excellent activity performance of the large-scale MEAs with 10x lower PGM catalyst loadings, and durability of over 1000 hours. The specific objectives for both budget periods are as follows:

Budget Period 1:

- Development of a membrane coating to decrease hydrogen permeation. (Accomplished)
- Demonstration of half and full 86 cm^2 membrane electrode assembly (MEA) performance within 50 mV of baseline commercial electrodes at 1.8 A/cm^2, 2.1 V. (Accomplished)
- Operation of half and full 86 cm^2 MEAs for over 1000 hours. (Accomplished)
- Integration of RSDT electrodes into a single MEA. (Accomplished)

Budget Period 2:

- Determine the optimal Pt and Ir concentrations by performing in-situ laser measurements in the RSDT flame. (Accomplished)
- Optimize the cathode, anode, and recombination layer and scale up the MEAs to 680 cm^2 active area. (Accomplished)
- Demonstrate comparable performance of the full scale 680 cm^2 RSDT MEA with the 86 cm^2 MEA. (Accomplished)
- Demonstrate durability of >1000 h with the optimized cathode, anode, and recombination layers for full-scale 680 cm^2 MEAs (Accomplished)
- Install the quality control equipment on RSDT II and collect in-situ optical images during the fabrication of 680 cm^2 MEAs at real time and verify the thickness, composition, and catalyst loading of the deposited catalyst layers. (Accomplished)

All tasks, milestones, and objectives of the project have been successfully accomplished. The outcomes of the project include: (i) successful development of RSDT deposition parameters and formulations that achieve reduction of iridium and platinum loadings from 3.3 mg/cm^2 to 0.2 - 0.3 mg_{PGM}/cm^2, (ii) innovative design of single and duo RLs to substantially reduce the H_2 crossover, (iii) equipment designs capable of producing multiple layers in registration, and measurement

parameters adapted for electrolysis MEAs, (iv) integrated in-line quality control optical system, and in-situ laser diagnostics system that offer the unique precise control of the electrodes' composition, thickness, porosity, and homogeneity.

In addition to that, the team performed comprehensive pre- and post- test characterization of the RSDT fabricated MEAs and identified the governing mechanisms contributing to performance loss in PEMWEs. Based on the findings of this project, the team identified and demonstrated novel pathways for further improvement of the performance of all PEMWEs.

2. Accomplishments during budget period 1.

The emphasis of the research and development activities during BP1 has been on defining and optimizing the RSDT deposition parameters that result in the fabrication of anode and cathode CLs with ultra-low PGM catalyst loading and high activity and durability performance. In addition, the parameters for Pt RL have been optimized to achieve effective H_2 crossover suppression, below 10 % of the Lower Flammability Level (LFL).

2.1 RSDT fabrication of Pt recombination layers directly on Nafion^{tm} N117 membranes.

A set of Pt RLs has been fabricated from precursor solutions prepared from $Pt(acac)_2$ dissolved in a mixture of xylene, acetone, and liquid propane . The precursor solution was sprayed from the primary nozzle into the methane/oxygen flame is described in our previously published papers.[1–4] After the flame, the synthesized Pt nanoparticles are quenched in an air quench and deposited directly on a Nafion^{tm} N117 membrane that is mounted in a specially designed holder and attached to an XYZ linear drive that moves the substrate holder in a software-controlled pathway to ensure homogeneous distribution of the deposit.[2–6]By changing the deposition parameters, the concentration of the precursor solution, and the time for deposition, we can precisely control the particle size, morphology, and the amount and thickness of the deposited RLs.

Figure 1(a) shows an example of measuring the Pt loading across the deposited area of 137 cm^2. The dashed circle indicates the active area for MEA testing. The deposited area is designed to be larger than the active area so that there is room for alignment in the assembly of MEA test. The Pt loadings at different locations as a function of deposition time are presented in Figure 1(b). The quality of linear fitting is shown in Figure 1(c) where all R-square values are above 0.95. This suggests that the Pt loading scales linearly with deposition time when all other process parameters are fixed. It is noted that lower Pt loadings were measured at the edges than at the center. This is due to the edge effect of the sample mask which is used to determine the deposition area. Since only the center region is used in the MEA test, low Pt loading at the edge is not a concern for the initial measurements. Additional tests with a modified mask and modified spray pattern have been also conducted, and this problem was resolved in the latter stages of the project.

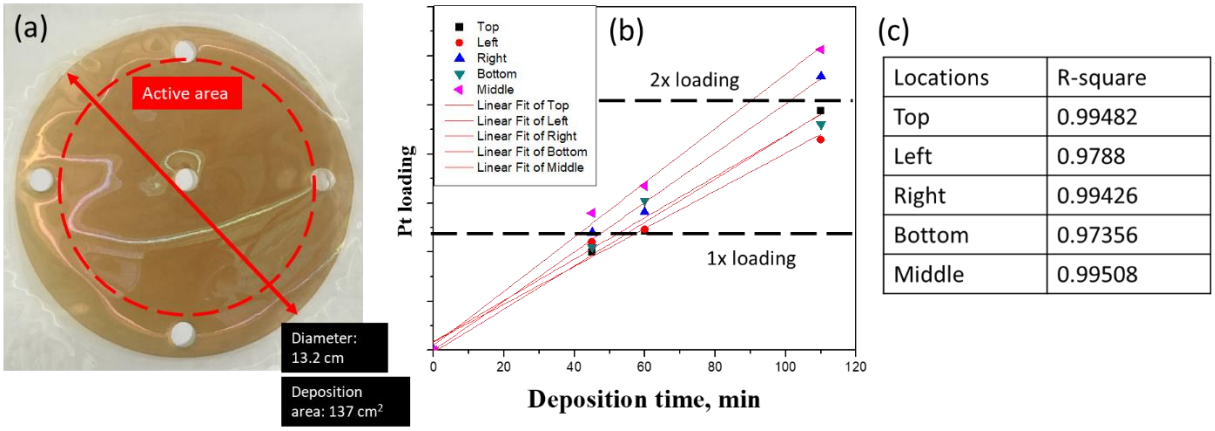

Locations	R-square
Top	0.99482
Left	0.9788
Right	0.99426
Bottom	0.97356
Middle	0.99508

Figure 1. (a) An example of measuring the Pt loading across a recombination layer. Five circles of 0.95 cm diameter were punched out for ICP analysis. The dashed circle indicates the active area used in MEA test. (b) Pt loading as a function of deposition time at different locations. (c) Summary of the linearity at different locations.

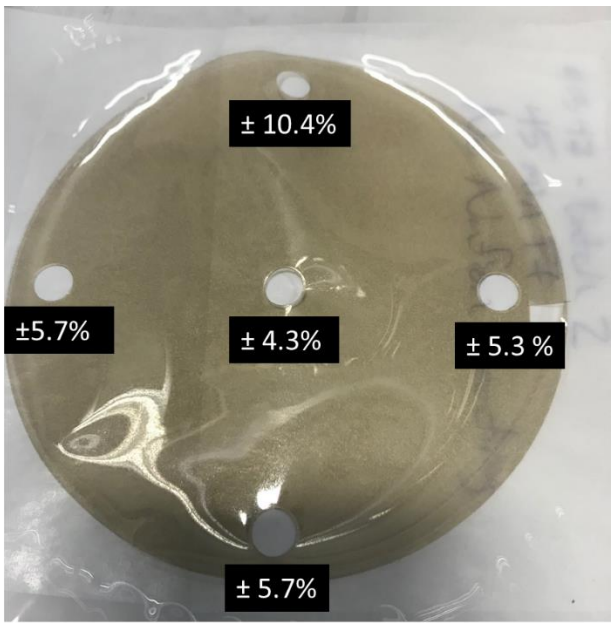

Figure 2. Variance of Pt loading for three Pt recombination layers fabricated independently. The Pt loading is measured at five locations.

Figure 2 shows the repeatability and variance of Pt loading of three Pt recombination layers fabricated independently. The standard deviation is 4.3% at the center and 5-6% at left, right, and bottom locations. The top location shows a standard deviation of 10.4% larger than that of other locations. Repeatable and controllable fabrication process is advantageous for repeatable test results, and we performed the same characterization of the full RSDT CCM to verify the uniformity of the fabrication process.

2.1.1 Verification of the performance of the recombination layers

To verify the effectiveness of H_2 suppression of the recombination layers (RLs), as fabricated RSDT Pt RLs are tested with lower Pt loading and short-term stability (500-hour operation). The crossover mitigated membrane architecture is based on a 3-layer design in which the RSDT deposited Pt recombination layer is sandwiched between N117 and N111 membranes. A lamination procedure is developed to combine the 3-layer structure into one component in order to improve the contact between the Pt layer and membrane before a Nafion top-coating by the RSDT method has been developed later in the program. The lamination procedure has been initially used for full CCM fabrication to meet the BP1 milestones and the Go/No-go decision.

Effect of Pt loading in the recombination layer on the H2 crossover.

CCMs (Catalyst Coated Membranes) with various Pt loading in their RLs have been tested for their effectiveness for H_2 crossover suppression. Figure 3 shows a comparison of the H_2 crossover measurements for 4 CCMs fabricated with a relative Pt in their RLs of 0, 0.2x, 1x and 2x times of the baseline RL. All Pt RLs have been fabricated by direct RSDT deposition of Pt nanoparticles directly on N117 membranes. Based on the SEM (Scanning Electron Microscopy) images collected on the samples, the thickness of as fabricated RLs is estimated to be between 100 and 200 nm, and the distribution of Pt particles across the cross-section of the sample is uniform. As shown in Figure 3 for the recombination layer with 0.2x Pt loading, the measured LFL is 31% (1.24% of H in O_2) at 0.58 A/cm^2. The crossover value is higher than the 1x Pt loading but lower than the unmitigated membrane. The optimum Pt loading is determined to be 1x for effective recombination and the LFL values meet the hydrogen crossover requirement of <10% LFL. It is found that the Pt loading in the RLs with optimized performance is lower than 0.2mg$_{Pt}$/cm^2.

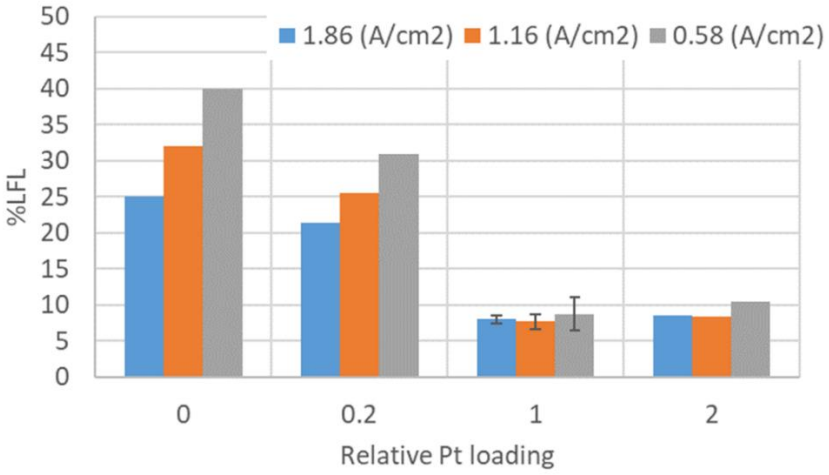

Figure. 3: Concentration of hydrogen in oxygen relative to the lower flammability limit (LFL) measured at three current densities. The recombination layer deposited on N117 was assembled with an N111 membrane and with standard anode and cathode gas diffusion electrodes (GDEs). The relative Pt loading in the recombination layer is indicated on the x-axis. The active area of the MEA is 86 cm^2, and the test conditions are 50^{o}C cell temperature and 400 psi differential pressure.

Short-term stability test.

A CCM fabricated with a membrane with 1x Pt loading in the RL, has been tested for 573 hours to determine the short-term stability of the recombination layer (Figure 4). The polarization curves taken at different time intervals are consistent and only a marginal variation in cell voltages, 2.097 ± 0.011 V was noticed at 2 A/cm^2. The cell performance has also been evaluated for hydrogen crossover before and after the durability test and no significant difference in % LFL values (Figure 5) has been detected. It is worth noting that the recombination layer was deposited with no ionomer to bind the Pt nanoparticles. The stack compression load kept the recombination layer held in place between N117 and N111. Overall, the short-term stability of the recombination layer is not impacted by the steady-state operation and the crossover %LFL values met the project requirement of <10% at the three current densities evaluated.

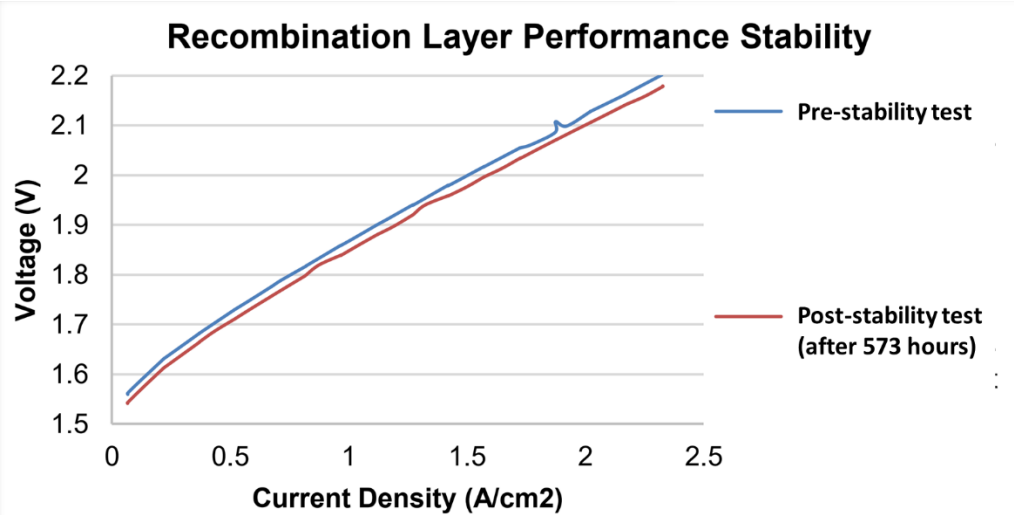

Figure. 4: Polarization curves were taken at different time intervals for an MEA with 1x recombination Pt loading. Standard GDEs were used for both anode and cathode with 3 ± 0.3 mg_{PGM}/cm^2. The active area of the MEA is 86 cm^2, and the test was conducted at 50°C cell temperature and operated at a differential pressure of 400 psi.

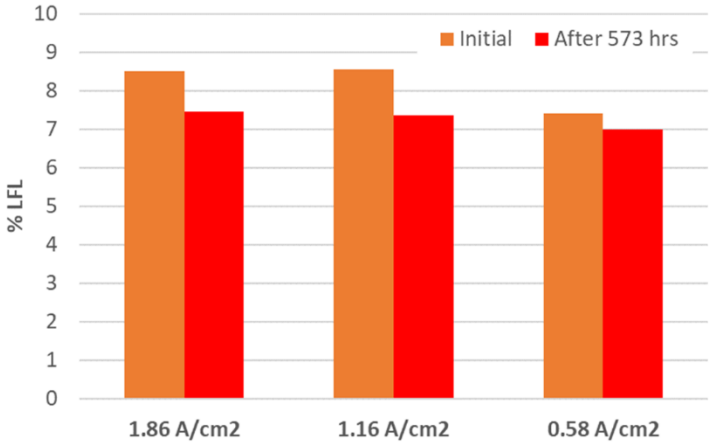

Figure. 5: Concentration of hydrogen in oxygen relative to the LFL measured at three current densities before and after the durability test.

Lamination procedure for the 3-layer crossover-mitigated membrane.

The 3-layer crossover-mitigated membrane, namely, N117 membrane, Pt recombination layer, and N211 membrane, are laminated to form a one-piece robust substrate for catalyst layer deposition. In addition, lamination improves the contact between the Pt RL and the membrane and can potentially reduce leak and ohmic resistance.

The lamination procedure is modified based on a MEA lamination procedure used for PEMFC (Polymer Electrolyte Membrane Fuel Cells) application. Key parameters are summarized in Table 1. Temperature is plotted as a function of the time in Figure 6 to demonstrate the thermal history of the 3-layer crossover-mitigated membrane during lamination.

Table 1 Lamination parameters

Items	Parameters
Target temperature (°C)	130
Target temperature setpoint (°C/°F)	137.8/280
Temperature ramp-up time (min)	48
Temperature dwell time (min)	3
Ramp-up load (lbs.)	5000 ± 1000
Dwell load (lbs.)	5000 ± 500
Sample size (Pt on N117 membrane, inch)	7.5*7.5
N211 membrane size (inch)	7.3*7.3
Pre-treatment (to improve adhesion)	Wipe the non-active area of recombination layer with Kimwipe damped with 5wt% Nafion® before lamination
Post-treatment (to remove wrinkles)	After lamination process, sample is assembled with substrate holder and put in vacuum oven at 100 C for 30 mins.

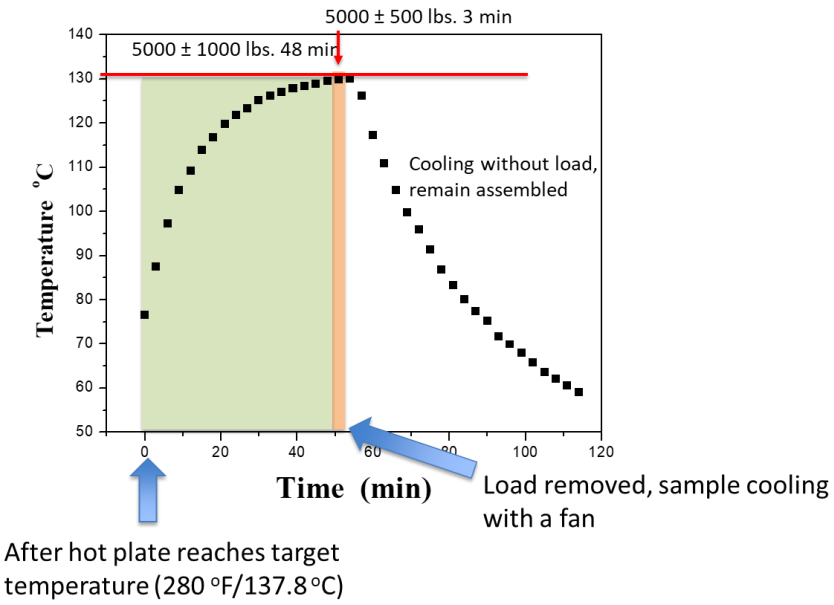

Figure 6. Temperature-time profile during the lamination process (the calibration curve).

The recombination layer before (Pt on N117 membrane) and after (3-layer combination) are presented in Figure 7. The active area is visually homogeneous after lamination. The change of color from yellow/brown to dark gray is most likely due to light refraction after a piece of thin N211 membrane is placed on top of the Pt layer.

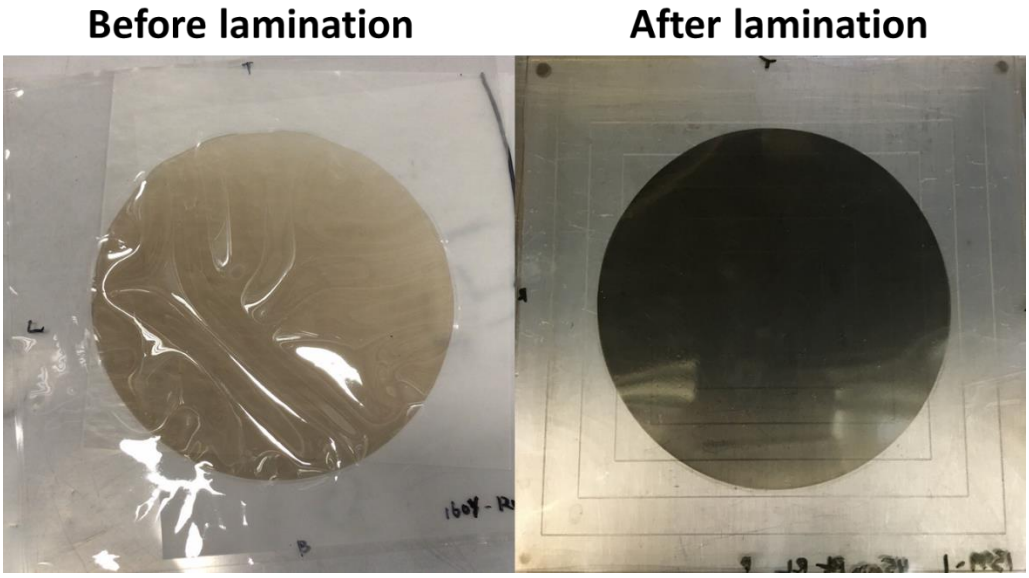

Figure 7. Photos of Pt recombination layer before and after lamination.

2.2 Long-term electrolyzer operation for full RSDT CCM at 86 cm^2 scale

After establishing an RSDT procedure for the fabrication of the Pt recombination layer with optimal Pt loading and proving its effectiveness and durability, five CCMs with recombination layer incorporated (denoted as full RSDT CCMs) were fabricated. Two of the CCMs were delivered and tested at Nel Hydrogen. The other three CCMs are used as backup samples for the long-term stability test. In addition, the RSDT electrode fabrication procedures have been optimized to improve the uniformity, thickness, and catalyst loading in the catalysts' layers.

2.2.1. Full RSDT catalyst coated membrane (CCM) development and evaluation.

Two full RSDT CCMs with a 5-layer architecture, Pt-C/N117/Pt RL/N211/IrOx have been fabricated by the RSDT method. The fabrication process is realized in several steps. First, Pt recombination layer is deposited on one side of the N117 membrane and then laminated with N211 membrane, so that the RL is held between N117 and N211 membranes. Then, Pt together with carbon support and ionomer, sprayed from the secondary nozzles, is deposited on the side of N117 membrane as the cathode catalyst layers.[1] After that IrOx/Nafion^{tm} layer is deposited on the side of N211 membrane as an anode catalyst layer, making a full CCM.[7] Verification of catalyst loading, and electrode thickness/morphology has been performed after finding the optimal deposition parameters for each of the deposition steps.[7] Furthermore, the anode and cathode fabrication procedures are improved with a modified design of the sample mask and deposition path/area to improve the uniformity of the active area.[1]

The two full CCMs were tested in a separate single-cell hardware and the high-frequency resistance of the two MEAs show consistent ohmic resistance values of 0.258 and 0.251 ohm-cm^2. The polarization curves, measured in the current range between 0 and 2.3 A/cm^2 are presented in Figure 8. However, compared to the reference MEA, Pt-GDE/N117/Pt RL/N11/IrOx-GDE, assembled with commercial anode and cathode with high PGM loading (3 mg$_{PGM}$/cm^2), the cell voltages for the two full RSDT fabricated CCMs at current densities above 1.2 A/cm^2 increases with increasing current densitie. This is attributed to a mass transport limitation of reactant/product in the MEA. Further characterizations of the electrode microstructure (pre- and post-test) and testing on the CCM with varying operating conditions such as water flow rate and differential pressure has been performed and the performance improvement has been achieved in the next RSDT fabricated CCMs.[8]

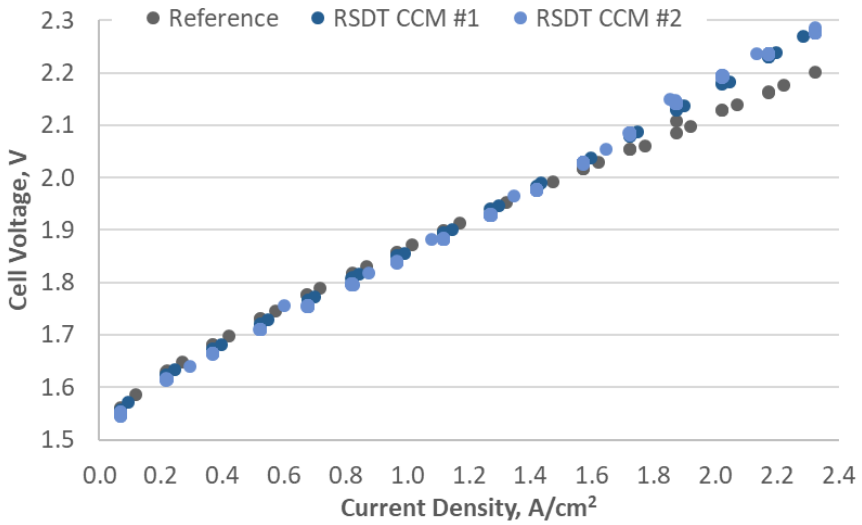

Figure 8. Polarization curves for RSDT full CCMs with estimated Pt and IrOx loadings are 0.2 mg$_{PGM}$/cm^2 per electrode. The active area of the MEA is 86 cm^2, and the test was conducted at 50^{o}C cell temperature and operated at a differential pressure of 400 psi. The reference sample is a proprietary MEA of Nel Hydrogen with H_2 crossover mitigation.

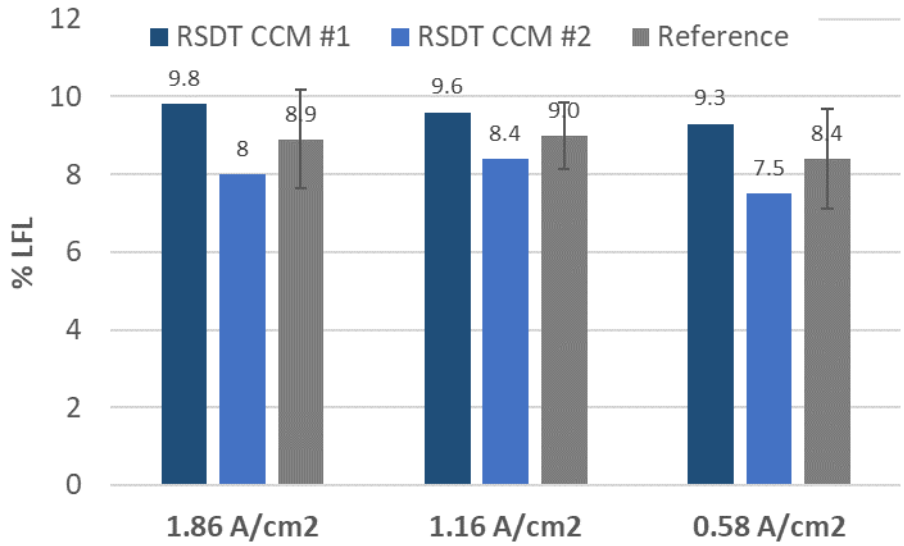

Figure 9. The concentration of hydrogen in oxygen relative to the LFL is measured at three current densities. The average values of the three measurements at each current density are labeled with the error bars representing +/- one standard deviation for the reference MEA. The active area of the MEA is 86 cm^2, and the test conditions are 50 ^oC cell temperature and 400 psi differential pressure. The reference sample is a proprietary MEA of Nell Hydrogen with H_2 crossover mitigation.

The crossover measurements performed for the two full CCMs also show reproducible %LFL values (Figure 9) and the variations between them, which is an average of 3 MEAs, are comparable to the reference. The two full CCMs fabricated by the RSDT, are with consistent performance and demonstrated the advantages of the RSDT deposition process to make low-loaded electrodes (0.3 mg_{PGM}/cm^2) for water electrolyzers.

2.2.2. Comprehensive characterizations of the RSDT fabricated catalyst materials and electrodes.

Physical characterizations of catalyst loading, and electrode morphology imaging are performed to verify the fabrication procedure and the quality of the RSDT fabricated CCMs. In addition, the structure of the recombination layer and its interface with Nafion^{tm} membrane are examined with transmission electron microscopy (TEM).

Catalysts loading measurements

The platinum and iridium loadings were measured by ICP at various locations of the active area. Samples from various locations were cut from the RSDT fabricated CCM, as is evident from Figure 10, and were subjected to ICP analysis. The estimated average platinum loading across the x-direction in the cathode is 0.2146 mg/cm^2 with a standard deviation of 0.025 mg/cm^2 or 11.7%. Across the y-direction, the average platinum loading is 0.1961 mg/cm^2 with a standard deviation of 0.030 mg/cm^2 or 15.3%. It is noted that the left and bottom of the active area shows lower Pt loading the average.

A similar quantitative analysis has been performed for the anode catalyst layer. Figure 11 shows that for the anode, the average iridium loading across the x-direction is 0.1917 mg/cm^2 with a standard deviation of 0.017 mg/cm^2 or 9.1%. Across the y-direction, the average platinum loading is 0.1877 mg/cm^2 with a standard deviation of 0.009 mg/cm^2 or 4.8%. The uniformity of

iridium loading is better compared to that of platinum loading. Note that the standard deviation across various locations reflects a combination of the variation during fabrication and sample preparation for ICP analysis.

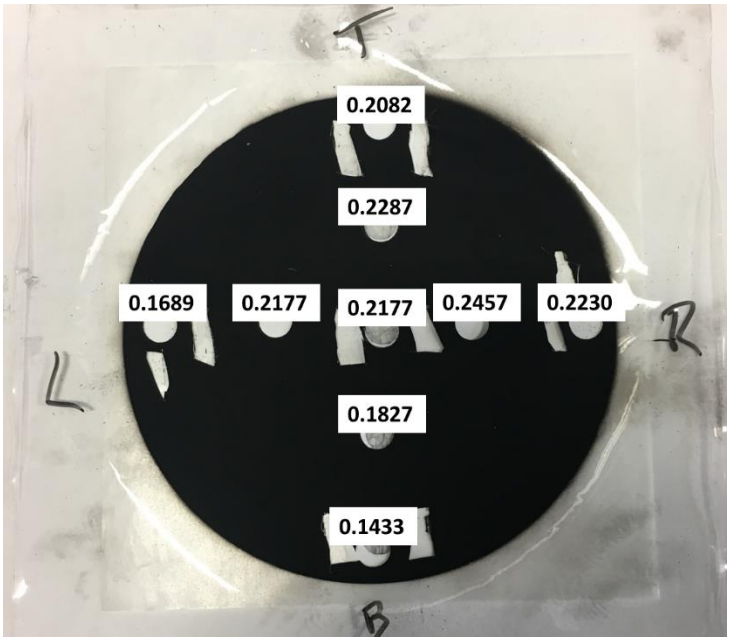

Figure 10. Cathode platinum loading distribution across the active area.

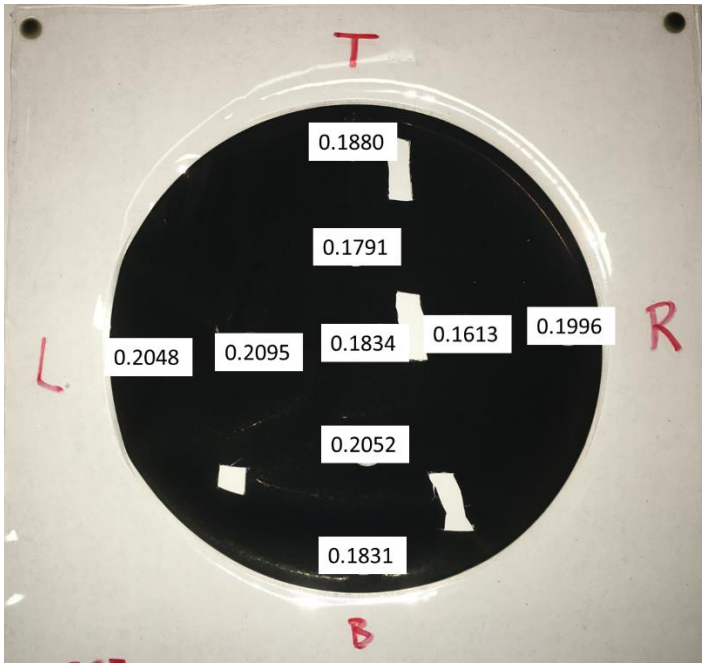

Figure 11. Anode iridium loading distribution across the active area.

Characterization of the electrode thickness and morphology

The cathode CL is composed of Pt nanoparticles supported on carbon. As Pt nanoparticles are mostly below 5 nm diameter, only carbon particles are visible in Figure 12. It is seen from the SEM images that the cathode thickness ranges between 15 and 21 µm. The thickness at the left and bottom locations is below the average range, which agrees with the platinum loading measurements. The morphology of the cathode catalyst layer exhibits a typical porous structure that contains meso- and macro-pores. The surface morphology of the cathode catalyst layer has been examined at low magnification in SEM, and the images are presented in Figure 13. The surface morphology is generally homogeneous for all five locations with some rough surface and cross-section observed at top and right locations due to uneven fracture during specimen preparation.

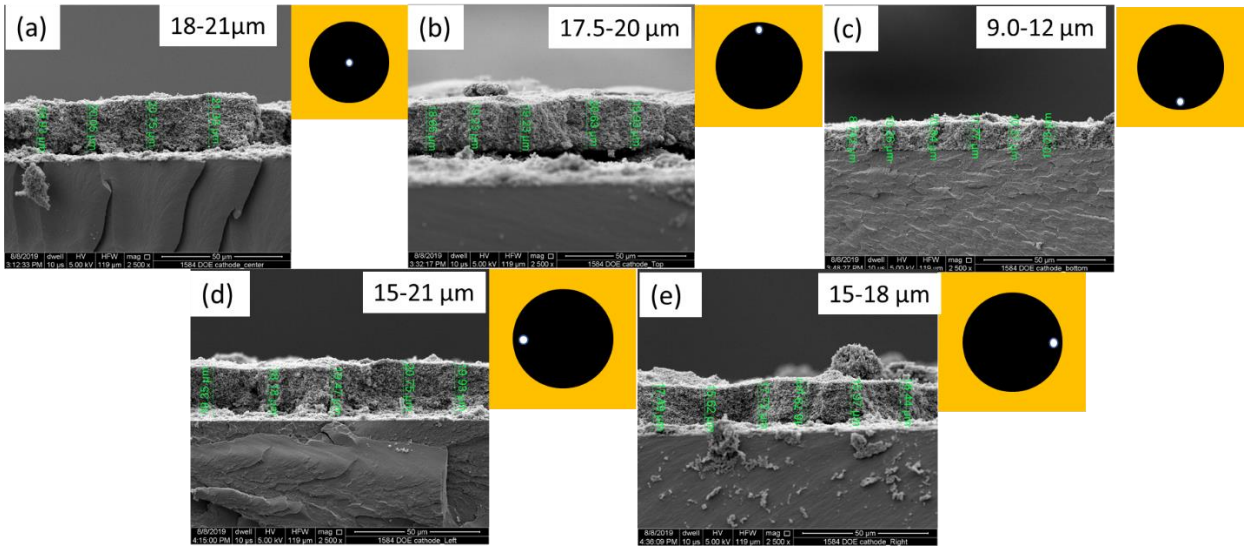

Figure 12. Cathode electrode thickness at five different locations of the active area.

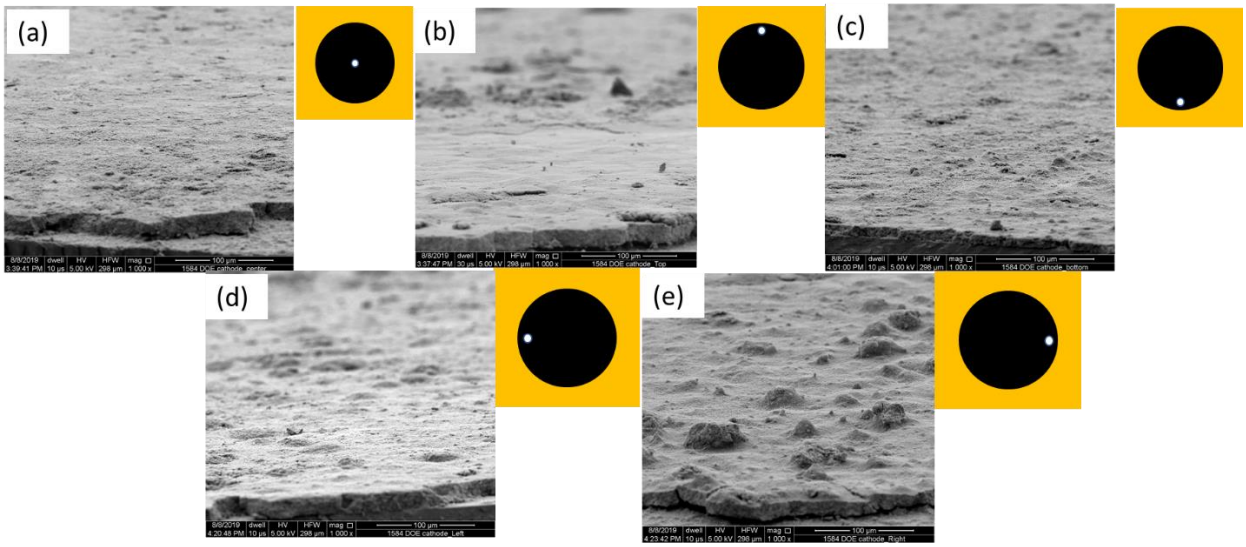

Figure 13. Surface morphology of cathode electrode at five different locations of the active area.

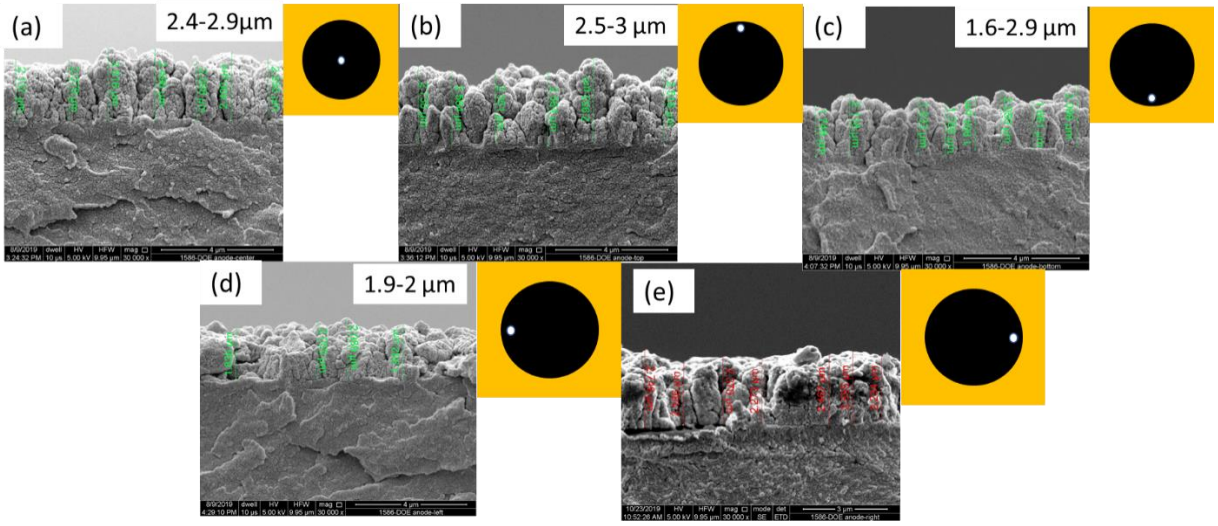

Figure 14. Anode electrode thickness at five different locations of the active area.

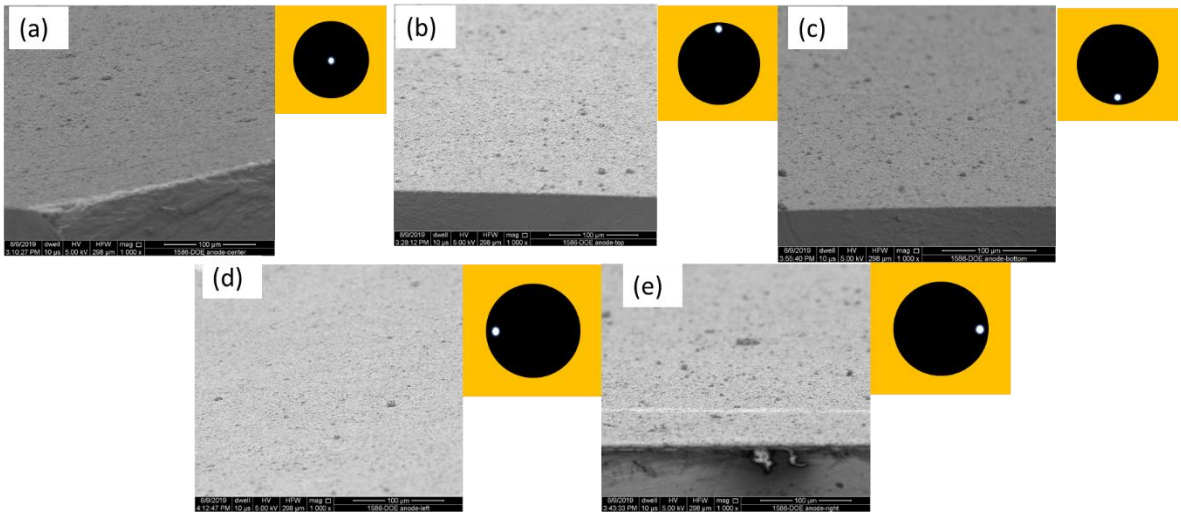

Figure 15. Surface morphology of anode electrode at five different locations of the active area.

The anode electrode shows a thickness range of 1.6-3 µm, which is composed of iridium nanoparticles embedded in Nafion ionomer (Figure 14). The morphology of the anode catalyst layer exhibits a column-like structure that contains meso- and macro-pores (Figure 14). The surface of the anode catalyst layer was examined at low magnification in SEM (see Figure 15). The surface morphology is homogeneous for all five locations. Few agglomerates (<10 µm) can be observed on the electrode surface.

Characterizations of the recombination layer

The Pt recombination layers are characterized by using TEM to study their microstructure. Specimens were prepared with ultramicrotome where the Pt layer and N117 are embedded in epoxy and polished into thin slices (~100 nm). Figure 16 (a) shows the TEM images of Pt recombination layer deposited on N117 membrane. The Pt layer is found between the N117 membrane and the epoxy. It is observed that the N117 membrane was partially disrupted during the microtome sectioning and thus, the Pt layer was also fractured and discontinued. At higher magnification, the Pt layer shows a structure of spherical agglomerates packing

into a layer (Figure 16(b)). The agglomerates are found to be composed of small Pt nanoparticles at higher magnifications (Figure 16 (c-e)). It can be concluded that the Pt recombination layer is not fully dense and likely has nano-porosity.

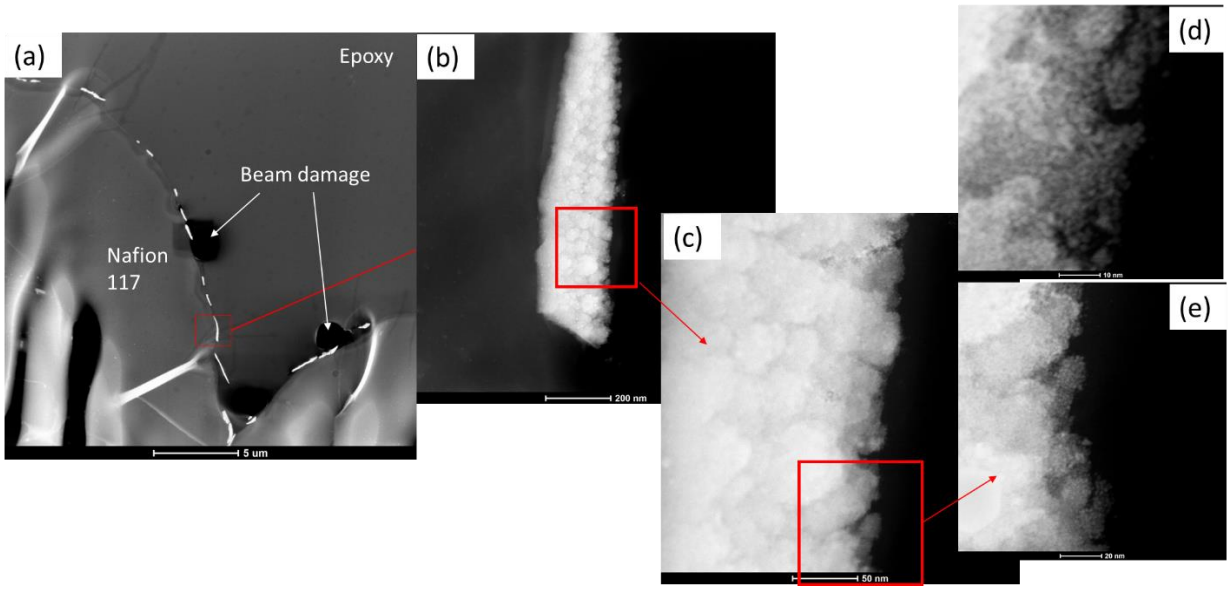

Figure 16. Cross-sectional TEM image of Pt recombination layer on N117 membrane. (a) shows an overview of the region being examined. (b, c, and e) are enlarged regions of the Pt layer. (d) shows the thin edge of the Pt layer where Pt nanoparticles can be distinguished at high magnification.

The Pt recombination layer after lamination is displayed in Figure 17. The 3-layer N117/Pt layer/N211 assembly was sectioned altogether with an ultramicrotome. Figure 17 (a) shows the membrane region which is usually torn apart after ultramicrotome. The Pt RL can be distinguished in the membrane as a thin bright strip due to Z contrast in high-angle annular dark-field (HAADF) TEM images. At higher magnification (Figure 17(b)), the Pt layer is found to be in good contact with the membrane at both left and right interfaces as shown in the image. Pt nanoparticles can also be distinguished at high magnification (Figure 17(c)). Figure 17(d) shows the EDS map of Pt in the square region of Figure 17(b), which confirms the presence of Pt. Figure 17(e) is the corresponding spectrum for the map.

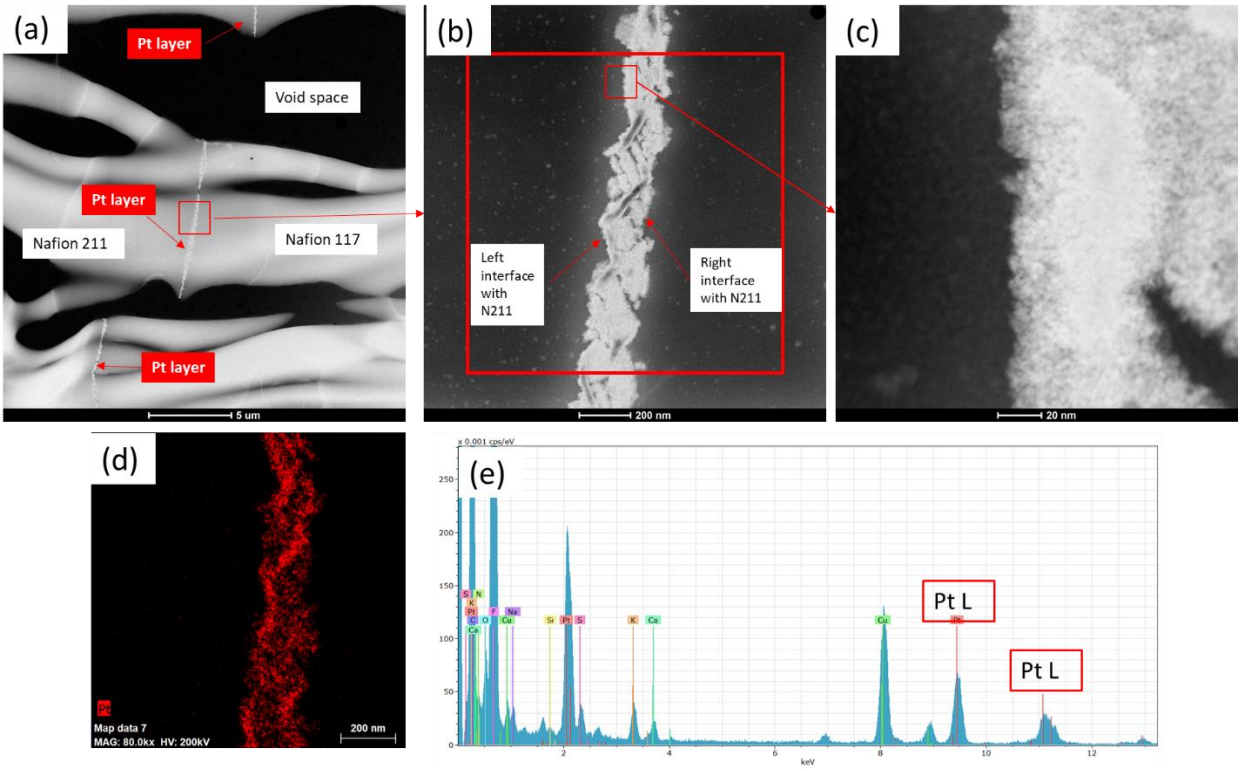

Figure 17. Cross-sectional TEM image of Pt recombination layer after laminated between N117 and N211 membranes. (a) shows the overview of the region being examined. (b) shows the enlarged region of (a). (c) shows the enlarged interface region of Pt and Nafion membrane. (d) shows the Pt EDS map of the square region in (b). (e) shows the spectrum of the EDS map.

In this early stage of the project, the optimal conditions for RSDT fabrication of anode, cathode catalysts layers as well as Pt RLs have been established and full CCMs were fabricated and tested. The evaluation of the RSDT fabricated anode and cathode electrodes showed that they are uniform and have precisely controlled thickness and catalyst loading. In addition, initial characterization of the Pt recombination layer structure has been performed, and its stability after 500 hours of operation has been demonstrated.

2.3. Long term testing of subscale CCMs

After defining the optimal RSDT deposition parameters, a set of 86 cm^2 CCMs (with round shape of the electrodes) have been fabricated. Coupons have been collected during each of the deposition events, and the electrodes' structure, morphology, and PGM loading have been examined. A short stack, consisting of two MEAs, one full cell (fully fabricated by the RSDT - anode, cathode, and RL), and one-half cell comprised from RSDT fabricated anode, and RL, and commercial cathode. The Ir loading in the RSDT fabricated anodes of these samples was estimated to be 0.2- 0.3 mg_{Ir}/cm^2, and the Pt loading in their cathodes was 0.2- 0.3 mg_{Pt}/cm^2. The Pt loading on the commercial cathode was 3 mg_{Pt}/cm^2. A schematic illustration of the RSDT fabricated full cell is presented in Figure 18. This figure shows the design of the CCM, as well as the PGM loading in the RLs and catalyst layers.

The two-cell short stack has been subjected to long-term stability test at steady-state conditions at 50°C, 1.8 A/cm^2, and 400 psi differential pressure. These operating conditions are typical for a

commercial hydrogen production system. All results from this 5000-hour durability assessment test have been summarized and published in two papers.[1,8] One of the papers reports the stack performance for up to 3000 hours,[1] while the second paper reports the results from the comprehensive post-test characterization of the full CCM.[8] Figure 19 shows the long-term steady-state performance for over 5000 hours of the full cell.

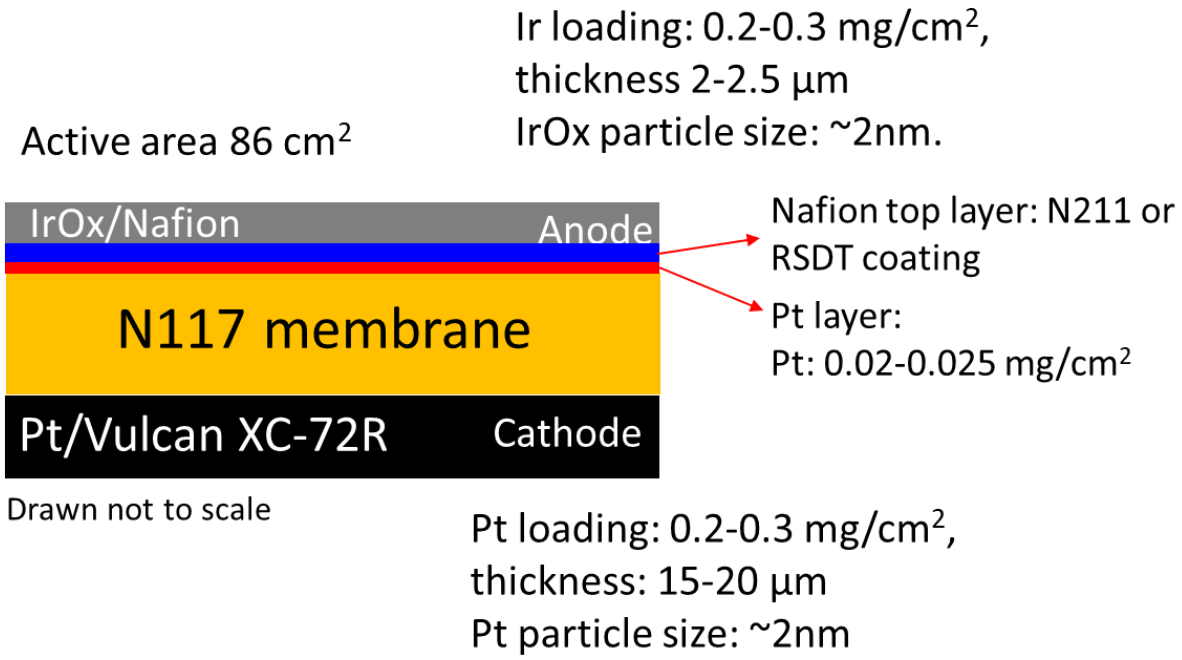

Figure 18. A schematic illustration of the full CCM fabricated by the RSDT method.

Figure 19 presents the potential transient for the 5000-hour steady-state operation, the polarization curves measured after different time of operation, and the hydrogen crossover measurements performed with the RSDT fabricated MEA. The cell voltage transient, collected during the steady state test of the MEA of interest, is presented in Figure 19 (a). The dotted vertical lines in Figure 19 (a) specify the times at which the polarization curves are measured. This figure shows that the cell voltage at the beginning of operation is 2.05 V, which is higher than the reported initial cell voltages in the literature for MEAs with higher catalyst loadings and thinner membranes.[8] The measured higher initial cell voltage may be attributed to the design of the used cell hardware, as well as the fact that the MEA is fabricated with thicker membrane consisting of two Nafion® membrane layers (Nafion® 117 and Nafion® 211), with a Pt recombination layer integrated between them, and ultra-low cathode and anode catalyst loadings. The activation procedure may also be a contributor to the measured higher initial cell voltage as the thicker membrane will require longer activation. A rapid increase of the cell voltage to above 2.15 V is observed at the beginning of the test. As it is explained in our paper, this normally happens because cell voltage stabilization does not occur immediately when the operating current density is initially applied to the cell.[8] Figure 19 (a) shows that the cell voltage decreased to its initial value (2.05 V) after 40 hours of operation and repeating several start/stop cycles for the diagnostic tests. The recoverable loss of the cell performance after each start/stop cycle is common in PEMWE cell

testing and may be attributed to the regeneration of the anode catalyst oxidation state, partial reduction of the surface oxidation of the Ti GDL (Gas Diffusion Layer) and the mass transport polarization. Recovery of the cell voltage is observed after each stop/start cycle for each diagnostic test during the 5000 hours of operation, as indicated by the vertical dotted lines in Figure 19 (a). The average cell voltage decay rate measured by linear fitting of the cell voltage transient, is estimated to be 37±4 µV h^{-1} during the first 3000 hours of steady-state operation. A sudden cell voltage increase of about 30 mV is observed at 3000 hours of operation, after performing the scheduled diagnostic tests. This voltage increase may be attributed to an increased ohmic resistance because of locally entrapped oxygen gas molecules (after the stop/start cycle) or to partial loss of contact as a result of the IrO_2 dissolution at the interface between the CL and the PTL (Porous Transport Layers). After performing the diagnostic tests, the cell performance remained stable with the reduced degradation rate of 15 ±2 µV h^{-1} until the end of the test. As estimated voltage decay rates are low and indicate significant stability of the RSDT fabricated catalyst layers. This finding outlines the advantages of the RSDT fabricated catalyst layers, especially the stability of the low-loaded Ir-based anode layers, which are usually more prone to severe degradation under electrolysis operating conditions. It is important to point out that the cell voltage decay rate estimated for the RSDT fabricated MEA that operated for 5000 hours is comparable with the recently reported decay rates of MEAs with similar PGM loadings, tested for only 1000 hours of operation.

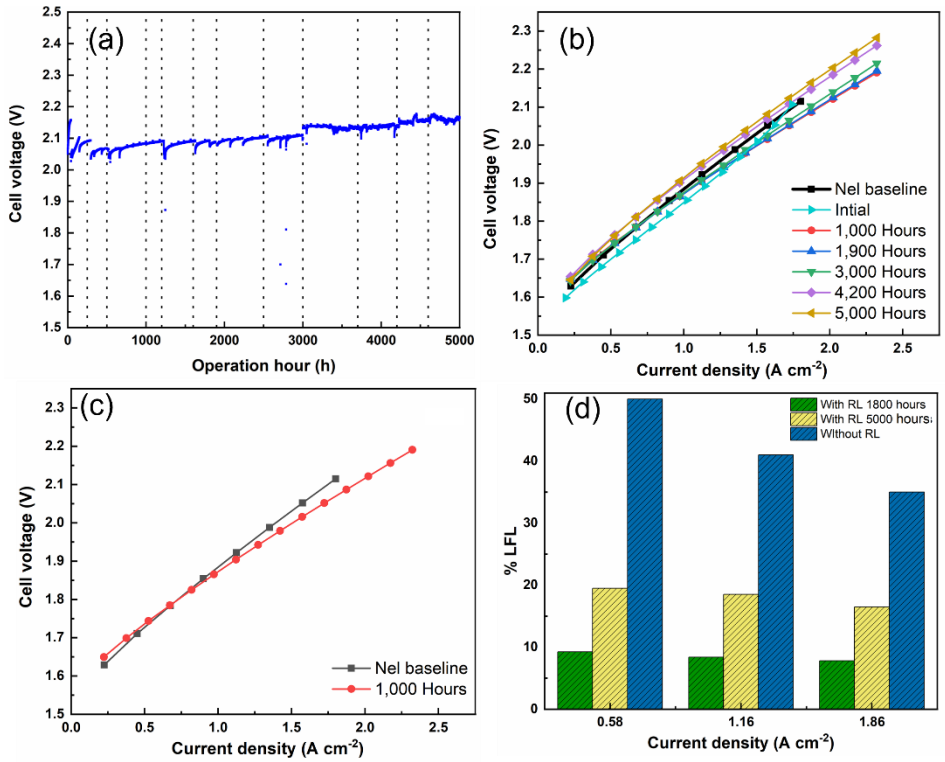

Figure 19. (a) Long-term electrolysis operation of the RSDT fabricated MEA. Vertical dotted lines mark times when diagnostic tests (polarization curves, EIS, and hydrogen crossover tests) were conducted. (b) I-V polarization curves for the RSDT-fabricated MEA during the operation. (c) Comparison of the I-V polarization curves measured at the BOT of the RSDT fabricated MEA and the Nel baseline MEA. The active area of the MEA is 86 cm^2. The tests were conducted at 50 °C with 1.8 A cm^{-2} current load, 400 psi hydrogen pressure, and ambient oxygen pressure. (d) Hydrogen crossover measured at different current densities.

The polarization curves, measured with the RSDT fabricated MEA after different times of operation at steady-state conditions, are compared in Figure 19 (b, c). The I-V polarization curves are measured periodically in the current density range of 0 to 2.3 A/cm^2 to monitor the MEA's performance losses as a function of the duration of the long-turn stability test. In addition, a polarization curve measured in the BOT of a commercial research grade MEA with high-PGM loadings (3 mg$_{Pt}$/cm^2 in the cathode and 3 mg$_{Ir}$/cm^2 in the anode), provided from Nel Hydrogen, is presented in the same figure, and is labeled as "Nel baseline". Figure 19 (b, c) shows that the cell voltages measured in the activation losses-controlled region of the polarization curves (at low current densities) for the RSDT fabricated MEA, are slightly higher than the ones measured for the baseline MEA. This indicates that the kinetics of the OER (Oxygen Evolution Reaction) reaction at the Ir catalyst layer for the baseline MEA is better than that of the RSDT fabricated MEA, which can be attributed to the fact that the baseline MEA has one-order of magnitude higher Ir loading in its anode catalyst layer. More importantly, the cell voltages in the ohmic losses-controlled region of the polarization curves are lower (about 40 mV) for the RSDT fabricated MEA for up to 3000 hours and slightly higher (about 10 mV) in the polarization curves measured after 4200 and 5000 hours of operation in comparison to the cell voltages measured at the BOT for the baseline MEA. This is a very important advantage of the RSDT fabricated MEA, because the industrial PEMWEs are operating at high-current densities, and the lower operating cell voltage is desired and contributes to improved overall efficiency and reduced cost of operation. The improved performance at high-current densities indicates that the RSDT fabricated MEA has improved catalyst utilization, which can be attributed to the cauliflower type morphology, higher porosity, and lower thickness of the deposited Ir catalyst layer in comparison to the-state-of-the-art commercial anode catalyst layers.[8] Figure 19 (b) also shows that mass transport limitations are not observed in any of the measured polarization curves at current densities of up to 2.3 A/cm^2.

Hydrogen crossover measurements were performed periodically as diagnostic tests to monitor the effectiveness of the integrated Pt recombination layer (RL) towards the hydrogen crossover suppression. Figure 19 (d) shows the concentration of the H_2 gas in the anode compartment, reported as percentage of the LFL, measured after 1800 and 5000 hours at three different current densities (0.58, 1.16 and 1.86 A/cm^2). The H_2 crossover measured after 1800 hours of operation remains below 10 % LFL at the three current densities of interest, which indicates that the Pt RL effectively suppresses the H_2 crossover. It is important to mention that H_2 concentrations below 10 % LFL are desired for safe operation of the electrolyzers. The measured %LFL after 5000 hours of operation is almost doubled, but it still remains below 20 % (see Figure 19 (d)), which is still well below the safety requirement of less than 50 % LFL. The effectiveness for the H_2 crossover suppression of the RL decreased with increasing of the durability test duration time. It is important to mention that the H_2 crossover in the commercial MEAs without RL is above 40 % LFL at the BOT. Hence, the Pt RL suppresses the H_2 crossover continuously, but its effectiveness is a function of the test's duration time, which shows that it is a subject of degradation processes. The structure, composition, design, and stability of the recombination layer is an objective of a separate work and is not discussed in the current paper. Figure 19 (d) also shows that the % LFL decreases with increasing of the current densities. This observation is expected as the generated O_2 at the anode is proportional to the applied current density, and thus more O_2 gas is generated at higher current densities, while the H_2 crossover remains relatively constant (the H_2 in the cathode compartment is under differential pressure of 400 psi at all current densities) and its concentration in the anode compartment decreases.

Based on the results obtained for the 86 cm^2 full cell fabricated by the RSDT and published in our publications [1,8] we concluded that:

1) The RSDT-fabricated Ir/IrO_x anode catalyst layers possess low Ir loading of 0.2-0.3 mg_{Ir} cm^{-2}, average Ir/IrO_x particle size of 1.46 ± 0.26 nm, and thickness of 2-2.5 µm. The Ir in this catalyst layer is predominantly in the fourth state of oxidation (Ir (IV)), which results in high OER mass activity of 600.1 ± 12.5 A g_{ox}^{-1} at 1.525 V vs. RHE. This mass activity is significantly higher than that of measured for the IrO_x catalysts fabricated by the wet chemistry methods.
2) The RSDT-fabricated Pt/C cathode catalyst layers have low Pt loading of 0.2-0.3 mg_{Pt} cm^{-2}, average Pt particle size of 2.69 ± 0.72 nm, thickness of 17-21 µm, and I/C ratio of 0.15. As-deposited catalyst showed considerably higher ECSA (electrochemical surface area) (115.9 ± 3.6 m^2 g_{Pt}^{-1}) than that of the commercial Pt/C catalyst (76.58 m^2 g_{Pt}^{-1}). Moreover, the HER (Hydrogen Evolution Reaction) current density measured for the Pt/C catalyst of interest is significantly higher than those measured for commercial Pt/C catalyst, Pt/WC catalyst fabricated by electrodeposition, and previously reported RSDT-fabricated Pt and Pt/Ebonex® catalysts.
3) As-deposited Pt recombination layers, with a loading of 0.025 mg_{Pt} cm^{-2} and thickness of 100-200 nm, effectively reduce the hydrogen crossover level to less than 10% of the LFL.
4) The RSDT-fabricated MEAs revealed better electrochemical performance with considerably lower PGM loadings than that of the baseline MEA. The polarization curves for the RSDT-fabricated MEAs show about 30 mV less voltage loss compared to that of the baseline MEA across the entire current density range of interest with no indication for mass transport limitations. In addition, the steady-state long-term electrolysis operation, conducted at 50°C with 1.8 A cm^{-2} current load, 400 psi differential pressure, indicates that the cell operates for 5000 h with no significant loss in the polarization performance.

2.4. Degradation mechanisms governing the performance loss in RSDT fabricated CCMs

After performing a comprehensive post-test analysis on the CCM that has been tested for 5000 hours, we identified and published the governing degradation mechanisms in PEMWEs.[8] We found that the harsh operating conditions at which the PEMWEs typicaly opperate lead to unavoidable degradation processes in all components of the MEAs. All failure modes contributing to the MEA's performance loss during the long-term 5000 hours steady-state test are summarized in Table 2. The MEA's components that are subjected to degradation are listed in the first column in Table 2, while the degradation processes and causes that drive these processes are listed in columns 2 and 3, respectively.

Table 2. Failure modes contributing to performance loss in RSDT fabricated low-loaded MEA during 5000 hours of steady-state operation

MEA's components	Degradation processes	Causes
Anode catalyst layer	Ir dissolution and Ir band formation	High anodic potential; low pH, formation of soluble iridium (III) complex during the OER;
	Ir migration, diffusion	Electric field, concentration gradient
	Imprint and cracks	Imprints of PTL; water flowing at high flow rate
	Pt dissolution from the Ti PTL	High anodic potential; low pH
Cathode catalyst layer	Pt dissolution and diffusion	Activation and stop/start cycles,
	Pt particle size increase	Coalescence; Agglomeration, Ostwald ripening
	Imprint and cracks	GDL imprint at high differential backpressure
Membrane	Chemical and mechanical degradation	Radical attack; holes formation
	Protonic conductivity decrease	Nanoparticle precipitation; Ir band formation

There is no known catalyst that can survive long-term operation at anodic potentials higher than 2 V and strong acidic environment (pH <1). Among all of the studied catalysts, the IrO_2 has the highest OER catalytic activity and stability. Even the best catalyst requires high loadings in order to sustain the harsh operating conditions and to provide the required durability for the MEAs. The RSDT fabricated catalyst layer with low IrOx loading showed remarkable stability for the duration of the long-term durabilitry test. 70 % of the initial catalyst loading remained within the anode CL, and only 30 % was dissolved, migrated into the Nafion® membrane, formed IrO_2 band (17%), migrated in the membrane and co-precipitated with the Pt ions (7%), and even reached the cathode and redeposited in its entire volume (6%). In addition, imprints and Pt flakes detached from the PTL along with cracks are obserbved within the CL layer. All these degradation processes are mainly caused by the severe operating conditions that include high anodic potentials and low pH.

The degradation mechanisms in the RSDT fabricated cathode catalyst layer with low Pt loading include: (i) Pt dissolution during the initial activation process, as well as during the start/stop cycles; (ii) Pt nanoparticles size increase as a result of re-deposition, agglomeration, coalescence, and Ostwald ripening; (iii) diffusion into membrane where the Pt ions are reduced from the cross-over hydrogen molecules and form nanoparticles in the membrane adjacent to the cathode CL. It is important to point out that 90% of the initial Pt catalyst remains in the cathode CL after 5000 hrs of operation, and only 10% of the Pt is found to form Pt nanoparticles in the membrane. In addition, imprints from the GDL and cracks in the cathode catalyst layer are also clearly seen, which could be attributed to the firm mechanical contact between the GDL and the CL at the high axial load where the cell operates.

The failure modes associated with the membrane include chemical and mechanical degradation, as well as decreased proton conductivity as a result of the Ir band and Pt/Ir nanoparticles formation in the volume of the membrane.

Identifying and understanding all degradation mechanisms contributing to the MEA's performance loss during long-term steady-state MEA test are very important steps, but it is even more important to quantify their contribution and distinguish the governing degradation mechanism. Finding viable mitigation strategies for controlling the governing degradation mechanism will ensure improvement of the PEMWEs durability performance. Based on the comprehensive analysis, as well as the discussions in our paper [8] it is obvious that only 10% of the Pt is dissolved from the cathode catalyst layer, and the average particle size distribution increased from 2 nm to 4 nm, as a result of the 5000 hrs. of operation at steady-state conditions. These degradation processes have marginal impact on the performance loss, and generally show that the RSDT fabricated cathode catalyst layers are appropriate for long term operation. In addition, the degradation processes observed in the membrane do not contribute substantially to the overall MEA performance loss. The degradation processes that are taking place in the anode have the largest contribution to the performance loss in the low loaded MEAs, fabricated by the RSDT methodology. Thus, the Ir dissolution is the governing degradation mechanism that defines the durability of the MEA of interest. The main cause that drives the Ir dissolution is the high operating cell voltage and the low pH during operation. While the high acidity cannot be controlled during the cell operation, the cell voltage can be reduced below 1.9 V by implementing thinner membranes. Decreasing the membrane thickness will result in increasing the H_2 cross-over, but this problem can be mitigated by using recombination layer to keep it below the required 10 % of LFL. Other strategies for reducing the operating cell voltage at current densities higher of 2 A/cm^2 include: (i) developing porous transport electrode (PTE) based MEA configuration to increase the interfacial area between the catalyst layers and Ti-porous layers, (ii) optimizing the ionomer content in the catalyst layer to facilitate any mass transport phenomena during the cell operation, and (iii) lowering the ohmic resistance from the cell components.

The conclusions from this comprehensive investigation are as follows:

1. It was found that 30 % of the Ir from the anode CL dissolved and formed an Ir-band in the membrane, co-precipitated with Pt ions and formed Pt/Ir nanoparticles in the volume of the membrane, and even reached the cathode and re-deposited in its entire volume. This is the governing degradation mechanism that has the highest contribution to the MEA performance loss.
2. Pt in the cathode CL is also subject to dissolution during the activation and start/stop cycles. 10 % of the Pt dissolved and penetrated into the membrane where Pt nanoparticles were formed. 90 % of the Pt remains in the cathode CL after 5000 hrs. of operation. These findings show that

RSDT fabricated cathode CLs are stable and have minimal contribution to the MEA performance loss.

3. The failure modes associated with the membrane include chemical and mechanical degradation, as well as decreased proton conductivity as a result of the Ir band and Pt/Ir nanoparticles formation into the membrane's volume.

Degradation processes are taking place in all parts of the MEA as a result of the 5000 hrs. of operation at steady-state conditions. Although all degradation processes have an impact on performance loss the governing degradation mechanism was identified to be the Ir dissolution from the anode catalyst layer. The main driving forces for the Ir dissolution are the high operating cell voltage and high acidity (pH=1). This shows that it is of critical importance to reduce the cell voltage to below 1.9 V at current densities higher than 2 A/cm^2, in order to improve the durability performance of the MEAs. One viable pathway to achieve this challenging goal is to reduce the thickness of the membrane, but this will require more effective management of the H_2 cross-over. Other strategies include improving the cell design, which includes reduction of the ohmic losses in the cell's components, decreasing the interfacial contact resistances between the PTL and catalyst layer, and improving the stability of the PTL. These are the challenging research tasks that our team addressed in the BP2.

With this research and development effort we demonstrated that the RSDT is an advanced technology that allows one-step fabrication of cost-effective, high-performance, and durable MEAs for the next generation PEMWEs. The results obtained outlined the great potential of this technology to boost the commercialization of PEMWEs substantially. All milestones for BP1 have been successfully met. The Go/No-Go decision to demonstrate 1000 hours of stable performance has been surpassed and we demonstrated that the RSDT fabricated CCMs with ultra-low PGM loading, are stable for over 5000 hrs.

3. Accomplishments during budget period 2.

In budget period 2, we focused our efforts on scaling up the RSDT fabrication process of CCMs with active area of 86 cm^2 to 680 cm^2, which has been designed to fit the megawatt scale PEMWEs stack that is commercial product of our industrial collaborator, Nel Hydrogen USA.

3.1. Redesigning the recombination layer. Long-term durability testing and characterization.

We used the knowledge accumulated during BP1 and successfully fabricated CCMs with ten times lower PGM loading in their catalyst layers, and integrated RLs in the volume of the Nafion membrane. In addition, the team redesigned the CCMs and fabricated the first CCMs with two RLs (duo-RL design) and demonstrated stable and effective H_2 crossover suppression for over 3000 hours in subscale CCMs.

The new two-layer recombination layer design change was tested in a subscale 86 cm^2 cell to verify its performance over time. Figure 20 presents a schematic of RSDT fabricated CCM (UC031) with active area of 86 cm^2, and unique dual recombination layer design, developed for first time in this project. The details of the fabrication steps are as follows:

1. To fabricate the dual recombination layer, a Pt/Nafion® layer (Pt RL) was deposited directly onto the Nafion® N117 at conditions that ensure platinum loading of ~0.025mg$_{Pt}$/cm^2. The Nafion® dispersion was sprayed from the secondary nozzles, and the Nafion®: Pt volume ratio in this first platinum layer is 3:1. After that, a 10µm thick Nafion® isolation layer was deposited onto the Pt/Nafion® RL by spraying Nafion® D521 dispersion from the secondary nozzles. Immediately following the Nafion® isolation layer deposition, a second Pt/Nafion® layer was deposited onto this Nafion® layer using the same deposition parameters as in the case of the first Pt RL. Lastly, a 15µm thick Nafion® topcoat layer was deposited on top of the second Pt/Nafion® layer by spraying Nafion® D521 dispersion from the secondary nozzles. Throughout all Pt/Nafion® and Nafion® dispersion depositions, the CCM was heated to 95°C and secured to the substrate holder with vacuum (24cm Hg). Once the final Nafion® topcoat layer was deposited to complete the dual recombination layer design, the CCM was hot pressed at 130°C for 3 minutes at 90 psi. Nothing unusual was observed during the dual recombination layer deposition and hot-pressing.

2. The Pt/C cathode catalyst layer was deposited on the opposite side of the hot-pressed dual recombination layer using the RSDT-II. Nothing unusual was reported during this deposition.

3. The IrOx anode catalyst layer was deposited on the RSDT coated Nafion insulation layer side using the RSDT-II, and nothing unusual was reported during this deposition.

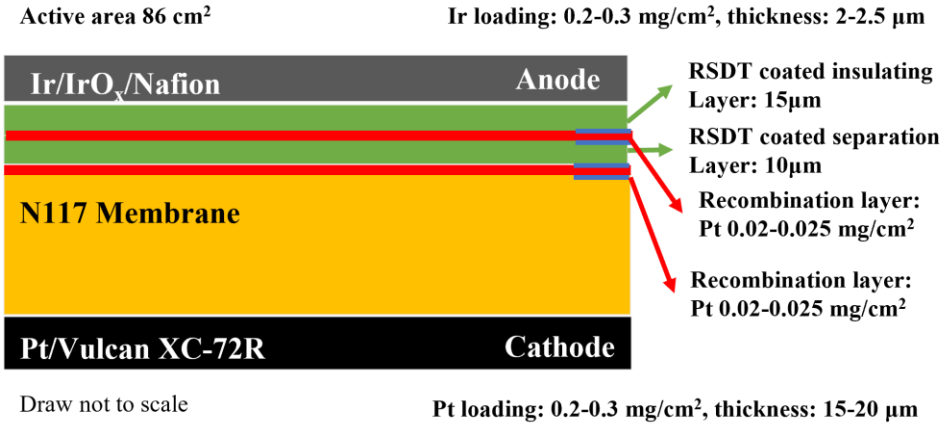

Figure 20. Schematic illustration of the RSDT-fabricated full cell (UC031).

This cell has been assembled in a single cell configuration, and has been tested for over 3000 hrs., and the H_2 crossover was continuously measured. The cell was subject to a break-in procedure followed by a long-time steady state durability assessment test. Steady-state data and polarization curves were collected on the same test stand. The hydrogen crossover tests were performed on a different test stand, designed, and calibrated for these measurements. Steady state voltage data for this test is presented in Figure 21. Steady state operating trends from the 5,000-hour durability test are included for comparison.

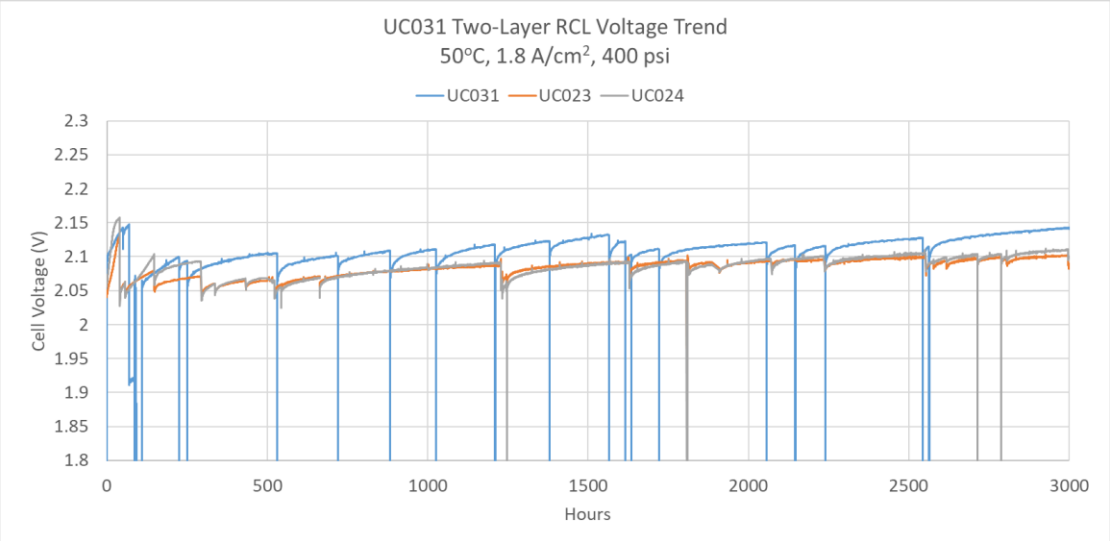

Figure 21. Steady state operating trends for UC031with duo recombination layer verification test cell at 50°C, 1.8 A/cm^2, and 400 psi. The data is compared to the two cells from the 5,000-hour durability test, discussed in the previous section.

At the end of testing, the cell voltage is 2.14 V at 50°C, 1.8 A/cm^2, and 400 psi, which is an increase of 56 mV in comparison to the cell voltage of the 5,000-hour test cells at the same point in testing. In addition to the cell voltage increase, the degradation rate is higher for the two-layer recombination layer cell (42 µV/h over the last 1,000 hours for UC031 versus 25 µV/h and 37 µV/h at 3,000 hours for UC023 and UC024, respectively). Hydrogen crossover rate was monitored continuously throughout the test and showed no indication of a loss in functionality of the two-layer recombination layer over 3,000 hours.

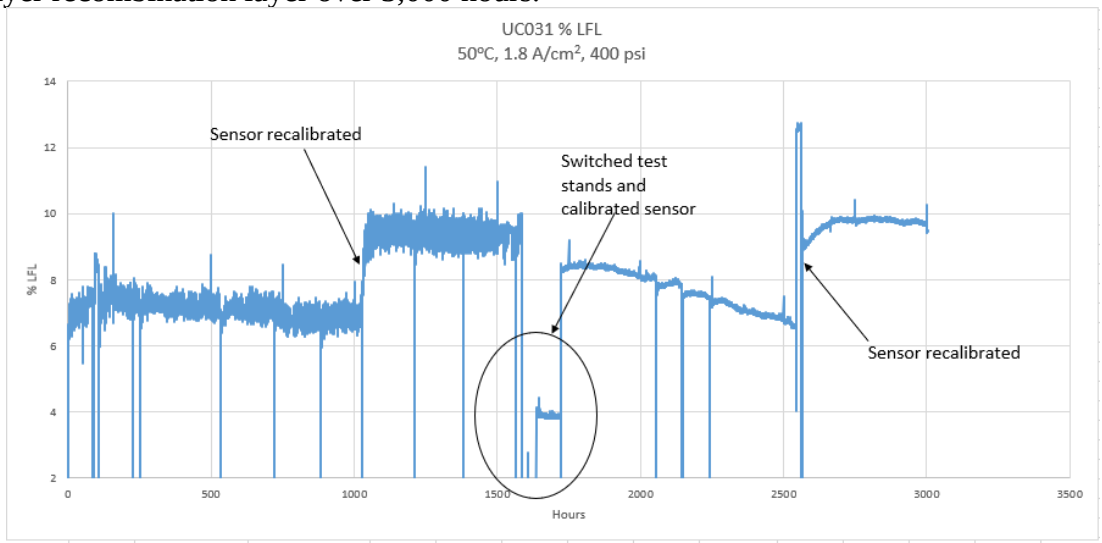

Figure 22. Hydrogen fraction in water reservoir headspace represented as a percentage of the lower flammability limit of hydrogen in oxygen tracked through the 3,000-hour durability test. % LFL was recorded as a measure of hydrogen back-diffusion rate.

Figure 22 shows the crossover rate trend measured as a fraction of hydrogen in the water reservoir head space relative to the lower flammability limit of hydrogen in oxygen. It is seen that there is no sign of a consistent trend toward a higher fraction of hydrogen in the electrolyzer

product stream as a function of time, suggesting the recombination layer remained sufficiently effective throughout the life of this test.

Polarization curves were collected every 250 hours throughout the course of the test. Figure 23 shows the polarization curves collected from 1,500 hours to 3,000 hours. The shape of the curves through the second half of the test remained consistent and there was no recurrence of the mass transport limitation that was present at the beginning of the test. The absolute voltage trend mirrors the steady state voltage trend, including temporary voltage reductions after restarting.

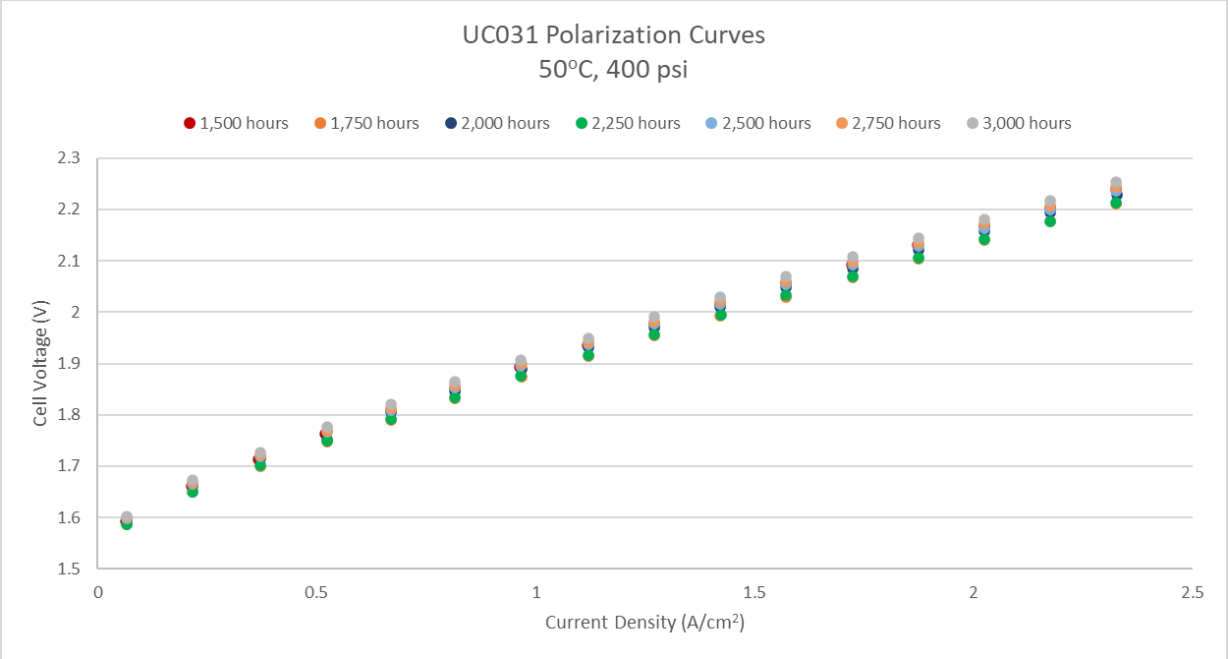

Figure 23. Polarization curves collected over the final 1,500 hours of testing at 50°C and 400 psi.

Pre-test Characterization

The platinum loading of the cathode was estimated by ICP-OES on coupons deposited along with the membrane during the deposition event. The estimated average Pt loadings in the coupons is $0.17 mg_{Pt}/cm^2$. The iridium loading in the anode was also estimated by ICP-OES on coupons deposited along with the membrane. The estimated average Ir loadings in the coupons is $0.3 mg_{Ir}/cm^2$.

Post-test Characterization

We have used advanced techniques and methods for physical and chemical characterization of the MEA after the test, such as ultramicrotome, HRTEM, HAADF-STEM, STEM-EDS mapping, SEM, and EDS mapping. All the tests were performed to understand the degradation mechanisms that govern the durability performance and H_2 crossover mitigation in this 86 cm^2 CCM.

SEM characterization

Figure 24 shows the SEM cross-sectional images of the MEA after 3000 hours of steady-state operation at 1.8 A/cm^2, 50 ˚C, and 400 psi differential pressure. The SEM image presented in Figure 24 (a) shows that the thickness of the anode catalyst layer (CL) is 1-1.5μm, while the thickness of the cathode CL is 17-20 μm. In addition, the two recombination layers are clearly seen in Figure 2 (a). No membrane thinning is observed in the images presented in Figure 24. The higher magnification SEM images presented in Figure 24 (b-c) show that the morphologies of the IrOx anode catalyst layer and carbon-supported Pt/C cathode catalyst layer are preserved after 3000 hours of operation.

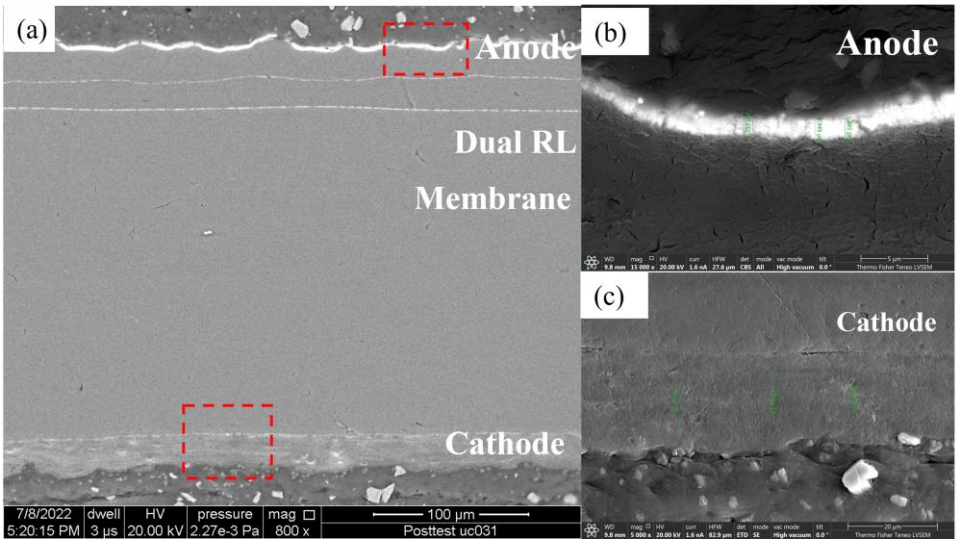

Figure 24. (a) SEM cross-sectional image of sample from MEA UC031 after the durability test. The dual recombination layers are sprayed on the N117 membrane closed to the anode side. (b) The anode catalyst layer. (c) The cathode catalyst layer.

Figure 25 shows the SEM-EDS map and line- profile scan image of a cross-section of the MEA after 3000 hours of steady-state operation. Figure 25 (a) shows the Ir and Pt distribution in the anode and cathode, separately. Figure 25 (b) shows that the Ir is also present in the cathode, which implies that the Ir dissolved from the anode and migrated to the cathode during the steady-state test.

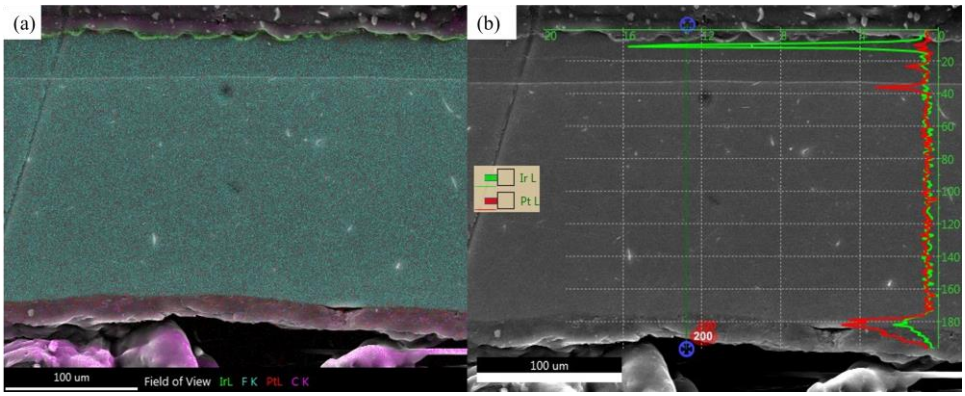

Figure 25. (a) SEM-EDS maps of cross-section of the MEA after the durability test. (b) SEM line profile scan image of the MEA after the durability test.

TEM characterization

Figure 26 presents STEM (Scanning Transmission Electron Microscopy) and EDS mapping images of the anode catalyst layer after the test. It is seen that the IrOx anode catalyst layer is 1-1.5µm thick (see Figure 26 (a)). Figure 26 (a, b) suggests that the iridium dissolves from the anode and diffuses into the membrane where it forms an Ir band. The analysis of these images indicates that the density of the Ir in the band is higher in the membrane adjacent to the anode and decreases with increasing the distance from the anode catalyst layer. Figure 26 (d-f) presents the STEM images of the Ir band at different magnifications. It is well known that the Ir dissolution process shares the same intermediate species with the OER at the anode at high anodic potentials. Although iridium is one of the most stable metals at these high positive potentials, the dissolution process cannot be completely avoided. At cell voltages 1.9 V and higher, the Ir dissolution rate increases, and the concentration of the Ir ions in the membrane increases, respectively. The dissolved Ir ions penetrate and diffuse into the membrane, but the diffusion of the Ir ion in the solid electrolyte is slowed. That is why the concentration of the Ir ions is substantially higher in the membrane adjacent to the anode. When it reaches supersaturation limits, the Ir ions precipitate and form the denser layer seen as the Ir band. The thickness of this band is defined by the diffusion coefficient of the Ir ions into the membrane and the operating cell voltage that represents the dissolution rate of the Ir catalyst, and hence defines the Ir concentration in the membrane. After the Ir band, the Ir ions continue to migrate into the membrane.

Another degradation mechanism associated with the anode includes the Ir and Nafion^{tm} ionomer distribution. It is well known that the Nafion^{tm} content plays a crucial role and impacts the catalysts' activity. Non-uniform Nafion^{tm} ionomer distribution can result in lower catalytic activity. Figure 26 (b-c) suggests that the post-test anode catalyst has a local non-uniform distribution of the Nafion^{tm} ionomer in the Ir CL. The variation in the F distribution in Ir CL may be explained by the Ir dissolution followed by diffusion and migration, which results in cell performance loss.

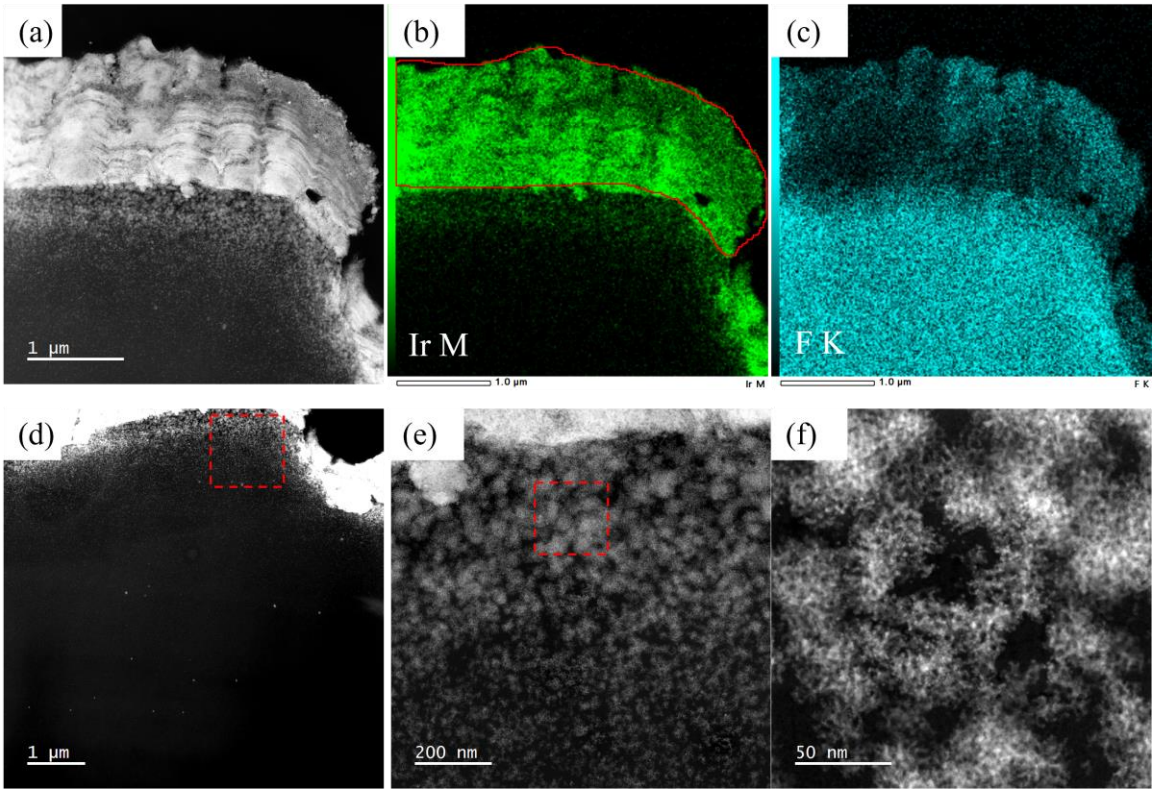

Figure 26. (a) STEM image of the anode catalyst layer after the stability test. (b-c) EDS maps of the Ir and F elements. (d-f) STEM images of the Ir band at different magnification.

Figure 27 presents STEM images and EDS elemental maps of recombination layer 1 (closer to the anode) after the test. It is seen that the post-test Pt recombination layer 1 is not continuous. The thickness of this RL is 50 nm (see Figure 27 (a)). The STEM EDS elemental maps and spectrum, presented in Figure 27 (b, c) show that no Ir is detected in the recombination layer. The high-resolution images, presented in Figure 27 (d, e) show the morphology of the Pt recombination layer after the test. It is seen that Pt nanoparticles are observed in the vicinity of the recombination layer. The nature of the formation of these nanoparticles is currently unknown.

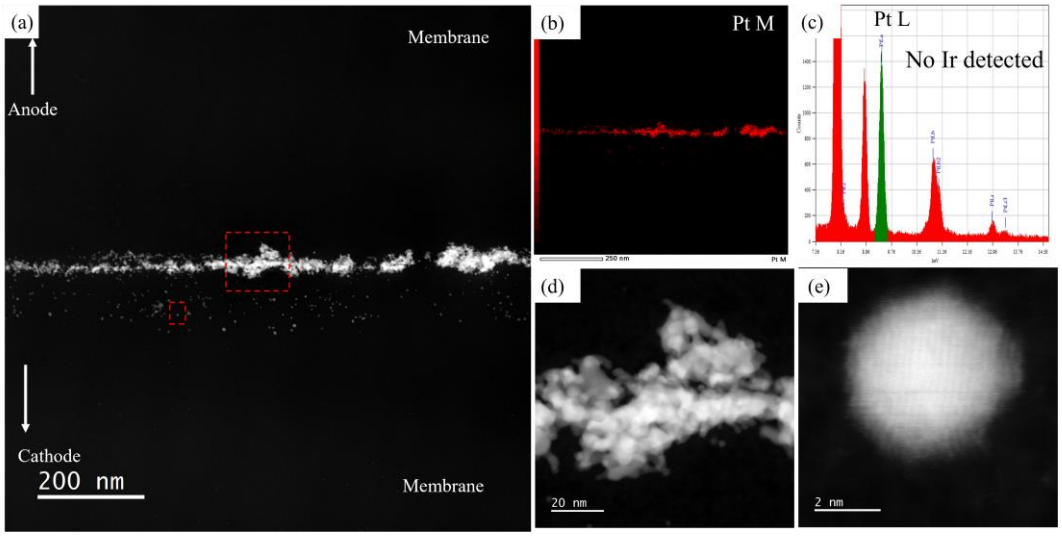

Figure 27. (a) STEM image of the recombination layer 1 (closer to the anode), after the durability test. (b) EDS elemental map of Pt at the same location. (c) EDS spectrum collected at the mapping location. (d, e) high-resolution STEM images of the Pt recombinant layer.

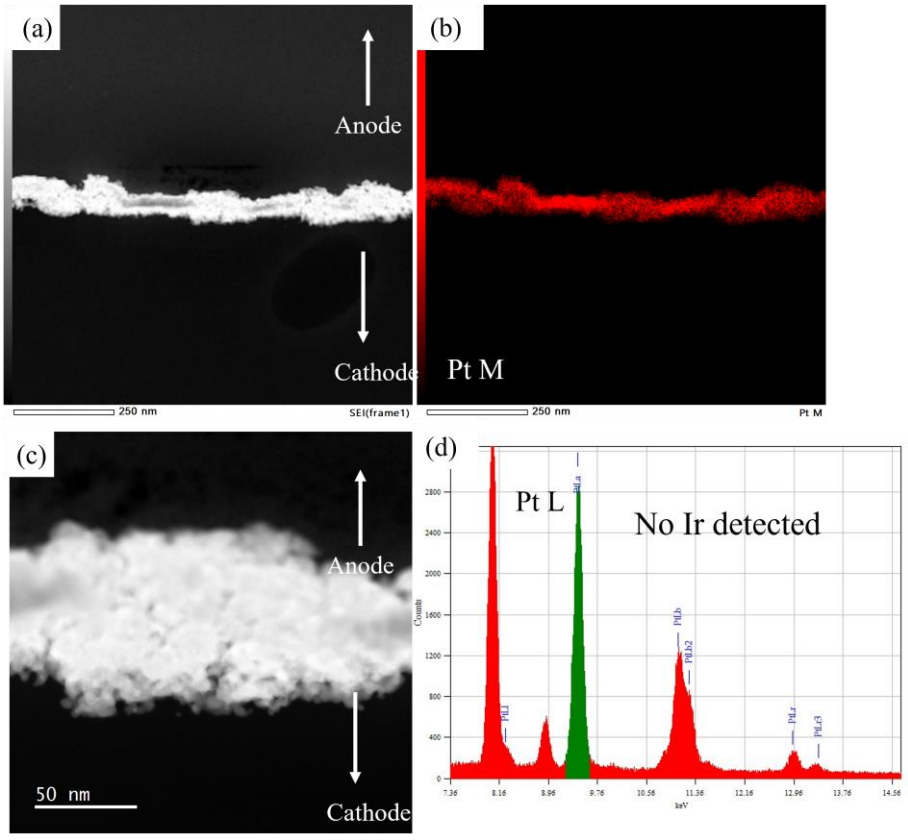

Figure 28. (a) STEM image of recombination layer #2 (closer to the cathode) after the 3000 steady-state test. (b) EDS elemental map of Pt at the same location. (c) high-resolution STEM images of the Pt recombinant layer. (d) EDS spectrum from the mapping location (all peaks in the EDS spectra, including the green peak, belong to Pt) .

Figure 28 shows STEM images and an EDS map of the recombination layer 2 (closer to cathode) after the test. It is seen that the post-test Pt recombination layer 2 remains dense, with a thickness of 50-100 nm in Figure 28 (a, c). The STEM map and spectrum in Figure 28 (c, d) shows that no Ir is detected in the recombination layer after the durability test.
The constant mitigation of H_2 crossover during the steady-state test of 3000 hours, suggests that the dual recombination layer design offers stable performance and effective crossover suppression. Both recombination layers are discontinuous after the durability test but still work efficiently to reduce the H_2 crossover.

The HAADF-STEM images and EDS maps of the Pt/C cathode catalyst layer after 3000 hours of steady-state cell operation are presented in Figure 29. The porous structure of the Pt/C electrode is evident in Figure 29 (a-b). The STEM image presented in Figure 29 (c) clearly shows the presence of nanoparticles in the volume of the membrane on the cathode side. Figures 29 (e, f) show the HAADF-STEM-EDS elemental map and the compositional profile analysis of nanoparticles in the cathode. This figure shows that both Pt and Ir are present in the nanoparticles, which is different from the pre-test TEM images of the cathode. This result proves that the Ir ion migrates during the durability test.

Another important observation is that the average Pt nanoparticle size in the cathode CL increased by about a factor of 2 after 3000 hours of operation. The high-resolution HAADF-STEM images of the nanoparticles formed in the membrane in the cathode catalyst layer are presented in Figure 29 (d). This figure shows that the average particle size after the durability test is 3-4 nm, while the average particle size before the test is 2 nm. This indicates that Pt re-deposition and coalescence occur in the cathodes during the long-term steady-state test, resulting in reduced Pt utilization and loss of mass activity.

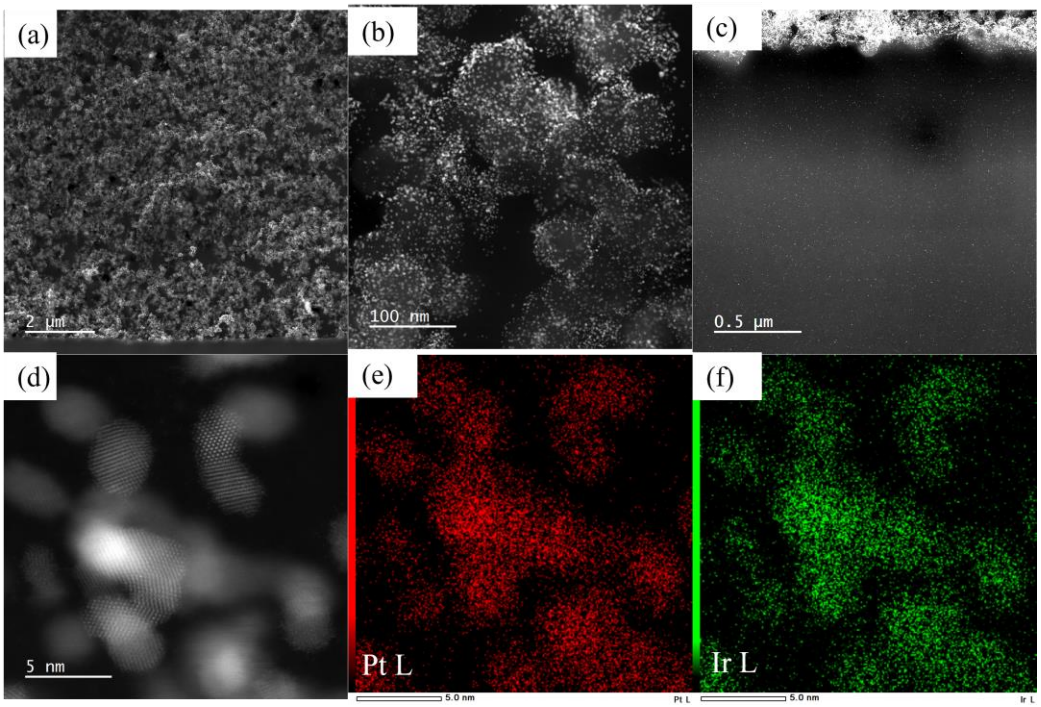

Figure 29. (a-c) STEM images of the post-test cathode layer. (d) High-resolution STEM images of the Pt nanoparticles in the cathode catalyst layer. (e, f) EDS elemental maps of Pt and Ir.

3.2. Scale up fabrication, characterization, and testing

After proving that the concept of the novel duo RL design works perfectly on subscale (86 cm^2) CCMs, our team focused its efforts on scaling up and testing large-scale 680 cm^2 CCMs with the same design. To fabricate the dual layer recombination layer, platinum was deposited by RSDT from the primary nozzle, while a Nafion® dispersion was sprayed by the RSDT secondary nozzles such that the Nafion®:Pt volume ratio in the first platinum layer was 3:1. The Pt/Nafion® deposition was sprayed directly on Nafion® 117 membrane and the estimated platinum loading is ~0.025mg_{Pt}/cm^2. Nafion® D521 dispersion was then sprayed onto as deposited RL using the RSDT secondary nozzles to form a 10μm thick Nafion® separation layer on top of the first platinum layer. Immediately following the Nafion® separation layer deposition, a second Pt/Nafion® RL was then deposited by RSDT using identical deposition parameters as for the first RL. Lastly, a 15μm thick Nafion® topcoat layer was deposited by spraying the dispersion through the RSDT secondary nozzles to form the isolation Nafion® layer. Throughout the Pt/Nafion® and Nafion® layer fabrication steps, the substrate holder was heated to 95°C to prevent wrinkles from forming and to ensure uniform Nafion® coatings. Once the final Nafion® topcoat layer was added to complete the dual recombination layer design, the CCM was hot pressed at 130°C for 3 minutes at 90 psi using an optimized hot press procedure. Pictures of the dual recombination layer design before and after the hot press step are presented in Figure 30. It is seen from Figure 30 that the sample is uniform and homogeneous and is free of defects.

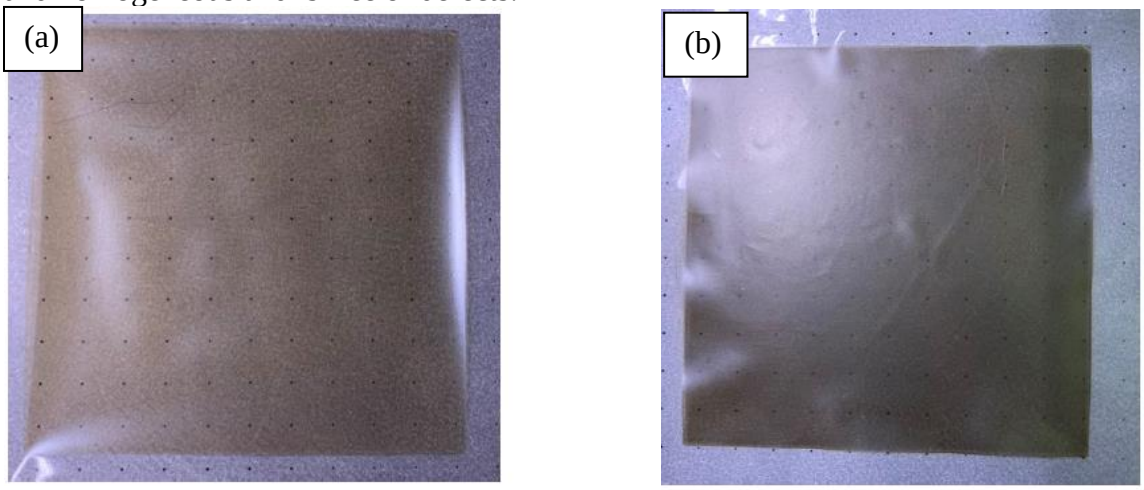

Figure 30. Pictures of the dual recombination layer design: (a) after finishing the deposition of the first Pt/Nafion® RL, the 10μm Nafion® separation layer, the second Pt/Nafion® RL, and the 15μm Nafion® topcoat layer; (b) the same 680 cm^2 sample after the hot press step.

The next step in the MEA fabrication process is cathode fabrication. At the start of the cathode deposition, the CCM was placed with the RSDT fabricated Nafion® isolation layer facing the substrate holder where it was observed that the CCM is completely flat with no signs of wrinkles. The Pt/C cathode catalyst layer was deposited by the RSDT directly on the Nafion® 117 membrane. During the deposition, coupons were placed on the substrate holder mask adjacent to the active area of the cell for characterization. A schematic of this configuration of the cathode deposition setup is presented in Figure 31.

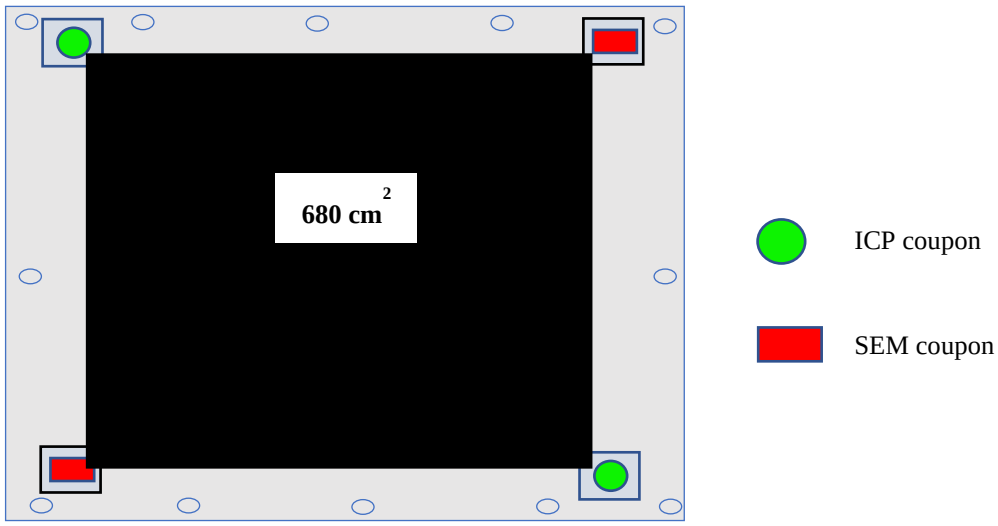

Figure 31. Schematic of the positions of the coupons for ICP and SEM characterization.

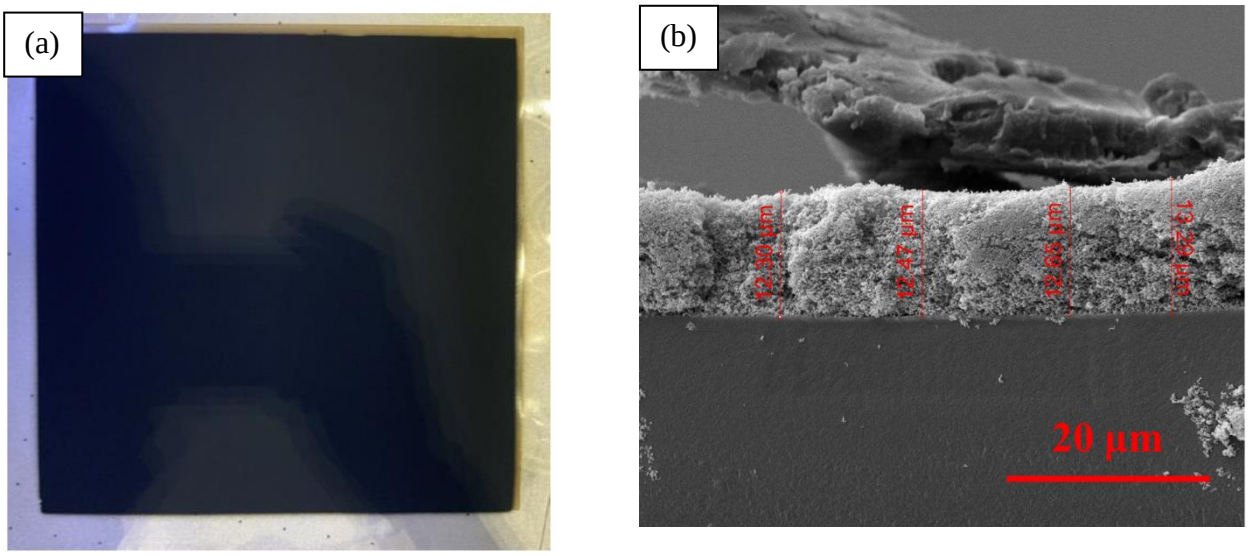

Figure 32. (a) Picture of the RSDT fabricated 680 cm^2 Pt/C cathode catalyst layer. (b) Cross sectional SEM image from the coupon of as fabricated Pt/C cathode catalyst layer.

A picture of the RSDT fabricated Pt/C cathode catalyst layer is presented in Fig. 32 (a). Cross-sectional SEM analysis of the coupons showed a homogeneous and uniform catalyst distribution with average thickness of 13.0 ± 0.4µm as seen in Figure 32 (b). This is similar to what was observed in the previous trials performed after optimization of the deposition parameters for cathode catalyst layer fabrication. In addition, a sample from the coupons was sent out for ICP analysis to determine the catalyst loading in the cathode electrode. According to the results, the platinum loading of the cathode electrode measured on the coupons is 0.131mg_{Pt}/cm^2. Since the coupons are placed by the edge of the CCM, this coupon loading is expected to be slightly lower

than the overall cathode catalyst loading. Previous trials have shown a similar loading on the coupons resulted in an average cathode catalyst loading of 0.186 mg_{Pt}/cm^2.

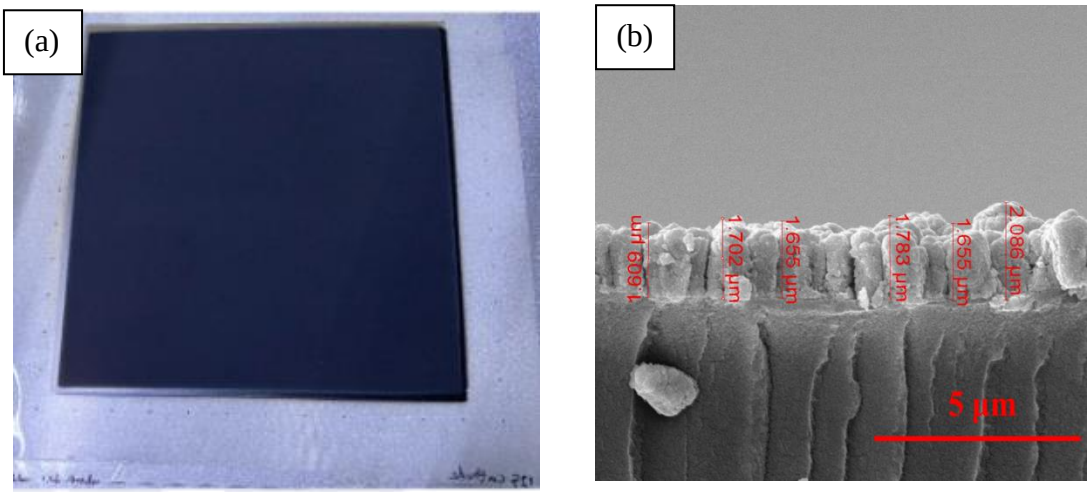

Figure 33. (a) Picture of the RSDT fabricated 680 cm^2 IrOx anode catalyst layer. (b) Cross-sectional SEM image from the coupon of as fabricated IrOx anode catalyst layer.

A picture of "as fabricated" large scale 680 cm^2 IrO_x anode catalyst layer is presented in Fig. 33 (a). At the start of the anode deposition directly on the RSDT fabricated Nafion® isolation layer, the CCM appeared to be flat with no sign of wrinkles. During the deposition, coupons were placed on the substrate holder mask adjacent to the active area of the cell for characterization as can be seen in Fig. 31. Cross-sectional SEM analysis of the coupons showed an average thickness of 1.8 ± 0.2µm with a uniform columnar structure as seen in Figure 33 (b). The iridium loading of the anode electrode measured on the coupons came to 0.252mg_{Ir}/cm^2. Following the anode deposition, the CCM was placed between two layers of Kapton® to protect the deposited catalyst layers. The CCM was then slid into a sealed bag and placed between two polyacrylic sheets to keep it flat and prevent folding, and then was placed in a dry storage box. The sample remained in the storage box until it was hand-delivered to Nel Hydrogen for testing.

At this stage of the project, we used the optimized procedures and conditions for RSDT fabrication of large scale 680 cm^2 to verify, again, the applicability of the RSDT for fabrication of full scale MEAs for advanced PEMWEs with ultra-low Pt and Ir loadings in their catalyst layers. All the RSDT parameters and conditions for fabrication of the Pt recombination layers, separation and isolation Nafion^m layers, Pt/C cathode catalyst layers, and IrOx anode catalyst layers for full scale 680 cm^2 MEAs, have been optimized and their reproducibility was proved. With completion of these research tasks our team successfully met the project's milestone, defined as "Scale-up of electrode manufacturing: With the optimized cathode, anode, and recombination layer, full RSDT cell is scaled up to 680 cm^2 (full scale) active area".

Full-Scale CCM Durability Test

As fabricated large-scale 680 cm^2 CCM fabricated by RSDT, has been tested for 1,000 hours at steady-state conditions. The cell was operated at 50^{o}C and 1.8 A/cm^2. Early in the test, the cell

was tested at 130 psi differential pressure due to a technical problem with our test stand. After fixing the problem, the remainder of the test was performed at 400 psi differential pressure. The complete steady-state cell voltage transient, measured during the 1000 hrs. of operation of the large-scale (680 cm^2) MEA, is presented in Figure 34. At the end of the test, the cell was operating at 2.084 V, which is identical to the cell voltage of the 86 cm^2 MEA with the round shape of the electrodes that has been tested for 5000 hrs. (UC024). This cell also outperformed the subscale test with 86 cm^2 cell (UC031) with the square shape of electrodes. The voltage degradation rate at the conclusion of the test was calculated to be 41 µV/hour, meeting the program goal of less than 50 µV/hour. This rate is also similar to the one measured on the sub-scale cell (UC024) (35 µV/hour) and better than the 86 cm^2 cell with square shape of the electrodes (UC031) (80 µV/hour), estimated at the same test time.

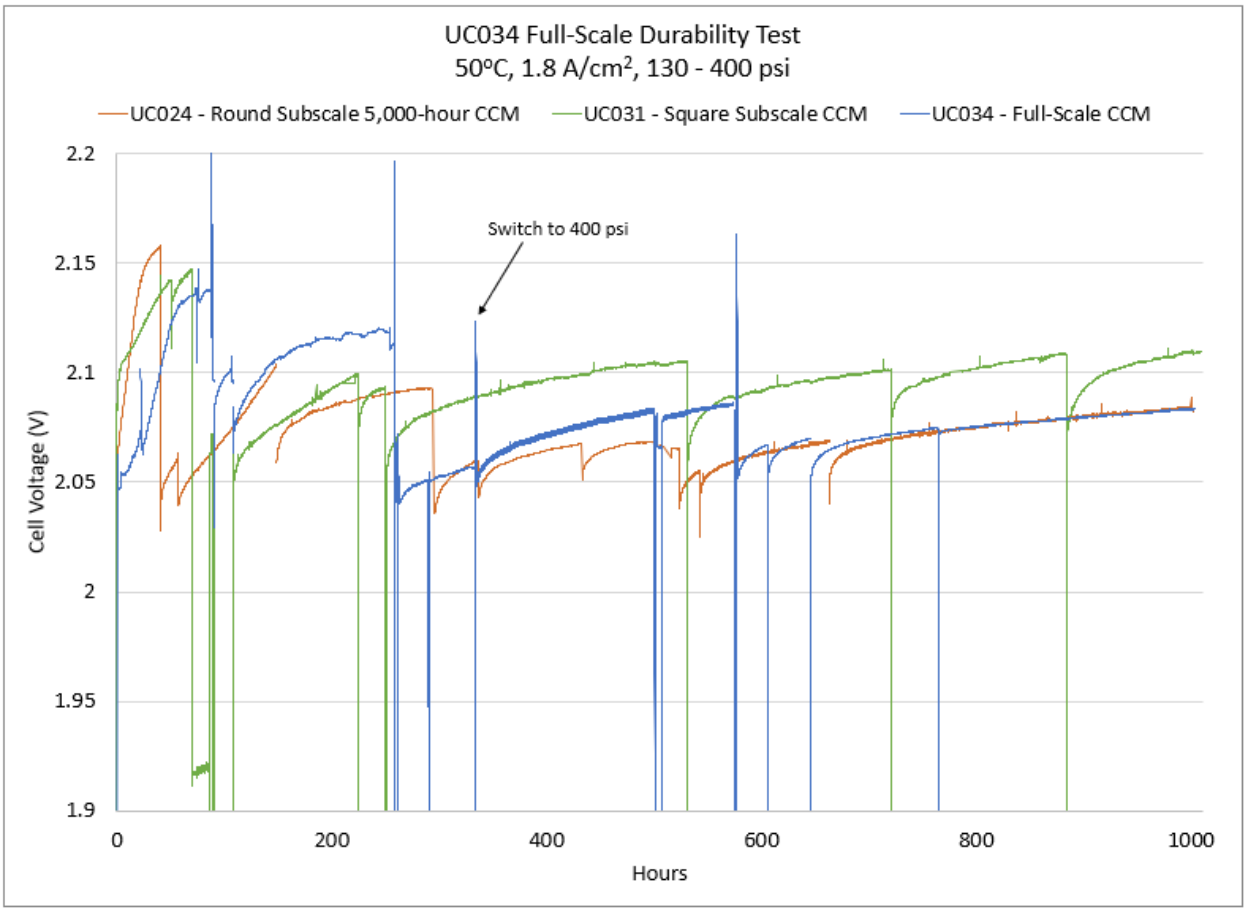

Figure 34. Comparison of the steady-state cell voltage transients of the large-scale 680 cm^2 CCM (UC034) with the ones measured with sub-scale (86 cm^2) CCMs with round shape of the electrodes (UC024) and square shape of the electrodes (UC031). All cells are tested at 50ºC and 1.8 A/cm^2.

Polarization curves were measured after every 250 hours of operation and after periods of dormancy. The polarization curves collected early in the test indicated mass transport limitation at higher current densities that has been observed in other CCMs during the break-in period. The upward curvature in the polarization curves at high current densities, was observed in the curves measured beyond 250 hours of operation but is not observed in the curve measured after 500-hours of operation. The polarization curves measured after 750-hours and 1,000-hours of operation are

linear, showing that the cell has been fully activated. This data agrees with the steady state trend, which would suggest the cell was still breaking in till almost 600 hours. The polarization curves measured after various times of operation are compared in Figure 35.

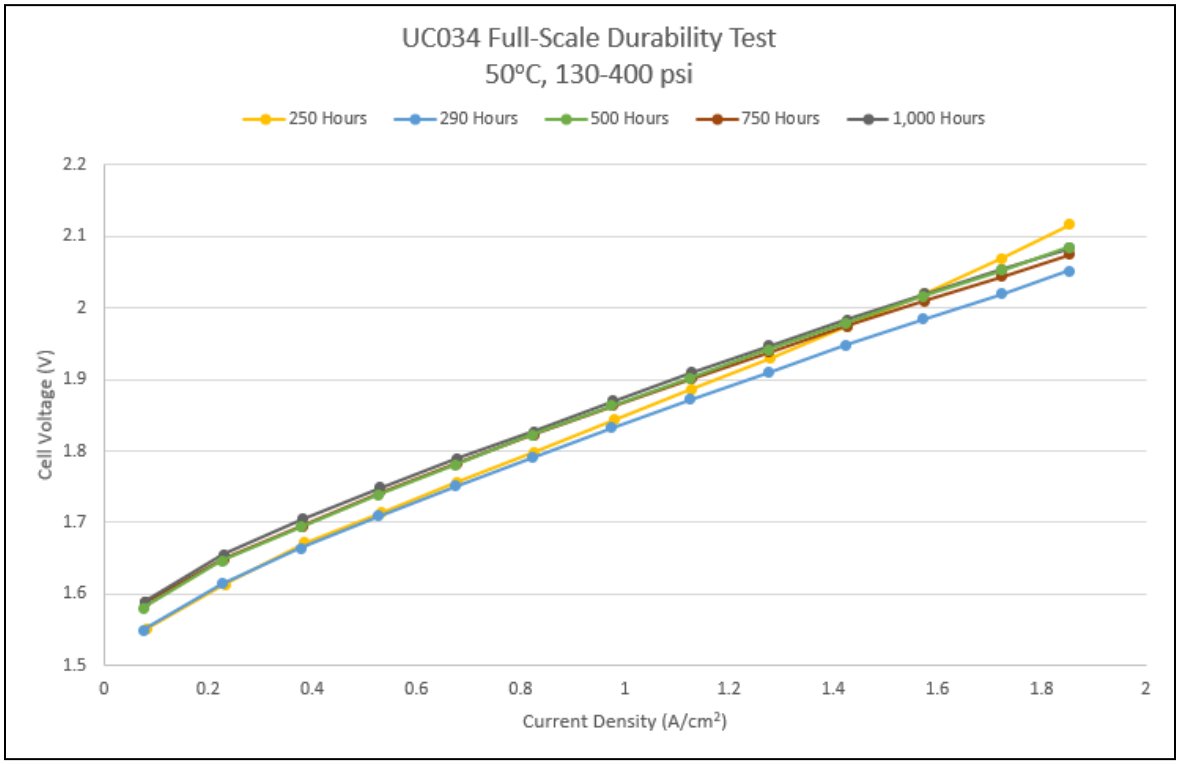

Figure 35. Polarization curves measured on 680 cm^2 cell (UC034) after various times of operation at 50°C and 400 psi. Curves before 500 hours were generated at ~130 psi.

This 680 cm^2 test represents successful completion of the program's final deliverable. In addition, we performed a comprehensive pre- and post-test analysis of the RSDT fabricated MEA with geometric area of 680 cm^2 and dual recombination layer design (UC034). This study intended to understand the governing degradation mechanisms that control the durability performance of the 680 cm^2 CCM. The main findings and conclusions from the analysis are as follows:

Pre-test Characterization

In this investigation, we have used advanced techniques and methods for physical and chemical characterization, such as ICP, ultramicrotome, HRTEM, HAADF STEM, STEM EDS mapping, SEM, and EDS mapping. All the tests were performed on samples cut from "as fabricated" 680 cm^2 MEA (UC034).

Figure 36 shows the SEM cross-sectional images of the MEA before the steady-state operation. Figure 36 (a) shows that the pre-test thickness of the anode CL is 2-2.5 μm, while the pre-test thickness of the cathode CL is 16-19μm. In addition, the two recombination layers are clearly seen in Figure 36 (a), confirming the dual RL design. The SEM images at higher magnification

presented in Figures 36 (b-c) show the morphologies of the IrOx anode catalyst and carbon-supported Pt/C cathode catalyst layer.

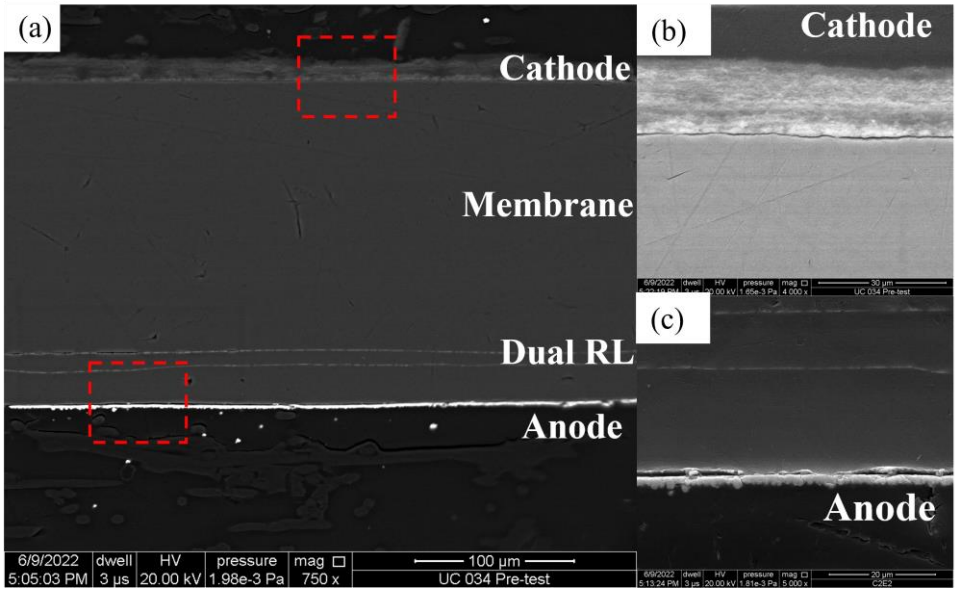

Figure 36. (a) SEM cross-sectional image of the MEA (UC034) before the durability test. The two recombination layers are sprayed on the N117 membrane and are closer to the anode side. (b) SEM image of the cathode catalyst layer. (c) SEM image of the anode catalyst layer.

ICP analysis of fabricated large-scale MEA

The platinum loading in the cathode was estimated by ICP-OES on coupons deposited during the RSDT deposition. The coupons are with average Pt loadings of $0.18 mg_{Pt}/cm^2$. The iridium loading in the anode was also estimated by ICP-OES on coupons deposited during the fabrication process. The estimated average Ir loading in the anode catalyst layer is $0.3 mg_{Ir}/cm^2$.

TEM analysis of samples from the MEA before the test.

Figure 37 presents STEM images and EDS maps of the anode catalyst layer before the test. It is seen that the pre-test IrOx anode catalyst layer is with a thickness of 2-2.5 µm (see Figure 37 (a, b)). Figure 37 (a, b) shows that there is a clear boundary between the catalyst layer and membrane. The uniform distribution of F and Ir in Figure 37 (c, d) suggests that the Nafion^{tm} ionomer is well-dispersed in the IrOx CL.

The HAADF-STEM images and EDS maps of the Pt/C cathode catalyst layer before the steady-state cell operation are presented in Figure 38. The porous structure of the Pt/C electrode is evident from the images presented in Figure 38 (a, d-f). The STEM image presented in Figure 38 (d) shows the absence of nanoparticles in the volume of the membrane on the cathode side. Figures 38 (b, c) show the STEM-EDS elemental maps and the compositional line profile analysis of nanoparticles in the cathode. These figures show that only Pt and F are present in the cathode CL. No Ir signal is observed in STEM-EDS-maps of the cathode.

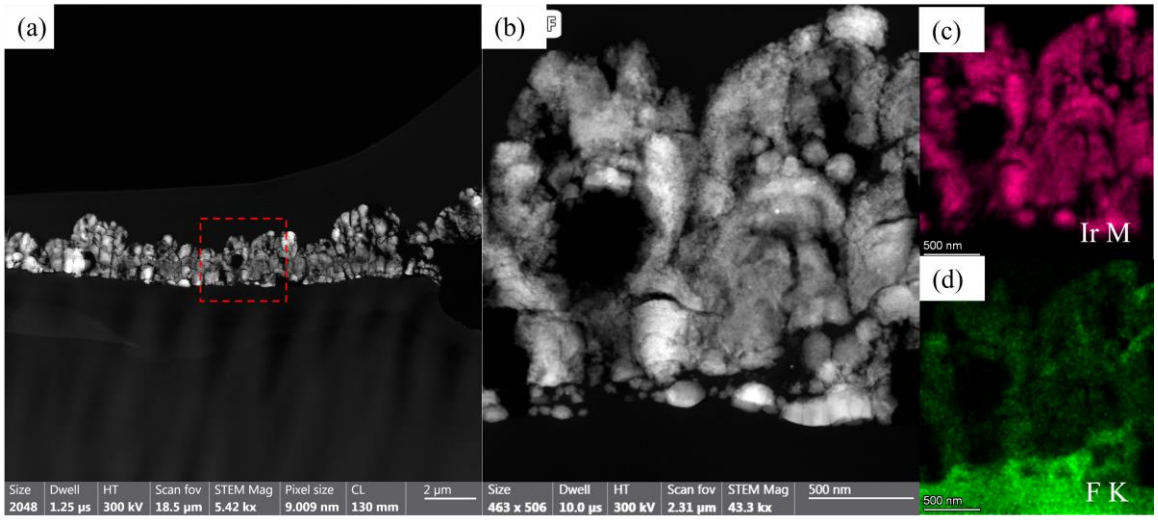

Figure 37. (a, b) STEM images of the pre-test anode catalyst layer. (c, d) EDS elemental maps of Ir and F.

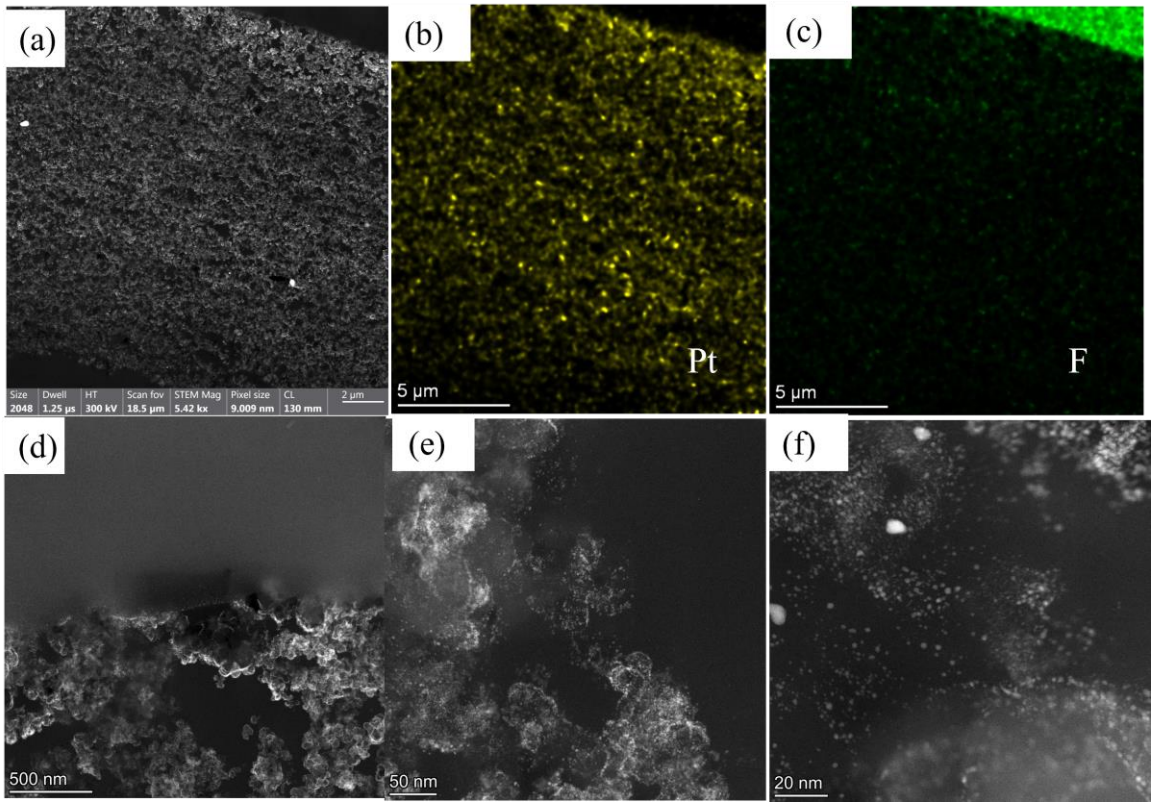

Figure 38. (a) STEM image of the pre-test cathode layer. (b, c) EDS elemental maps of Pt and F. (d-e) High-resolution STEM images of Pt in the cathode catalyst layer.

SEM analysis of the MEA after the 1000 hours test

Figure 39 shows the SEM cross-sectional images of the MEA after 1000 hours of steady-state operation at 1.8 A/cm^2, 50˚C, and 400 psi differential pressure. The estimated thickness of the anode CL after the test is 1-1.5µm, while the thickness of the cathode CL is 13-16µm (see Figure 39 (a)). In addition, the two recombination layers are clearly seen in Figure 39 (a). No membrane thinning is observed in Figure 39 (a). Figure 39 (a) shows that small cracks are observed in both catalyst layers, which may be attributed to the compressive forces that are observed during the hardening step of the epoxy resin used for sample preparation for cross-sectional imaging. The higher magnification SEM images presented in Figure 39 (b-c) show that the carbon-supported Pt/C cathode catalyst layer and the morphology of the IrOx anode catalyst layer are preserved after 1000 hours of operation.

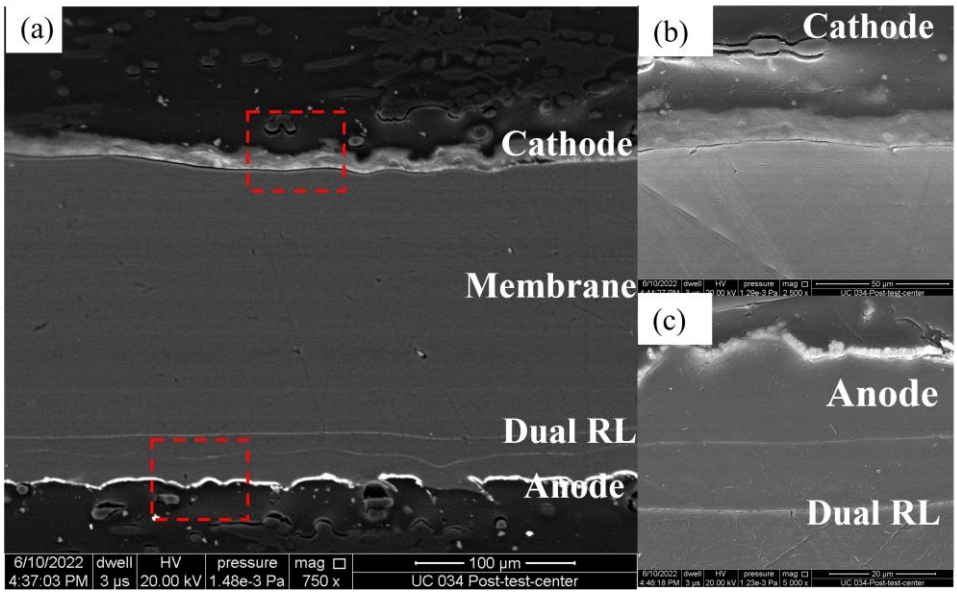

Figure 39. (a) SEM cross-sectional image of MEA UC034 after the durability test. The dual recombination layers are sprayed on the N117 membrane closer to the anode side. (b) SEM image of the cathode catalyst layer. (c) SEM image of the anode catalyst layer.

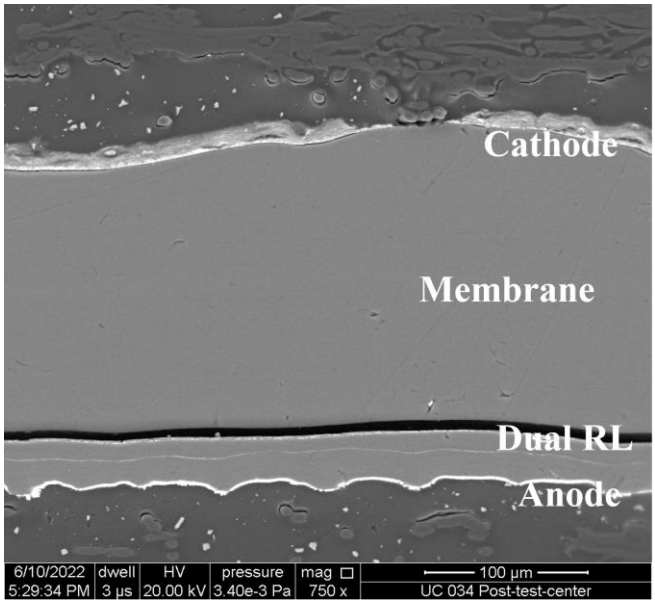

Figure 40. SEM cross-sectional image of UC034 peeled-off area after the durability test.

Figure 40 shows a cross-sectional SEM image of a sample from area that has been peeled-off during the disassembly process after 1000 hours of steady-state operation at 1.8 A/cm^2, 50 ˚C, and 400 psi differential pressure. It is seen that there is detachment between the N117 membrane and RSDT fabricated Nafion^{tm} separation layer.

TEM post-test analysis of the large scale 680 cm^2 MEA (UC034)

Figure 41 presents STEM images and EDS maps of the anode catalyst layer after the 1000 hours test. It is seen from Figures 41 (a, b) that the IrOx anode catalyst is with a thickness of 1-1.5 µm. This figure also shows that iridium is dissolving during the durability test and forms an Ir band in the volume of the membrane. The density of the Ir in the band is higher in the membrane volume adjacent to the anode and decreases with increasing the distance from the anode catalyst layer. Figure 41 (c, d) presents the STEM-maps for Ir, and F. Figure 42 compares the extent of IrO_x anode catalyst layer dissolution in a cell that was tested for 3000 hours at steady-state conditions (cell UC031) and our previous cell tested for 5000 hours at steady-state conditions (cell UC024) at the same test condition. The Ir band in UC034 is thinner and less dense than the one observed in cell UC024. This observation indicates that the dissolution of the Ir from the anode is a continuous process. Accordingly, the thickness of the Ir band in the membrane is defined by the operating cell voltage that determines the Ir catalyst's dissolution rate, the maximum concentration of Ir ions in the membrane, and the diffusion coefficient of the Ir ions into the membrane. After the Ir band, the Ir ions continue to migrate into the membrane and even reach the cathode side where they are re-depositing in the entire cathode volume.

Figure 43 presents STEM images of the recombination layers after the test. Both RLs are clearly seen in this image. Both RL are not continuous and are with thicknesses of 50 nm (Figure 43 (b, c)). The high-resolution images presented in Figures 43 (b, c) show the morphology of the post-test Pt recombination layers. Pt particles are observed around the recombination layers. It is interesting to point out that the Pt recombination layer 1 becomes less dense in comparison to RL2, after the test.

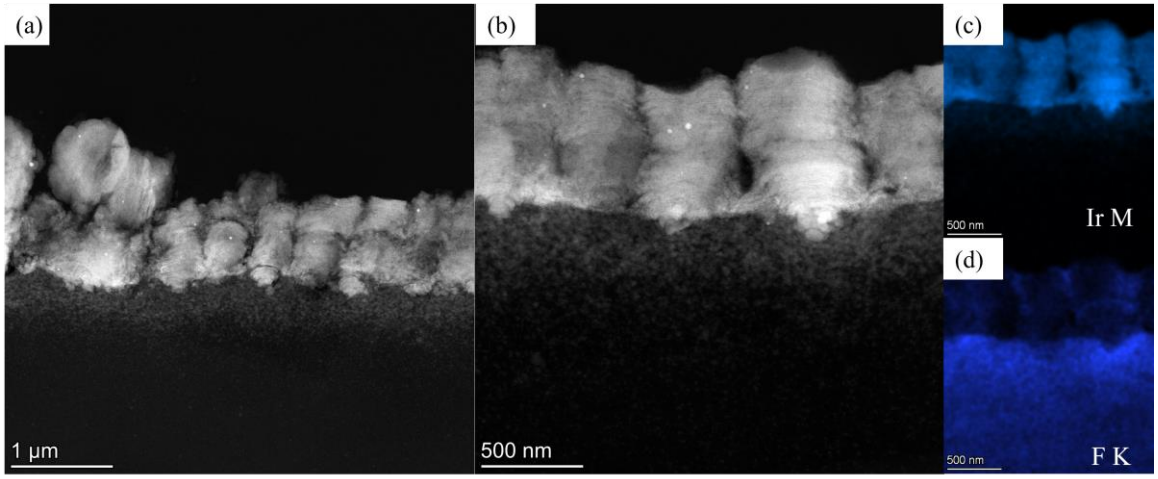

Figure 41. (a-b) STEM images of the anode catalyst layer after the test. (c-d) EDS elemental maps of Ir and F.

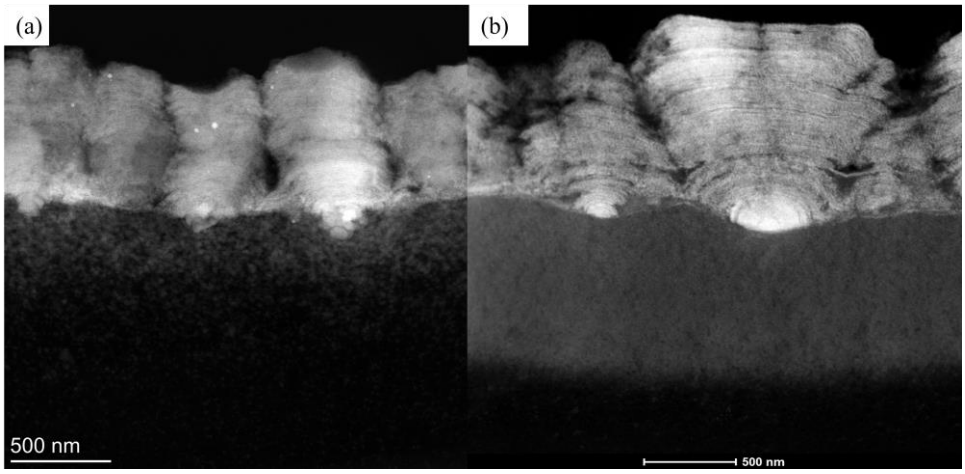

Figure 42. (a) STEM image of the 3000 hours post-test UC031 anode catalyst layer and Ir band (b) STEM image of the 5000 hours post-test UC024 anode catalyst layer and Ir band.

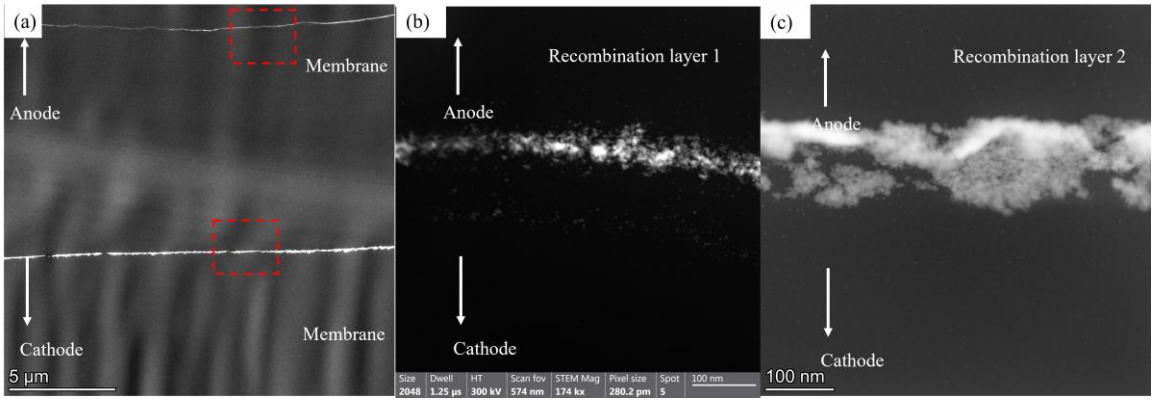

Figure 43. STEM images of the post-test recombination layer (a) High-resolution STEM images of the Pt recombinant layer 1 (closer to the anode). (c) High-resolution STEM images of the Pt recombinant layer 2.

The HAADF-STEM images and EDS maps of the Pt/C cathode catalyst layer after 1000 hours of steady-state cell operation are presented in Figure 44. The STEM images presented in Figure 44 (a-c) clearly show the presence of nanoparticles in the volume of the membrane on the cathode side. Figure 44 (d-g) shows the HAADF-STEM-EDS maps and the compositional profile analysis of nanoparticles in the cathode. This figure shows that both Pt and Ir are present in the nanoparticles, which is different from the pre-test cathode TEM images. This observation confirms that the Ir is dissolving from the anode CL, diffuses in the membrane, forms Ir band, and migrates and reaches the cathode CL, where it is redeposited in the volume of the cathode.

Another important observation is that the average Pt nanoparticle size in the cathode CL increased after 1000 hours of operation. The high-resolution HAADF-STEM images of the nanoparticles formed in the membrane are presented in Figure 44 (b-c). This figure shows that the average particle size after the durability test is 3-4 nm, while the average particle size before the test is 2 nm. This indicates that Pt re-deposition and coalescence occur in the cathodes during the long-term steady-state test, resulting in reduced Pt utilization and loss of mass activity.

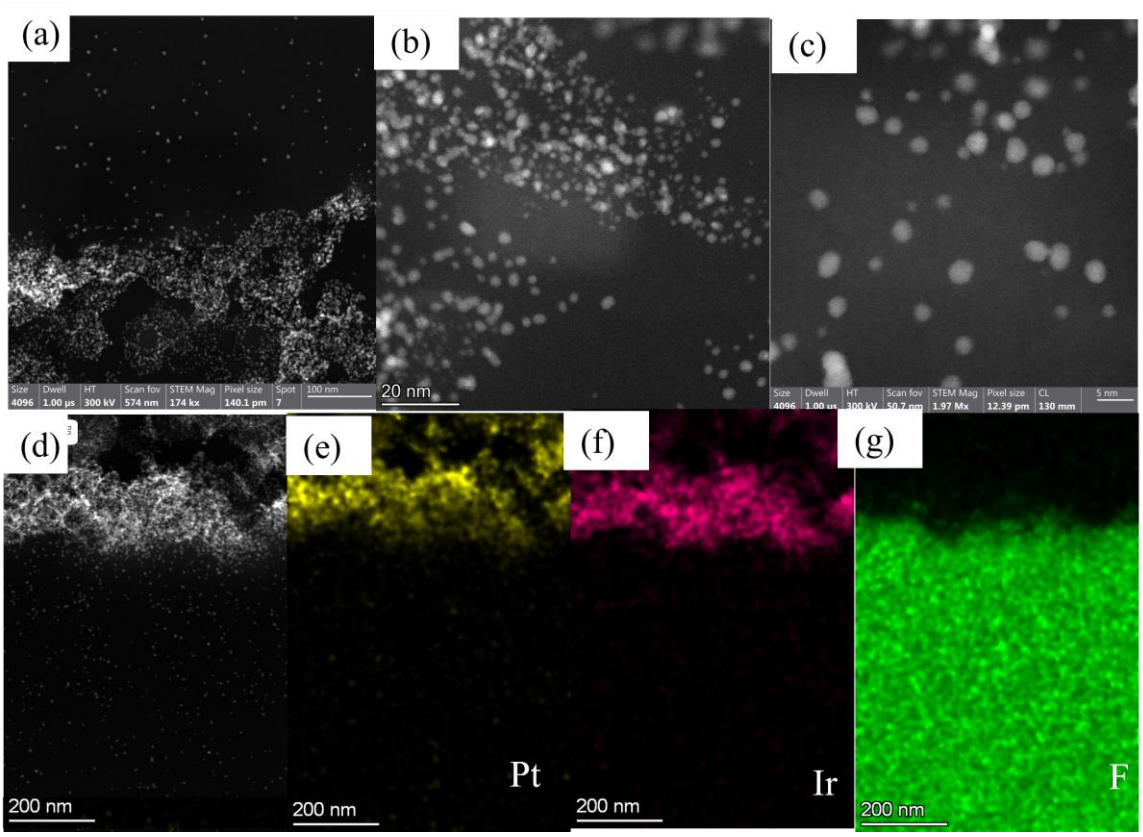

Figure 44. (a) STEM image of the post-test cathode catalyst layer, (b, c) High-resolution STEM images of the Pt in the cathode catalyst layer, (d) EDS-mapping location, (e-g) EDS elemental maps of Pt, Ir, and F.

3.3. Strategies for future improvement of the activity and stability performance of RSDT fabricated CCMs for PEMWEs.

In the final stage of the project, a subscale RSDT-fabricated CCM using Nafion N212 (2-mil thick) membrane, has been fabricated and tested at Nel Hydrogen for up to 1,000 hours. The CCM (UC036) consisted of the two-layer recombination layer design deposited onto a Nafion N212 membrane with an RSDT-fabricated Pt/C cathode and IrOx anode. The cell was tested at 50°C and 1.8 A/cm^2 with 400 psi differential hydrogen pressure. The complete steady state durability performance is presented below in Figure 45. At the end of the test, UC036 was operating at 1.862 V. This represents a 239mV improvement compared to UC031 (7-mil thick membrane) and a 135mV improvement compared to UC035 (5-mil thick membrane) with the same operating time. The voltage degradation at the end of the test was measured to be 64 μV/hr, which falls between the degradation rates of UC031 (80μV/hr) and UC035 (41μV/hr).

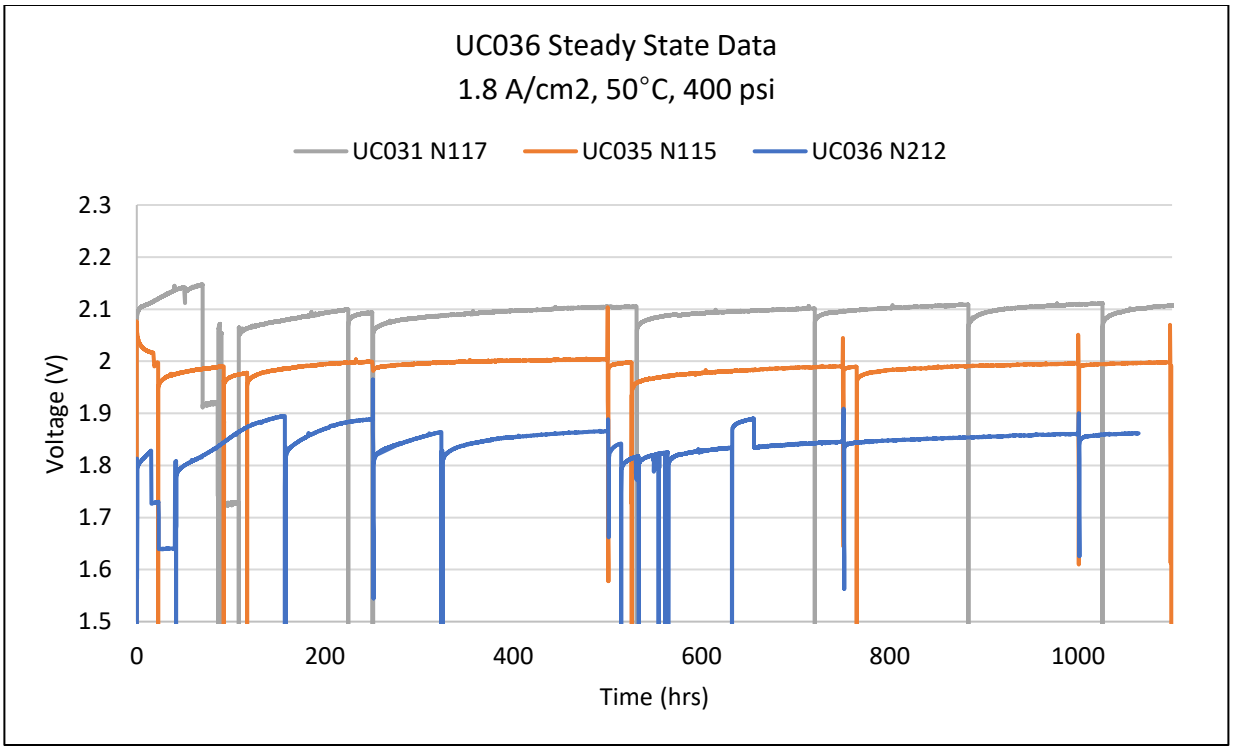

Figure 45. Steady state operating performance of RSDT fabricated MEA (UC036) with N212 membrane, compared with UC031 (N117 membrane) and UC035 (N115 membrane). All tests were conducted at 50°C and 1.8 A/cm^2.

In addition to the steady state operation, the hydrogen crossover rate was measured before and after the test as shown in Figure 46. The crossover was measured by reading the hydrogen content in the anode outlet as a percentage of the lower flammability limit of hydrogen in oxygen. This test was measured at 1.86 A/cm^2, 1.16 A/cm^2, and 0.58 A/cm^2. Following the steady state operation, the hydrogen content at 1.86 A/cm^2 was measured at 6.9% of the LFL compared with 5.9% at the start of the test. At 1.16 A/cm^2, the hydrogen content increased from 6.9% at the beginning of life to 7.3% after 1,000 hours of operation. At 0.58 A/cm^2, the hydrogen content increased from 7.2% at the beginning of life to 8.0% after testing. The results are presented in Figure 46. This minimal increase in hydrogen crossover at all current densities shows that the two-layer recombination layer design developed by RSDT, has maintained its effectiveness in reducing H_2 gas crossover for the duration of the long-term test despite a much thinner membrane.

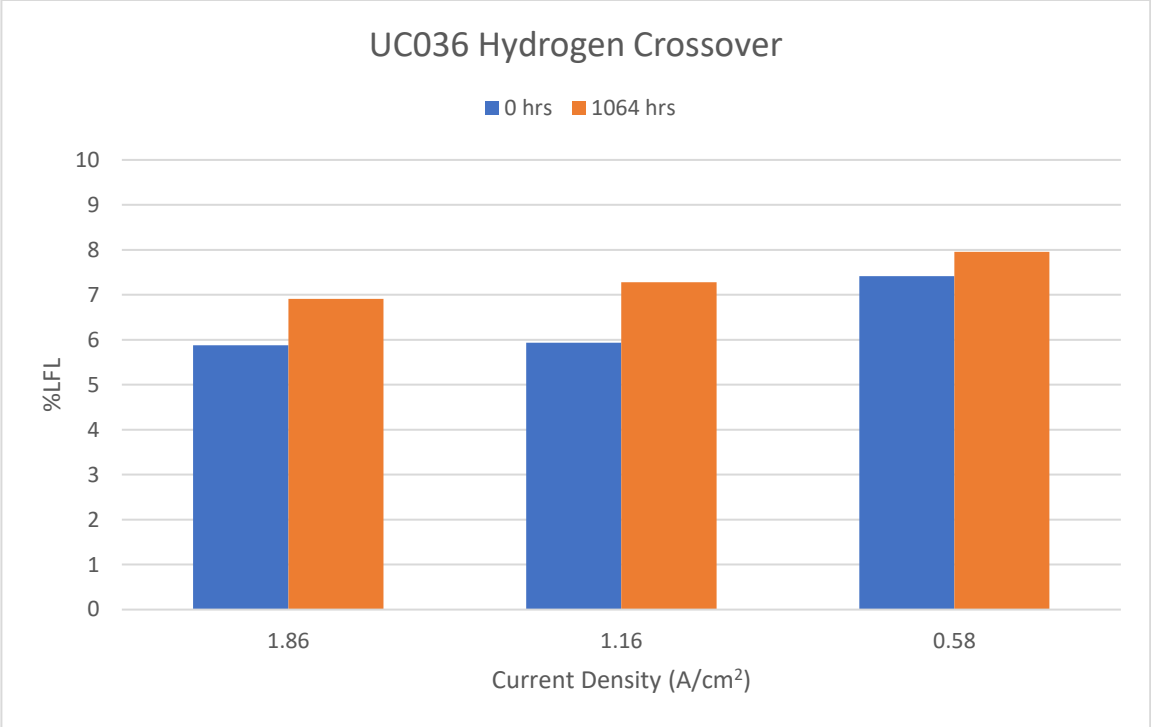

Figure 46. Measured hydrogen crossover of cell UC036 before and after test as a percentage of the lower flammability limit of hydrogen in oxygen. Measurements were collected at 400 psi and 50°C.

The hydrogen crossover can also be compared to the RSDT-fabricated CCMs containing two-layer recombination layers on Nafiontm N117 (UC031) and Nafion^{tm} N115 (UC035) membranes. As shown in Figure 47, the hydrogen crossover observed with UC036 is comparable to both UC031 and UC035, despite having a 71% and 60% reduction in membrane thickness, respectively. This indicates that, despite the thinner membranes, the RSDT-fabricated two-layer recombination layer remains capable of significantly reducing hydrogen crossover through the membrane.

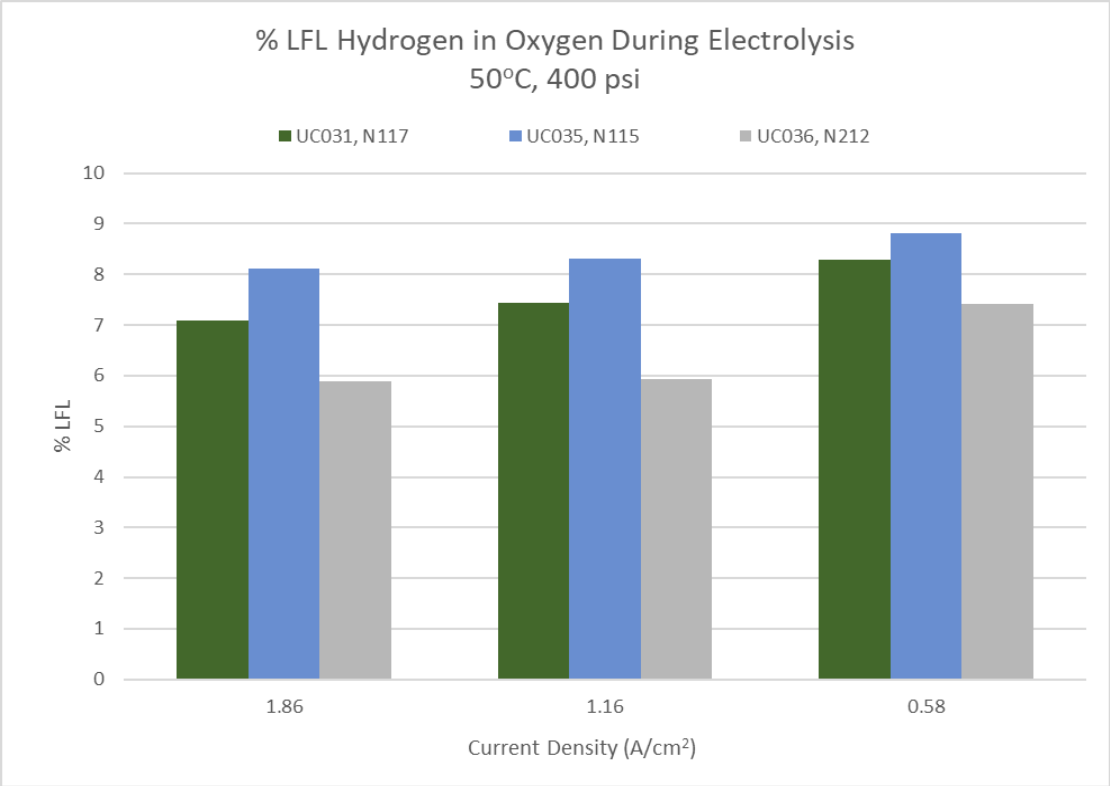

Figure 47. Measured hydrogen crossover comparison of UC031 (7-mil membrane), UC035 (5-mil membrane), and UC036 (2-mil membrane)

During the steady state operation of cell UC036, polarization curves were collected at every 250-hour interval and are presented below in Figure 48. During the 250-hour and 500-hour polarization curves, an upward curvature was observed at higher current densities suggesting a mass transport resistance during the break-in period. This phenomenon has been observed in previous RSDT CCMs, including the full-scale RSDT CCM, UC034, discussed above. After the 500-hour polarization curve, the curves become linear at higher current densities to suggest that the cell has fully broken in. The break-in period measured in the curves matches well with the steady state operating trends. The steady state voltage appears to change with each restart during the first 500 hours and becomes more consistent after that.

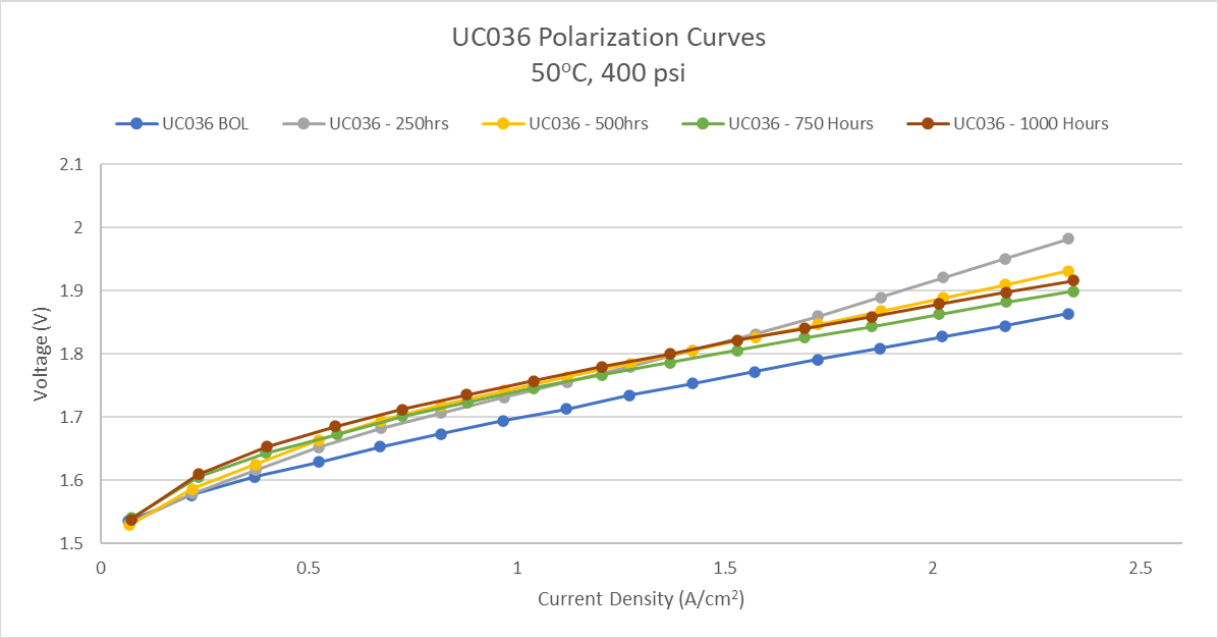

Figure 48. Polarization curves of cell UC036 measured at beginning of life (BOL), and after 250 hours, 500 hours, 750 hours, and 1000 hours of steady state operation

Summary

In this project we successfully demonstrated the capabilities of the RSDT to fabricate large-scale CCMs for advanced PEMWEs that have one-order of magnitude lower PGM loading in their catalyst layers, and performance comparable with the commercial state-of-the-art CCMs. The RSDT is a unique methodology that combines the catalyst synthesis and CCM fabrication in one step and reduces dramatically the time for CCM manufacturing. As fabricated large-scale CCMs with geometric area of 680 cm^2 demonstrated excellent activity and durability performance, and the novel duo recombination layer design paves the way for solving the safety concerns related to PEMWEs systems. In addition, excellent activity and durability performance has been demonstrated with RSDT fabricated CCMs with thinner membranes and duo RL design. This is a novel approach for further performance improvement of the MEAs for PEMWEs that has been successfully demonstrated for the first time in this project. All tasks have been executed promptly, and all project's milestones, objectives, and Go/No-Go decision, have been achieved successfully.

4. Development of in-line optical quality control system. (Mainstream Engineering-subcontractor)

In addition to the reported activities on fabrication of advanced large-scale CCMs for PEMWEs with 10 times lower PGM loadings in their catalysts layers, in the frame of this project, Mainstream Engineering developed a quality control system to determine catalyst loading and defects in real-time during the RSDT fabrication process. Catalyst loading calibrations were developed in a static test stand using completed anode and cathode catalyst layers and compared to ICP analysis. A vision system setup was planned, fabricated, and installed in a vertical orientation for preliminary testing. Based on the results, raster pattern, and necessity to not interfere with the process, the setup was refined and finally installed in a horizontal configuration. The system was debugged, software updated, and loading re-standardization conducted to modify the calibration to the actual operating conditions. Once complete, validation runs were conducted to verify the system was successfully installed and operating correctly. During operation, the system collects images for a 16-inch image width at the full speed of UConn's RSDT large CCM size raster pattern with a sub 250 µm resolution. Real-time and post-run analysis indicates the correct trends observed during platinum and iridium depositions as well as visualization of surface features. Secondary ICP validation demonstrates a loading calibration to within 0.03 mg Ir/cm^2 or Pt/cm^2 and defects greater than 250 µm at ± 50% nominal catalyst loading are identifiable.

The primary objectives of Mainstream's work were completed and included the following:

- Detect catalyst loading to within 0.03 mg Pt/cm^2
- Identify defects greater than 250 µm at ± 50% nominal catalyst loading
- Detect defects and catalyst properties in real-time during RSDT CCM fabrication for a 12-inch image width up to 100 ft/min
- Install the quality control machine on the University of Connecticut's RSDT system

4.1. Major Activities and Specific Objectives Achieved

4.1.1 Calibration Development

Static Imaging Setup

Optically the CCMs all have strong absorbance in the visible region with low reflectance. To obtain high quality images of the samples, a bright light and camera with a long exposure time are used. All CCM samples have been imaged in triplicate under no tension. All images were collected under a 12-inch imaging window to replicate the final development target. Excess pixels beyond the samples were cropped and a full resolution image saved for analysis. Reflectance technology has traditionally been used on flat samples with the most success.

- The equipment used for collection of images and processing of data includes a line scan camera, line scan light source, encoder, sample platform, motion system, and collection and processing hardware. A picture of the component test stand that has been modified for the new hardware is shown in Figure 49. This was used to successfully image a full scale CCM with a 12-inch image width for CCM calibration development.

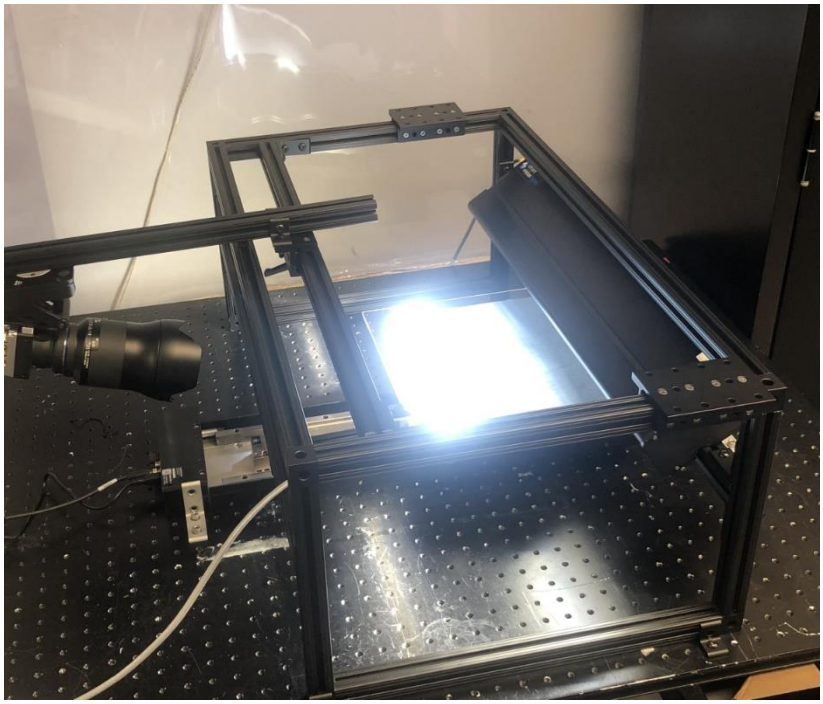

Figure 49. Mainstream's hardware test stand for UConn components

Catalyst Loading Calibration Development

Calibrations for catalyst loading were developed based on samples with a variety of catalyst loadings both across the samples and among the samples. UConn performed spot loading analyses by inductively coupled plasma techniques, which provided known reference loadings to calibrate the optical data. Calibrations were prepared for both platinum and IrOx based on imaging the area around the analyzed ICP spots and assuming similar loading surrounding them. A best fit was generated, and data was compared to the known ICP values. This t is shown compared to the ICP values both Pt and IrOx in a parity plot is shown in Figure 50 and Figure51 which indicates a good fit. The IrOx had a root mean square error of calibration of 0.02 mg_{Pt}/cm^2 and 0.03 mg_{Ir}/cm^2.

These calibrations for catalyst loading were validated using six additional samples (3 IrOx and 3 Pt), which were analyzed using the optical technique before being sent back for analysis by ICP at UConn on five different unique points including each corner and the middle. The ICP for these points were then directly compared and predicted using the developed calibrations. The samples had a linear increase over the time periods with significant variation across the samples. The calibration was applied to the samples with reasonable success as shown in the parity plot in Figure 5050. The specific spots on the 60 minute and 120-minute samples had reasonable accuracy, while the averaged area of the entire sample matched quite well.

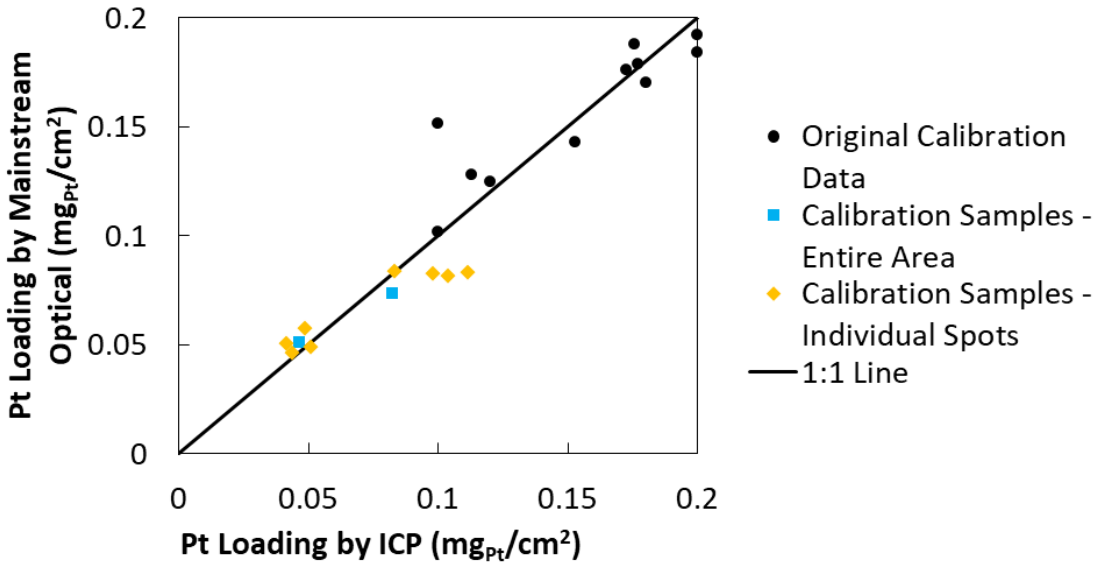

Figure 50. Loadings compared between UConn by ICP and Mainstream by optical reflectance of a set of Pt samples applied to new calibration samples on their individual spots or the entire area

The iridium oxide samples were made at 40, 95, and 150 minutes of deposition with RSDT. The samples had a linear increase from the 40 to 150-minute samples, but the 95-minute sample did not. All samples had some variation across the sample's surface. The IrOx calibration was applied to the samples with particularly good results at low loadings as shown in the parity plot in Figure51. All spots and the average of the spots were well predicted from the 40-minute sample. The specific spots on the 95 minute and 150-minute samples had weaker accuracy, but the averaged area of the entire sample matched quite well. These tests demonstrated the prediction capabilities of the developed calibrations.

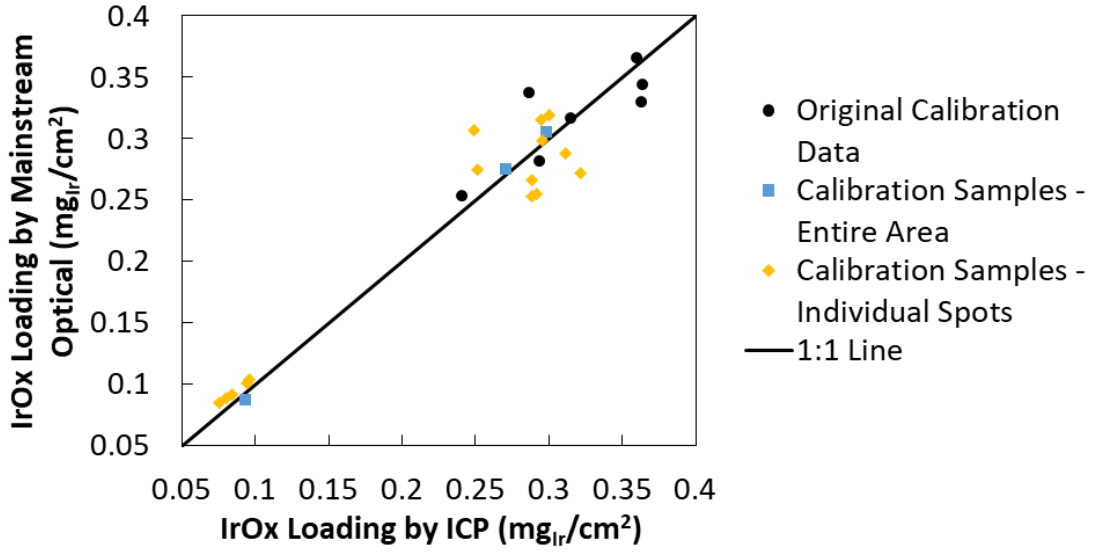

Figure 51. Loadings compared between UConn by ICP and Mainstream by optical reflectance of a set of original IrOx samples applied to new calibration samples on their individual spots or the entire area

Full-scale Sample Loading Calibration

Calibration for catalyst loading based on multiple small samples was applied to partial samples from full-scale catalyst-coated membrane samples including cathodes, anodes, and combined samples. Mainstream evaluated the samples and compared the optical measurements to known ICP values. Comparison plots are shown in Figure 5252 for three samples cut from two full-scale iridium anode samples where squares were previous calibration samples and circles are data points with known loadings from the new full-scale samples. The color of each data point corresponds to the sample. They have similar errors (i.e., 10%) compared to the sample loading. The second set of samples was evaluated and shown in Figure 153 for two samples cut from one full-scale platinum cathode sample. The squares are the previous calibrations and circles are new data points. They also have a similar error (i.e., 10%) of the sample loading. This final validation indicated the calibrations would be successful when implemented in on the RSDT hardware.

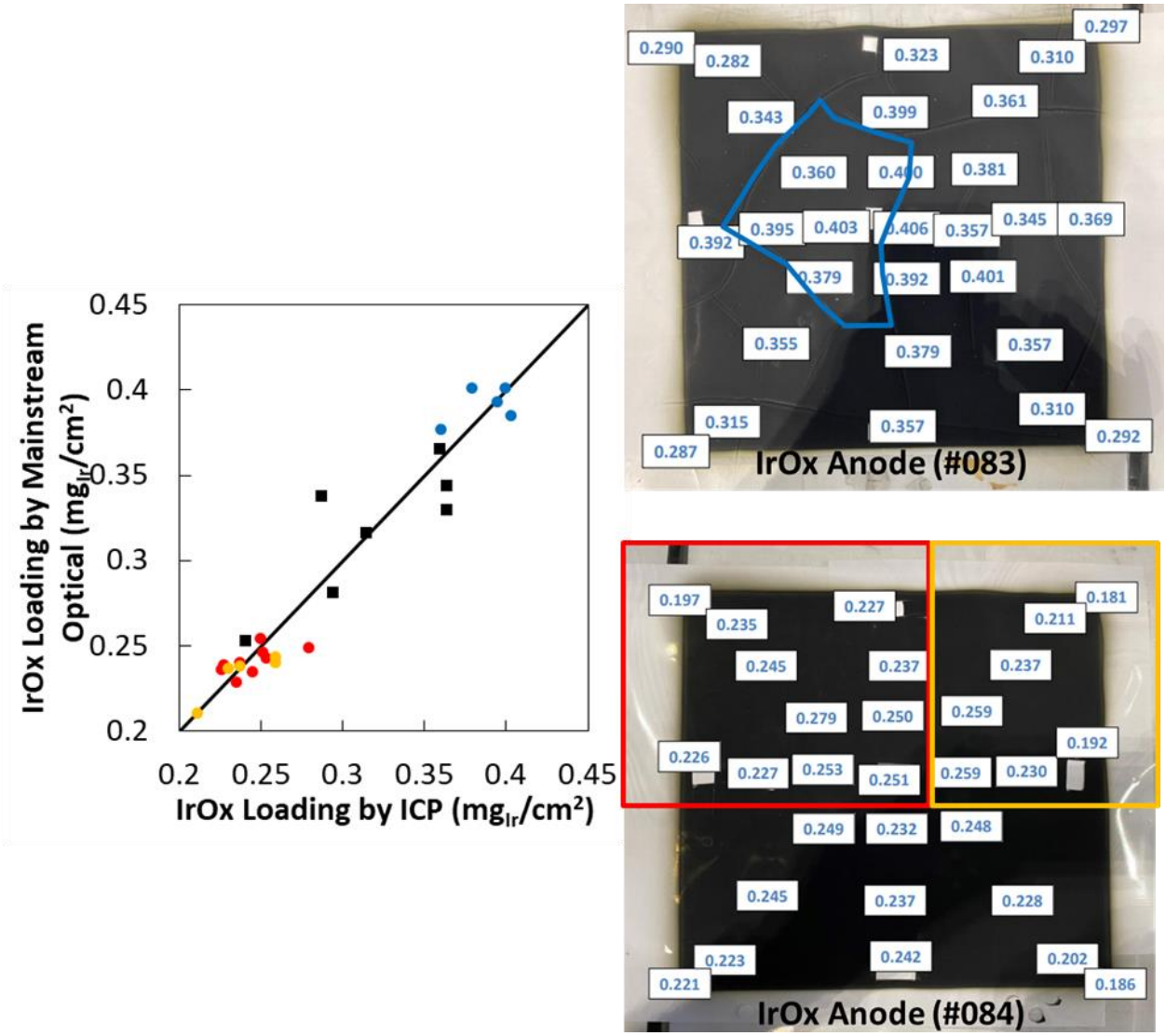

Figure 52. Loadings comparison between UConn by ICP and Mainstream by optical reflectance of a set of 86 cm^2 samples (squares) and full CCM samples (circles) for IrOx cathodes with the spot size of 1 cm x 1 cm (left), where colors coordinate to the specific regions in the optical pictures (right)

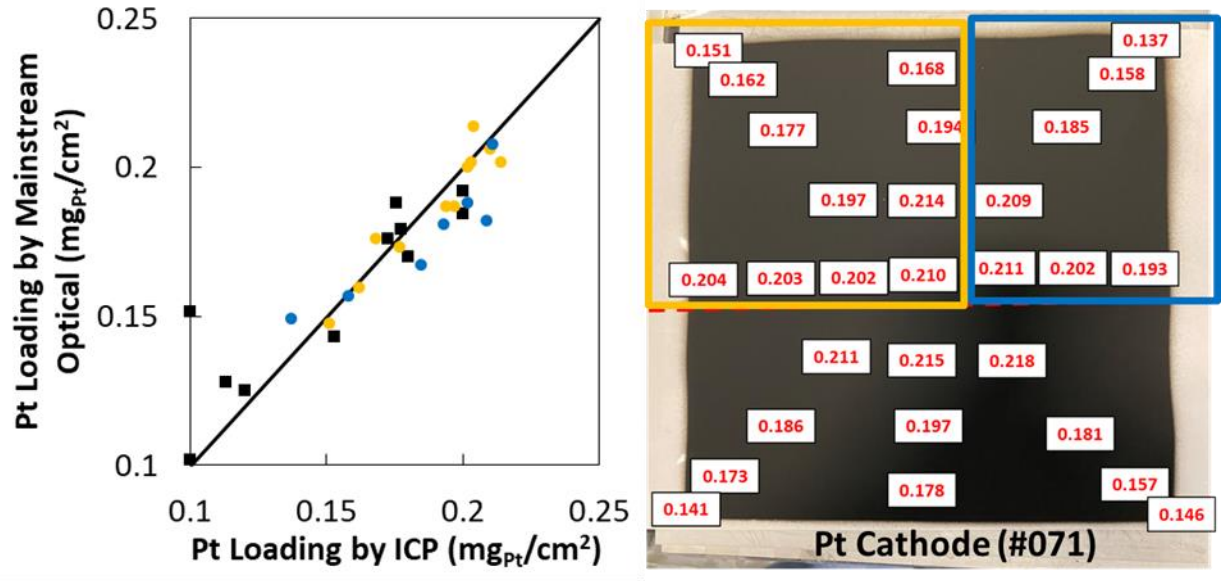

Figure 13. Loadings comparison between UConn by ICP and Mainstream by optical reflectance of a set of 86 cm^2 samples (squares) and full CCM samples (circles) for Pt cathodes with the spot size of 1 cm x 1 cm, where colors coordinate to the specific measurement regions in the optical pictures (right)

Spot Identification Indicating Minimum Size for Defect Analysis

A RSDT fabricated sample with interesting spot features was identified by UConn and analyzed by Mainstream. These samples were imaged, and the images were processed with simple optical filters (e.g., gain, contrast, brightness). Then the images had machine vision algorithms applied to them for complex transformation (e.g., open, erode, Gaussian averaging, masking, background subtraction). A threshold was then applied to the images to convert them into a binary file to highlight the spots. The spots are then characterized by size, shape, and location information based on a grid made from the top left corner of the image. This process allows for the spots to be identified and located through the software. The spots can be directly correlated and highlighted on the raw image in order to look at the area of interest. This was processed and areas between 1 – 5 pixels up to 50 pixels were identified in this manner (Figure 5454). These had significantly different optical properties and were able to be detected down to below 250 µm. This indicates the ability to detect defects down to below that resolution as well.

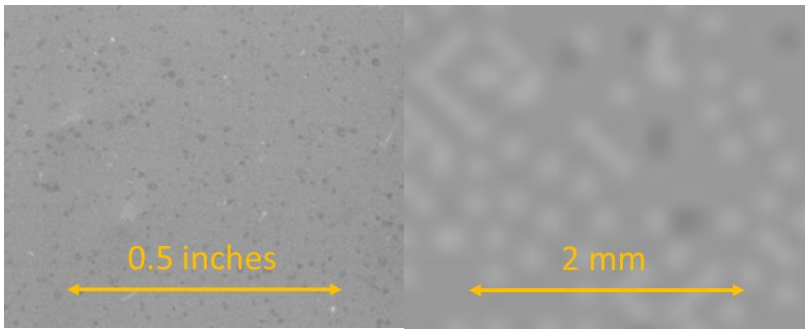

Figure 54. Raw optical reflectance image of a RSDT sample with odd spot features, zoomed in to show features smaller than 250 µm being identified

4.2. Optical Setup for the RSDT Process

The equipment used for collection of images and processing of data includes a line scan camera, line scan light source, encoder, sample platform, linear motion system, and collection and processing hardware. The line scan camera is a Basler model raL8192-80km capable of processing lines at 80 kHz and 8k resolution over a Camera Link connection. The light source is a SmartVision LCHP-600 that utilizes 144 high-power LEDs to illuminate a 12-inch linear section. The encoder, a Tru-Trac TR1, measures position at speeds of up to 3000 fpm. The encoder delivers 8192 pulses per revolution to offer 0.02 mm resolution.

This imaging configuration worked well for testing CCMs and developing the calibration and will be implemented on the RSDT process. The shroud positioning only allows for a gap of around 1.5 inches between the substrate and the shroud. This thin optical gap necessitates the line scan hardware because an area scan camera would not have sufficient space to view the entire sample. After seeing the flame operation in person and the limitations imposed by the narrow gap, two different arrangements were considered, and a high angle was selected.

4.3. Installation of the Full Scale RSDT System

Mainstream installed the quality control equipment and conducted validation tests at UConn. The system was planned to be installed with the sides of the stage aligned to the left and right of the flame at an angle of 15°. This setup allows the full catalyst coated membrane to be imaged and recorded without requiring any image stitching or modification to the existing setup. In addition, the iridium and platinum spray depositions take place at different distances between the nozzle and stage; however, the stage position relative to the flame assembly remains constant. Therefore, by positioning the camera and light in a fixed position relative to the assembly and RSDT frame, it can image during all deposition types without requiring readjustment to the focus or platform distance.

All hardware was successfully installed during the trip in the planned side orientation (Figure 5555) and images were captured at a 16-inch field of view to enable multiple passes of a full size CCM. The encoder was mounted horizontally on the back raster stage to determine when to image at the proper time. The stage passes within less than an inch of the optical hardware but does not make contact. The light is mounted to the hardware used to affix the laser beam dump, enabling minor movement between spectroscopic measurements and CCM production. All components are affixed to the exterior RSDT framing to reduce vibration as it shares no direct connection with the moving stages or flame spraying apparatus. During validation testing, the light slowly accumulated trace particulate from the flame spraying and should be cleaned after every run. The camera has a disposable glass filter on the lens that should be discarded periodically. A remote connection protocol was established that enables transferring files, updating the code, and direct access to the vision system by Mainstream.

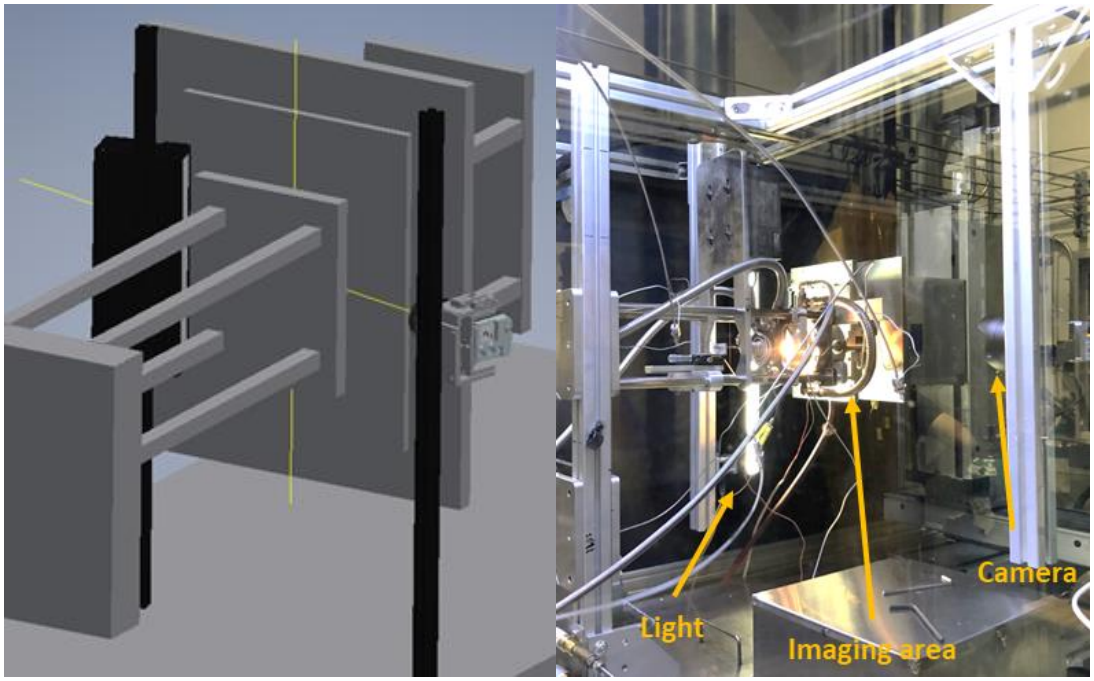

Figure 55. CAD rendering of the planned optical equipment setup on the RSDT system positioned to the sides of the flame at 15° (left) and the quality control hardware installed on the RSDT (right)

The linear light and camera were aligned to the image through the less than two-inch gap and image over the center of the part where the flame is depositing, as seen in Figure56. Due to the intensity of the light, the flame has no discernable interference on the optical images. An image of the light centered on a CCM part raised above the shroud is shown in Figure57. The linear light is on mounted, lockable swivels, while the camera is mounted onto a non-moving adjustable plate for alignment.

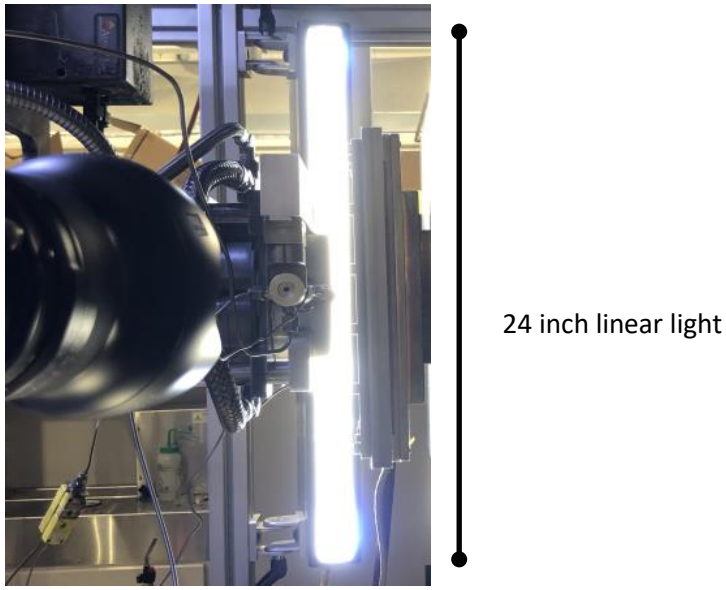

Figure 56. Image of stage and shroud in proper deposition position, showing the small gap through which, the camera is imaging

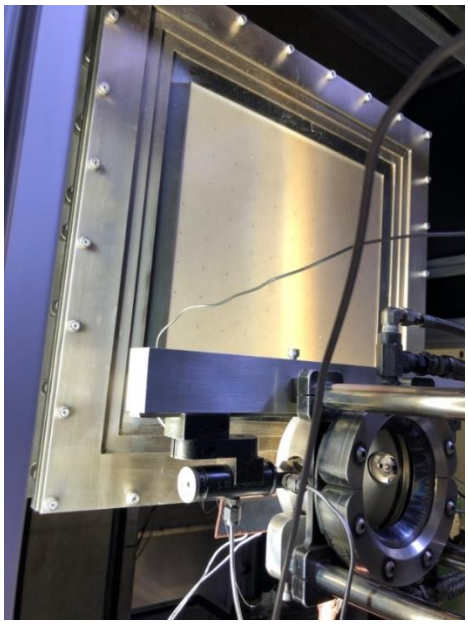

Figure 57. Image of the linear light centered on a full scale CCM before deposition where the camera is imaging

With a line scan camera, images are generated when there is movement of the stage as triggered by the encoder. As the stages raster back and forth on each horizontal move, the encoder triggers the camera to record the rate at which the stage is moving. When the stage moves left it images left to right, and when the stage moves right it images right to left. This means that every other full image is flipped along this axis. The initial plan was to count horizontal rasters per the encoder as determined by time between horizontal pulses to enable imaging every time the part was centered in the middle and moving in the same direction.

A few imaging issues were discovered as highlighted in Table 33 and were resolved to allow for clear, high-resolution images to be captured during all stages of RSDT processing. These improvements enable non-uniformities such as spotting or surface texture to be observed, while enabling the calibrations for iridium and platinum to be correctly applied based on the changing pixel intensity.

Table 3. Issues and Resolutions for Improved Optical Imaging

Issue	**Resolution**
Shadows caused by protruding screws	Switched to counterbored screws
Non-uniform lighting caused by reflective surfaces	Painted the part mask, greatly reduced reflections
Highly reflective surfaces caused LEDs to be visible	Added a holographic linear diffuser to reduce reflection
Non-uniform lighting caused by slight off-angle lighting/camera	Recording images always in the same location, background correction, and improved lighting setup
Variations in setup during setup	Improved setup procedures that were incorporated into the user manual

4.4. Image Processing – Background Correction

An example of the capabilities of a general background correction is shown in Figure58. As can be seen, most light intensity features can be removed for improved loading analysis. The algorithm used for this was the same and removed an average light intensity in the horizontal direction to remove vibration and vertical direction to remove non-uniform lighting. It maintains unique features such as spotting or surface texture non-uniformity. This adjustment maintains the same trend seen previously that indicates proper imaging and loading calibration will be effective.

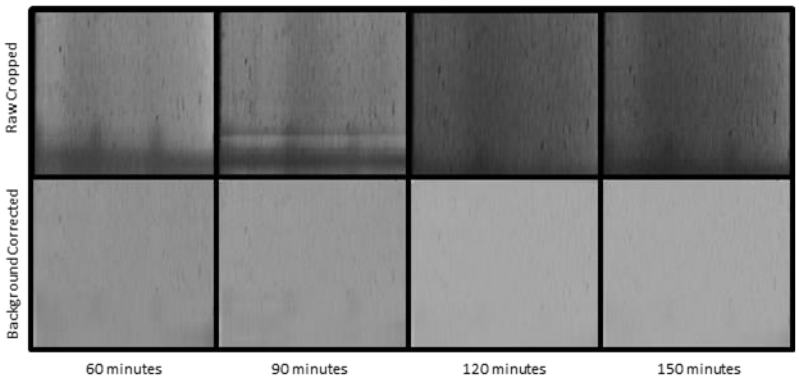

Figure 58. Example of background corrected images eliminating non-uniform lighting from cropped small CCM images collected during a platinum deposition

4.4.1. Highly Reflective Samples – Diffuser

During imaging, highly reflective samples, such as the base metal substrate and recombination layer, projected the linear LED light pattern through the sample onto the camera. This can be seen in Figure *2*59, where there are lines that appear vertical with the system and almost completely straight and unmoving. A holographic linear diffuser that only diffuses light along the long axis (to conserve intensity) was assembled to the light to distribute the light effectively and high-quality images of reflective surfaces were able to capture clearly as shown in Figure *2*59. This enabled all components to be imaged clearly.

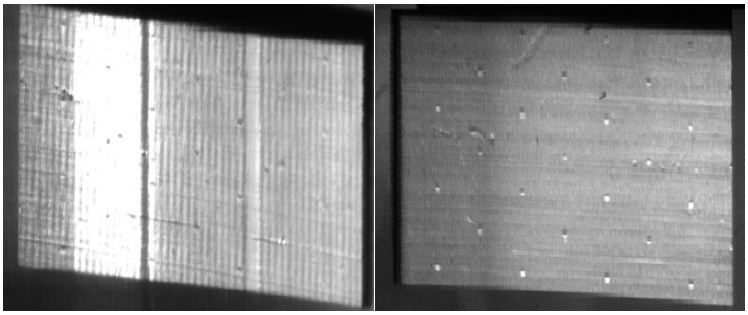

Figure 2. Raw image taken during recombination layer deposition (left) and after polarizer applied to the light (right)

4.5. Installed System –Calibration Run and Loading Analysis

With the final optical setup in place and issues resolved, a complete part was fabricated on the RSDT 2 setup and images were collected throughout the entire process for final calibration. Each layer including the 4-part recombination layer, anode, and cathode were successfully collected. The sample is rotated 180 degrees halfway through each deposition, so the anode is rotated three

times, but the part is only ever in two unique positions. During imaging it was found that variation caused by rotation was the most significant change in image quality, beyond the change due to deposition, and must therefore be adjusted or the signal drowned out. The software used a new background subtraction for when the part is rotated.

The method for this is a drop-down menu that has options that include recombination layer – platinum, recombination layer – membrane, anode – iridium oxide, cathode – platinum. Then a second drop-down menu that indicates when the part is rotated. This allowed for the software to track that the top left corner has been rotated to the bottom right corner and keep track through the deposition process. The loading is then built throughout the entire run by comparing each image to the former, instead of processing each image relative to an initial background. Based on the analysis performed and detailed later, this is a viable method to control the software with a changing optical setup due to all the required system movements.

4.5.1. 1st Anode Calibration Run

The anode deposition was conducted, and all images collected. The raw images from this run are shown in Figure 60, where the rotated images are highlighted in the red boxes. The processed images are then shown in Figure61, where a brightness and contrast filter has been applied and differences can be seen easier. As can be seen in the left of the anode and highlighted in Figure62, there is a non-uniform lighting strip that does not move when the part is rotated, providing indication it is a function of the setup and not the part itself.

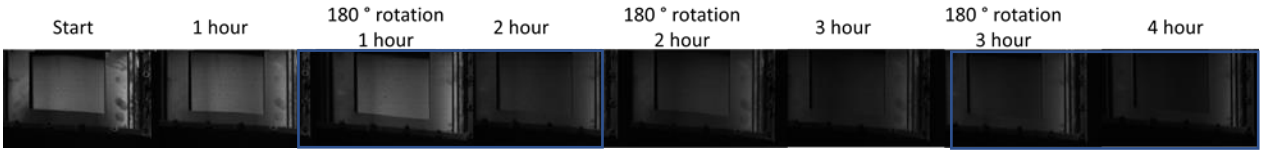

Figure 60. Raw images taken during anode layer deposition at the start and end of each continuous section

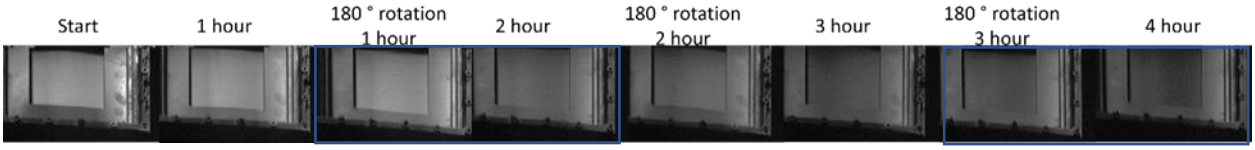

Figure 61. Processed images taken during anode layer deposition at the start and end of each continuous section all rotated to be in the same orientation

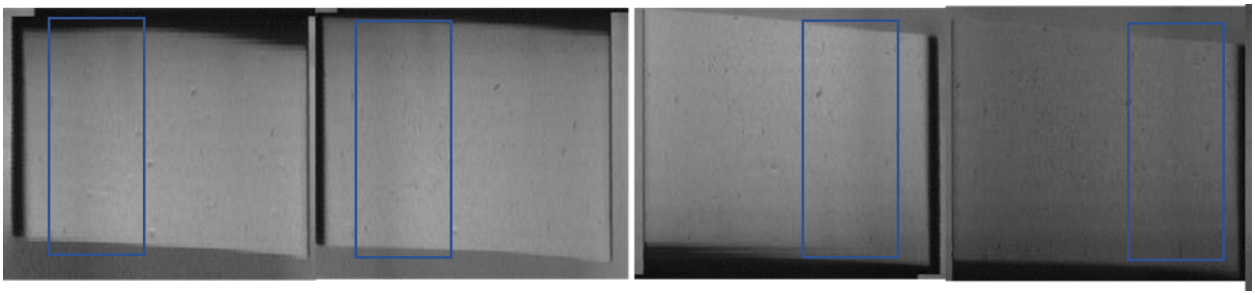

Figure 62. Processed images taken during anode layer deposition at the start and end of two continuous sections rotated to be in the same orientation and a moving shadow highlighted that is caused by lighting irregularities since it does not move with the rotated part

The final images for loading are all rotated to be in the same orientation, so the upper left is always the upper left are shown in Figure 633. The raw intensity from the four quadrants and middle are plotted with time in Figure 44. As can be seen, there are trends during deposition, and then around 60, 120, and 180 minutes there are large discontinuities, which is because the part is flipped, and different lighting conditions lead to movement. This data was then processed based on the quadratic calibrations that Mainstream had previously developed, and the background corrected as described above so when the part is rotated it resets. The loading was then applied as shown in Figure 44. As can be seen, there appears to be mostly linear deposition with an interesting change right two hours before the run.

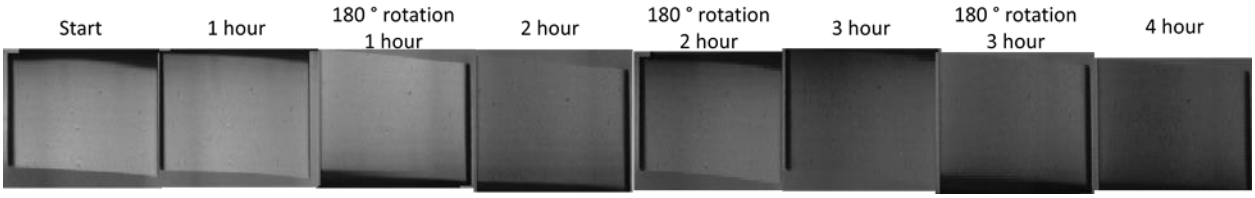

Figure 633. Processed images taken during anode layer deposition at the start and end of each continuous section all rotated to be in the same orientation and cropped to the area of interest

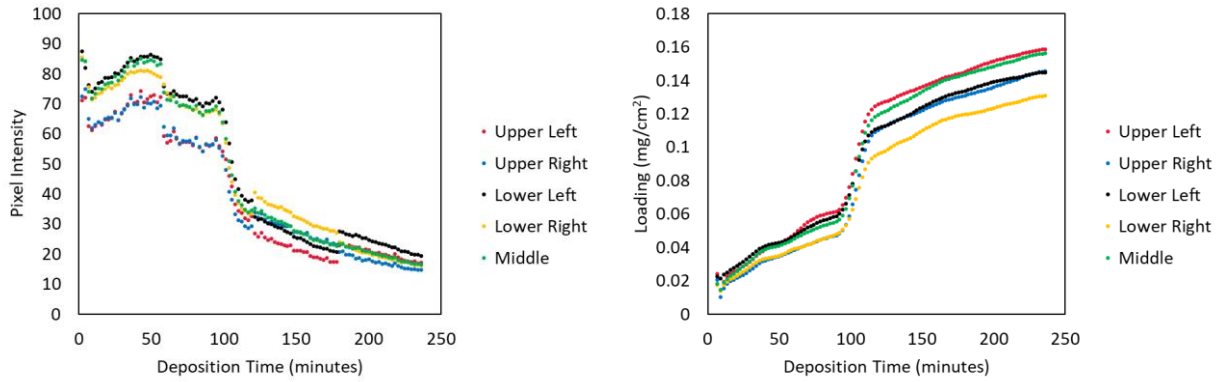

Figure 44. Raw intensity of the anode (left) and processed intensity (right) during the entire deposition in 4 quadrants and the middle, discrete movements can be seen around time 60, 120, and 180 minutes where the unit was rotated

4.5.2. 1st Cathode Calibration Run

The cathode deposition was conducted, and all images collected. The raw images from this run are shown in Figure 655 and the processed images for analysis are then shown in Figure 666. The same method of analysis was applied for the cathode as the anode with a different curve based on the images we had collected previously. The rotation issue can be seen clearly here as well in the plot of the raw image intensities in Figure67, where then the part rotates, it moves significantly in every part. The initial variety in the intensities is due to non-uniformity in the lighting of the setup. However, by performing the calibration by image-to-image differential, this non-uniformity impact is greatly reduced. The loading was then applied and is shown in Figure67. There were no large changes in this setup like was seen in the anode deposition.

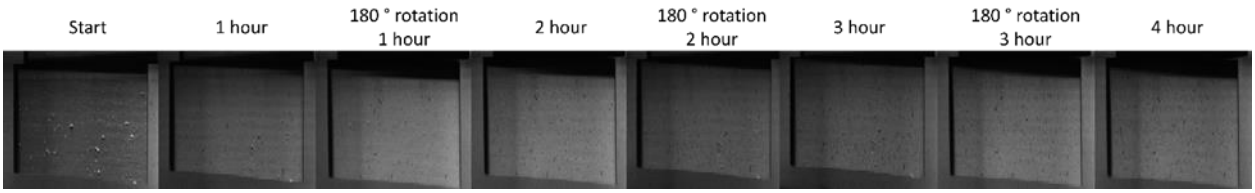

Figure 655. Raw images taken during cathode layer deposition at the start and end of each continuous section

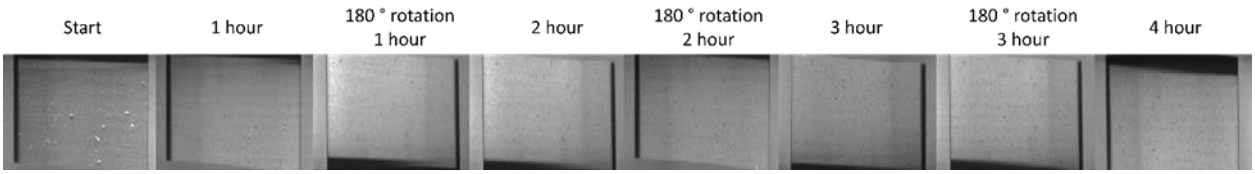

Figure 666. Processed images taken during cathode layer deposition at the start and end of each continuous section

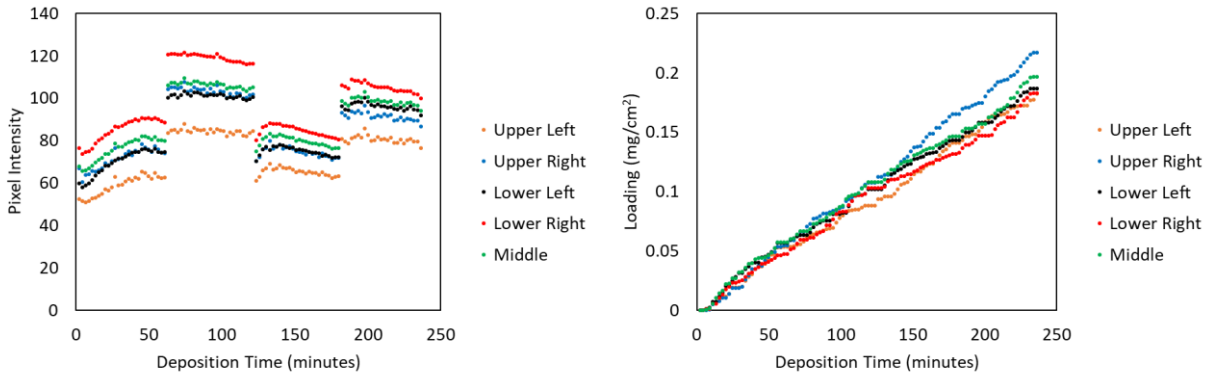

Figure 67. Raw intensity of the cathode (left) and process intensity (right) during the entire deposition in 4 quadrants and the middle, discrete movements can be seen around time 60, 120, and 180 minutes where the unit was rotated

4.5.3. Recombination Layer Calibration Run

Three of the four sections of the recombination layer deposition were successfully imaged. The raw images from this run are shown in Figure68. The membrane depositions made the image darker, while the platinum made it brighter, similar to what was seen at the start of the cathode deposition.

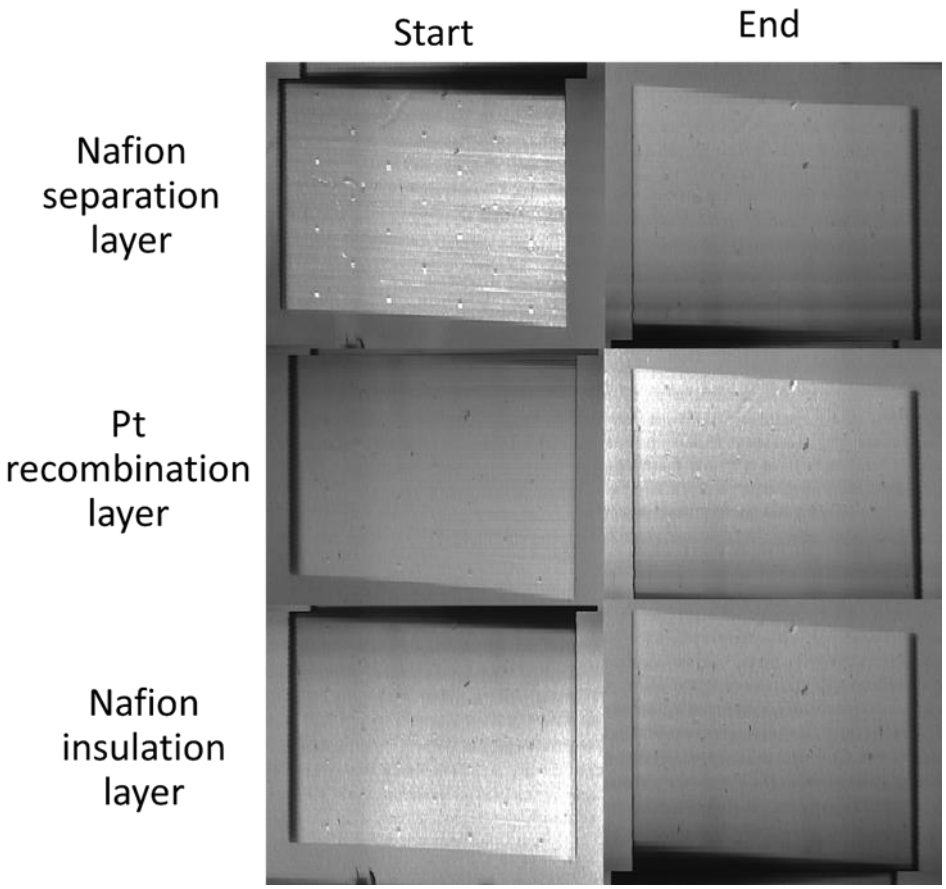

Figure 68. Raw images taken during recombination layer deposition at the start and end of each section

4.5.4. Non-uniformity Analysis

The non-uniformity analysis was conducted and is highlighted for the cathode as an example in Figure 69769. As can be seen the non-uniformity spots can be seen throughout the run and at the end, they appear to be more present. These do not appear to have any negative effect on performance.

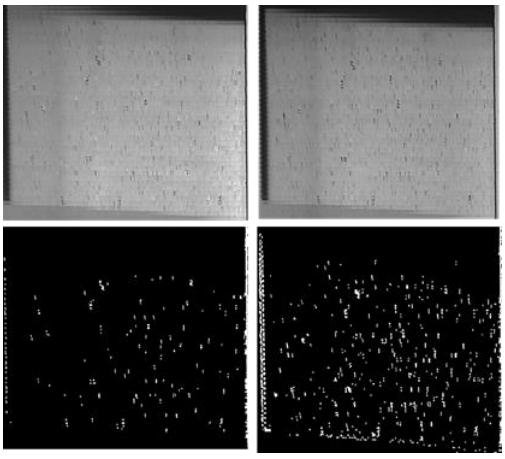

Figure 697. Spot processing to look for non-uniformities that also ignores background shadows

4.6. 2nd Anode Calibration Run – Validation

The anode deposition had an interesting nonlinearity in it that was not easily explained by the image processing software. A second deposition was conducted to determine if this trend was real or a byproduct of the imaging processing software. The first and second anode runs are shown in raw images in Figure 70870. The raw intensity from the four quadrants and middle of each run are plotted with time in Figure 71971. This data was then processed using the original quadratic calibrations that Mainstream had previously developed, and background corrected as described above so when the part is rotated it resets. The loading was then applied as shown in Figure 710. As can be seen, there appears to be mostly linear deposition with an interesting change right before two hours into the run, just like in the 1st run.

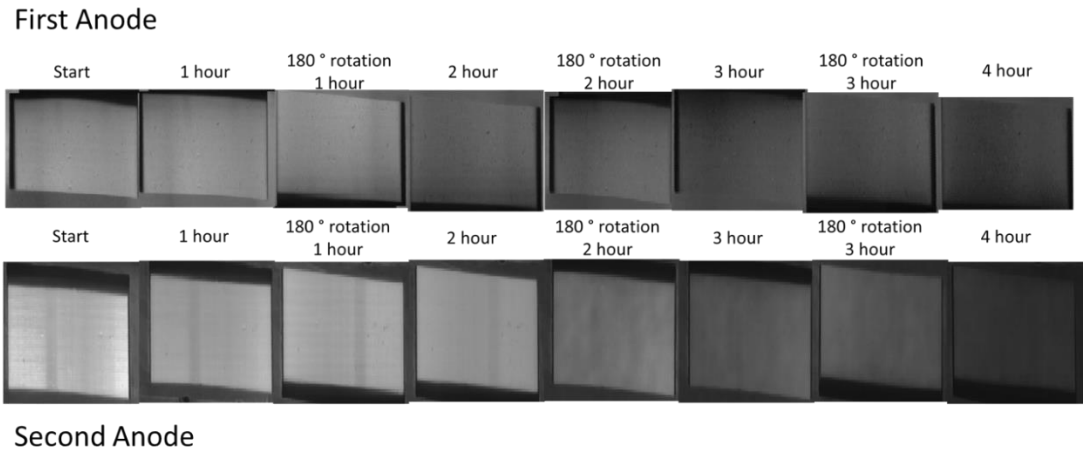

Figure 708. Processed images taken during anode layer deposition at the start and end of each continuous section all rotated to be in the same orientation and cropped to the area of interest for the first anode (top) and the second anode (bottom)

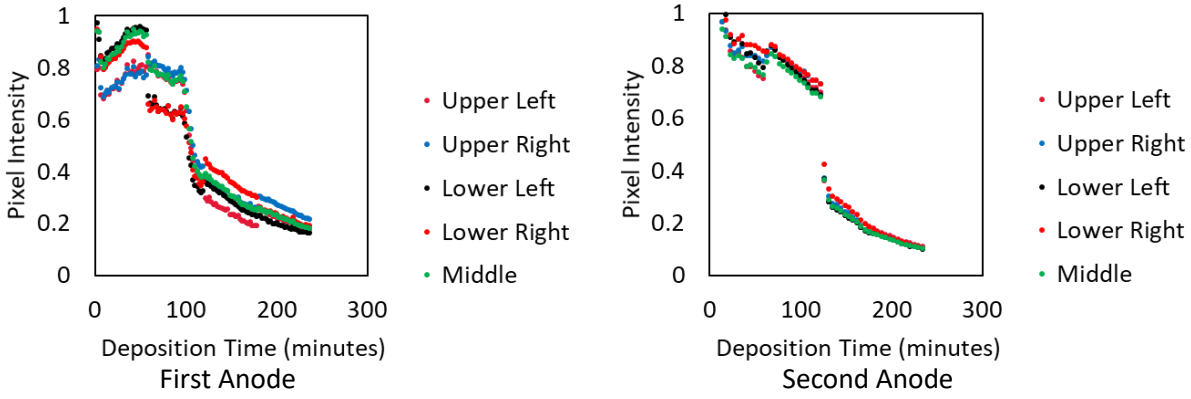

Figure 719. Raw intensity of the anode during the entire deposition in 4 quadrants and the middle, discrete movements can be seen around time 60, 120, and 180 minutes where the unit was rotated for the first anode (left) and the second anode (right)

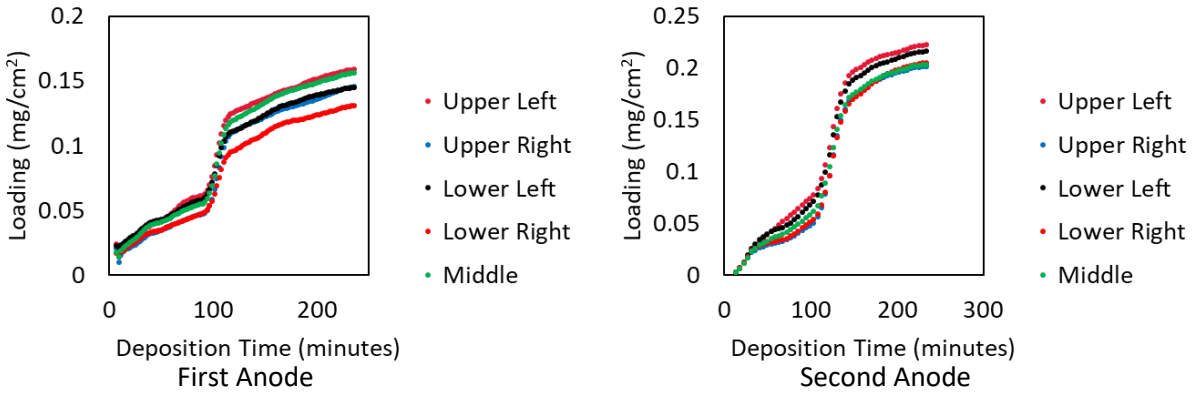

Figure 710. Processed intensity converted into loading of the anode during the entire deposition in 4 quadrants and the middle for the first anode (left) and the second anode (right)

4.7. System Performance Evaluation

ICP analysis of the calibration runs were collected in 13 areas and the loadings compared to the optical measurements. The average loading from the ICP was used to modify the slope of the optical calibrations and the 13 spots loading determined and compared as shown in Figure 731173 for the anode and in Figure74 for the cathode. The optical loadings appear to have good agreement when the rotation and background is taken into account, within 0.03 mg Pt/cm^2 or Ir/cm^2, just like in the static evaluations.

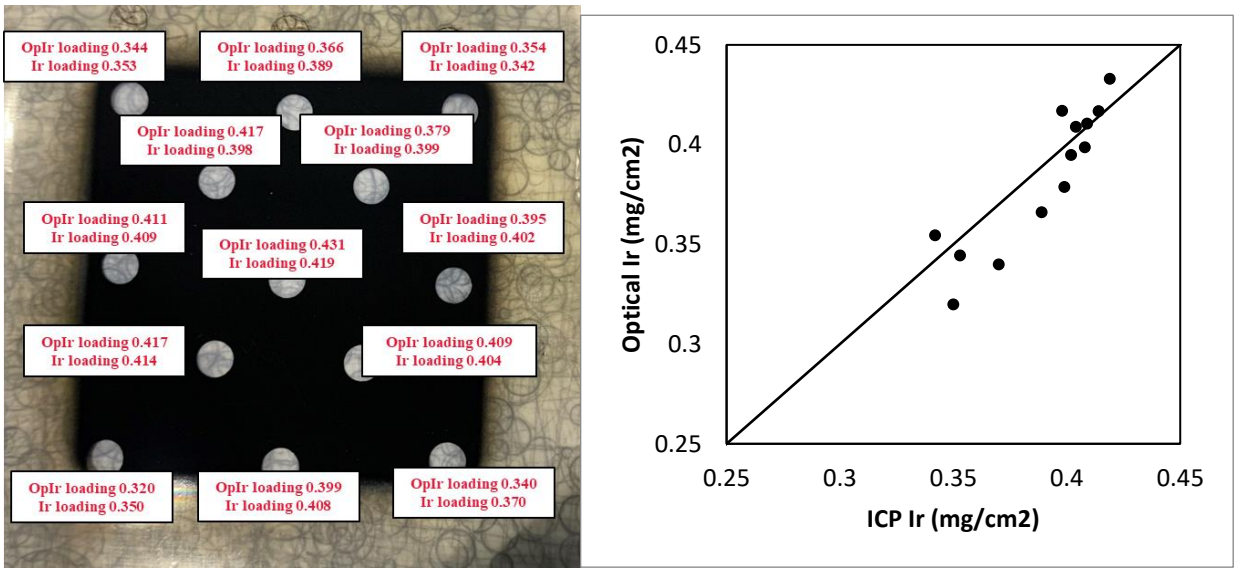

Figure 7311. Image of the location data from ICP and Optical Ir loading (left) and parity plot (right) of the anode

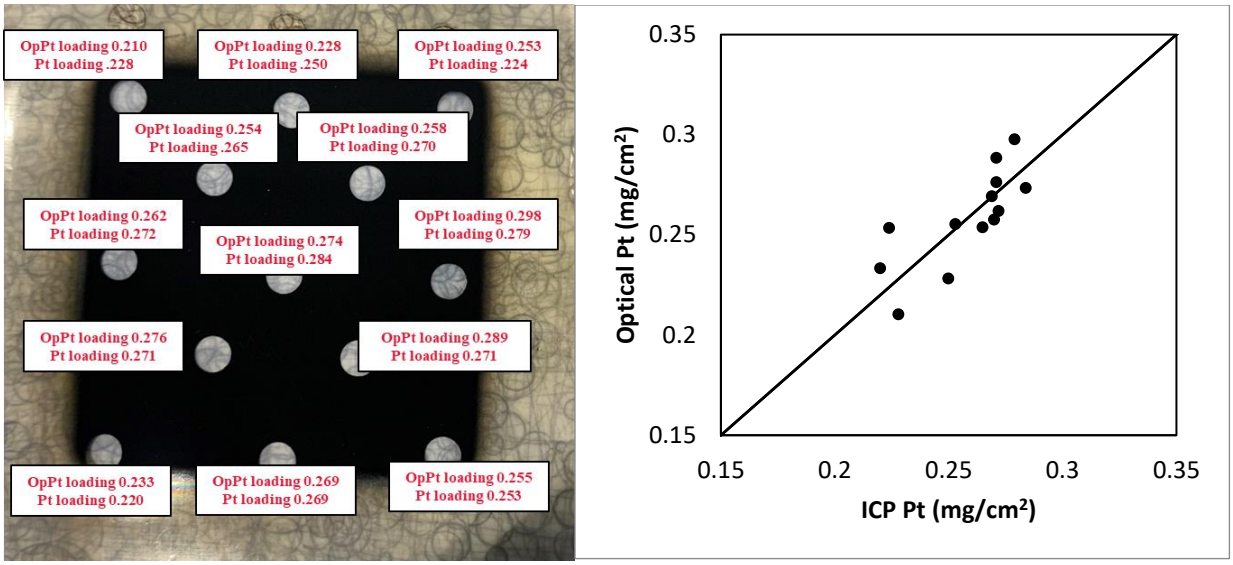

Figure74. Image of the location data from ICP and Optical Pt loading (left) and parity plot (right) of the cathode

4.8. Real-time Operation –Features and Loading

All features and analysis were implemented in real-time with a mode on the optical quality control setup to inform the system of what part is currently being fabricated and what orientation it is in. The method for this is a drop-down menu that has options that include recombination layer – platinum, recombination layer – membrane, anode – iridium oxide, cathode – platinum. Then a button to push when the part is rotated. This allows for the software to track that the top left corner has been rotated to the bottom right corner and keep track through the deposition process. The loading is then built throughout the entire run by comparing each image to the former, instead of processing each image relative to an initial background. This user interface is shown in Figure *12*75.

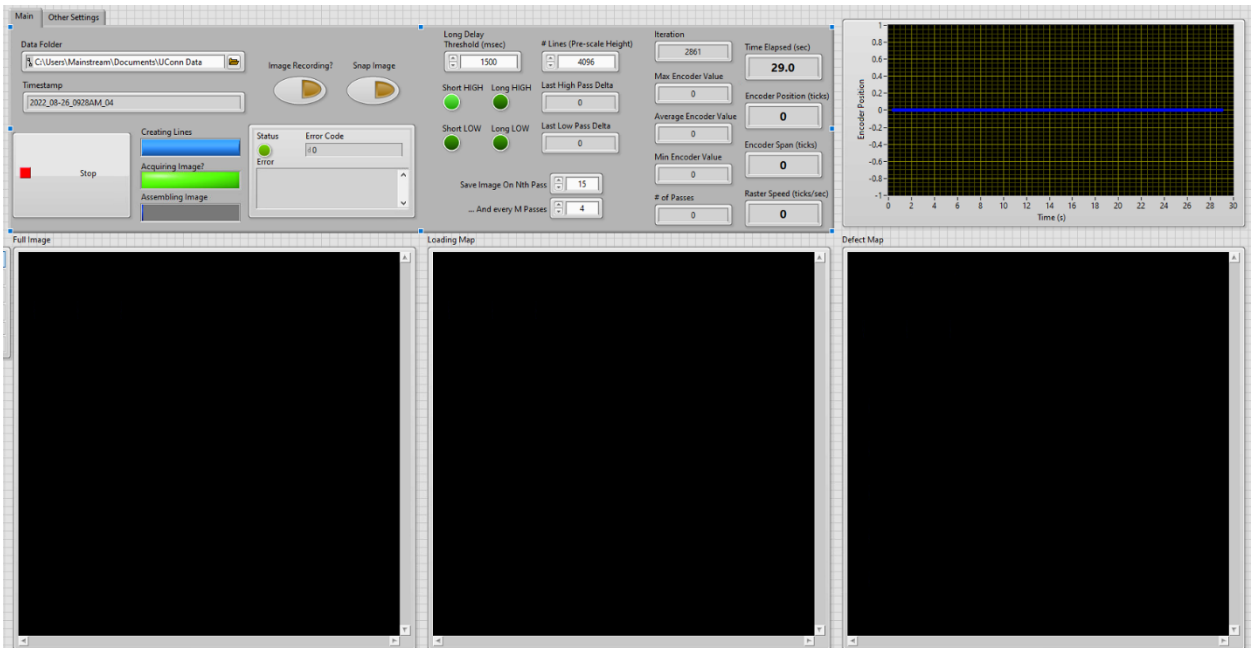

Figure 125. Quality Control User Interface

Summary

Mainstream Engineering developed and installed a quality control system to determine catalyst loading and defects in real-time during component fabrication using reactive spray deposition technology. Numerous in-place real-time measurement challenges were overcome, and images of components were collected and processed during a run. These cause issues with standardization and clear image collection, but modifications enabled clear images to be used for analysis. Calibrations from static samples were successfully translated and demonstrated a loading calibration to within 0.03 mg_{Ir}/cm^2 or mg_{Pt}/cm^2 and defects greater than 250 µm at ± 50% nominal catalyst loading are identifiable at the full-scale and speed. All milestones related to the optical quality control system have been successfully met.

5. In-situ laser diagnostics

In addition to the above reported research and development activities, in the frame of this project, the UConn team developed an advanced laser system for *in-situ* diagnostics of the nanoparticles size and composition during their fabrication by the RSDT. This unique system is integrated with the scaled up RSDT 2 setup and allows to study the relationship between the platinum and iridium oxide structure, particle size, and particle density as a function of the location in the flame environment, the metal precursor concentration, and equivalence ratio. The results of this investigation have been summarized in a journal paper that just was accepted for publication in journal of Combustion and Flame[9]

Figure 76 shows a schematic of the setup implemented to perform *in-situ* Laser measurements in the RSDT flame. A Q-switch Nd-YAG laser (Quanta-Ray Lab-170-10, Spectra-Physics), generates a 10 Hz pulsed beam (532nm) with 8 ± 2ns duration whose 8 mm core of approximately uniform fluence is selected by an iris. A half-wave plate (10RP12-16, Newport) and a polarizer (86-710, Edmund) attenuate the beam. A beam sampler (BSF20-A, Thorlabs) diverts a fraction of the attenuated beam to a pyroelectric sensor (ES120C, Thorlabs) connected to an oscilloscope (MSO2024B, Tektronics) to measure the measurement pulse energy. The timing of the laser pulse is monitored by a photodiode with a time response of 1 ns (SM05PD2B, Thorlabs), detecting a spurious diffuse reflection of the beam sampler.

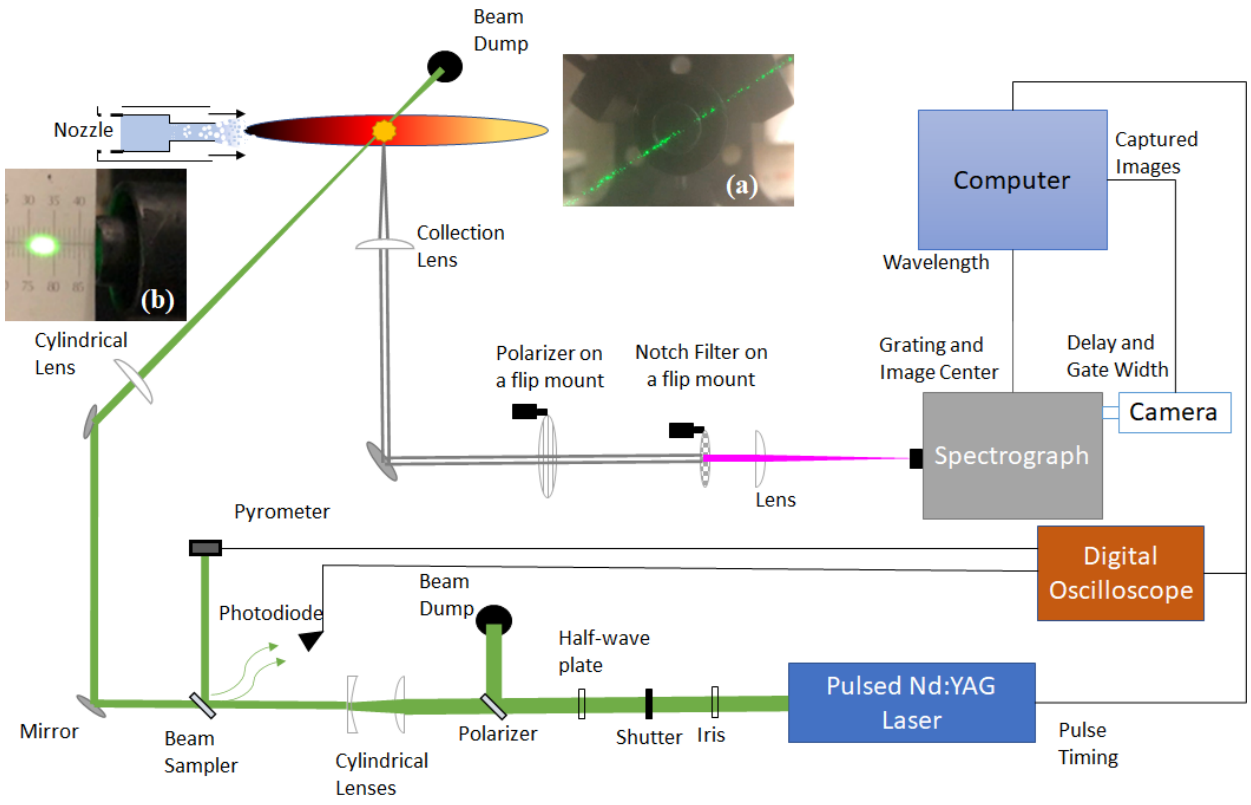

Figure 76. Schematic diagram of the optical layout with insets showing the direction (inset a), position (insets a-b), and the cross-section (inset b) of the laser beam at the measuring point relative to the fuel jet nozzles (and, when installed, the LS calibration nozzles).

An optical train composed of a plano-convex and a plano-concave cylindrical lens with a 400 mm focal length (FL) reduces the size of the beam along one axis orthogonal to the propagation direction, while a 1000 mm FL plano-convex cylindrical lens, installed 750 mm from the measuring point, partially focuses the beam along the orthogonal axis. A set of mirrors redirect the beam to the measuring point upward at a 35-degree angle from the horizon (Figure 76(a)) and horizontal polarization. As a result, and by design, the beam cross-section at the measuring point is shaped into an ellipse with diameters of 3.75 mm along the jet nozzle (and polarization) axis and 2 mm along the radial direction (Fig. 76(b)). The size and shape of the illuminated measuring volume are selected as a compromise between the desired spatial resolution of the measurements and the need to lower the illumination fluence and minimize the consequent possible measurements artifacts (i.e., partial ablation of the nanoparticles) while using the largest possible pulse energy to maximize the acquired signals. The insets of Fig. 76 depict the position of the laser beam relative to the auxiliary double nozzle.[9]

The emission of light stimulated by the laser illumination is collected in the vertical plane (orthogonal to the laser polarization and at a 35-degree angle from the incident beam) by an achromatic (plano-convex) spherical lens with 400 mm FL (PAC090, Newport). The collected light can be filtered by a polarizer (20LP-VIS-B, Newport) and a 532 nm notch filter (86-130, Edmund) mounted on flip mounts before being focused with another achromat (plano-convex) spherical lens (400 mm FL) into the entrance slit of the spectrograph (IsoPlane SCT 320, Princeton Instruments). In the spectrograph, the collected light is spectrally resolved using a 600 groove/mm

grating and refocused to be detected by a 1024 x 253-pixel Gen III Intensified-CCD camera (PI-MAX4, Princeton Instruments) triggered 5 ns before the laser illumination using a pulse delay generator (DG535, Stanford Research Inc) connected to the laser Q-switch signal, and fast gated through the LightField software (LightField 4.0, Princeton Instruments).[9]

In the time frame of the project, we collected experimental data and refined our methodology for improving the accuracy of the results while extracting more information about the measured nanoparticles. First, we established a robust and repeatable methodology for analysis of high-angle annular dark-field scanning transmission electron microscopy (HAADF-STEM) images that were collected at different magnifications. Second, we fitted the results for the particle size distributions (PSDs) estimated from the STEM images and retrieved additional information for the nanoparticles size distribution. Third, we reprocessed the data accounting for both Pt and PtO_2 nanoparticles formed in the RSDT flame and compared these results with the results derived from the HAADF-STEM images. We also replaced the grating 2400 g/mm of the spectrograph with a 600 g/mm grating to increase the Raman signal and investigated as collected spectrum during the IrO_x deposition

Reviewing the methodology, we established that each experiment's accuracy and repeatability is evaluated through gas calibration measurements on CO_2, N_2, and He, before and after each experiment. The average accuracy of the scattering signal calibrations before and after the flame experiments is 95%, as confirmed by comparison with the scattering cross-section of CO_2, N_2, and He reported in the literature.

Once the repeatability and the accuracy of the method were established, we performed the in-situ measurements in the RSDT flames. We tested three different RSDT configurations at which the metal precursor was dissolved in the fuel, or the corresponding blank flame was fueled by the solvent alone. The first configuration utilized a fuel solution composed of 250 mL of xylene, 125 mL of diethylene glycol monoethyl ether (DGME), 92.87 g of propane, and 3.1 g of iridium acetylacetonate (or without the metal precursor in the case of the blank flame) to fabricate iridium nanoparticles (Ir-Type 1/Ir-Blank 1). The spraying nozzle temperature was 65 °C, and the fuel solution flow rate was adjusted at 8 mL/min. The second and the third RSDT configurations included a fuel solution containing 600 g of xylene, 200 g of acetone, 170 g of propane, and 5.1 g of platinum acetylacetonate (or without the metal precursor in the case of the blank flames). The spraying nozzle temperature was 190 °C, and the fuel solution flow rate was either 4 mL/min (Pt-Type 1/ Pt-Blank 1) or 7 mL/min (Pt-Type 2/Pt-Blank 2). The laser light scattered from the synthesized nanoparticles, $\overline{Q_{vv,p}}$, is calculated by subtracting the calibrated signal of the blank flame from the calibrated signal measured in the corresponding flame containing the metal precursor. Light Scattering (LS) measurements are collected for all flames at distances L, particularly at 150 mm, 175 mm, 200 mm, 250 mm, and 300 mm from the primary nozzle.

The fluence is defined as the laser pulse energy per unit area. The laser pulse energy is measured through a pyrometer (ES120C, Thorlabs) connected to an oscilloscope (MSO2024B, Tektronics), and it is recorded from the oscilloscope software (TekBench, Tektronix). All the measurements are collected for laser fluence lower than 200 mJ/cm^2, which we established in previous experiments as the upper limit for fluence-independent measurements.

The determination of the nanoparticle (light scattering equivalent) diameter associated with the measured $\overline{Q_{vv,p}}$, requires the knowledge of the volume fraction of the particles, $f_{v,p}$. An initial

estimate of $f_{v,p}$ can be made at the tip of the flame through a mass balance, assuming the precursor concentration at this point is the same as the precursor concentration in the pump. The variation of $f_{v,p}$ downstream the flame is measured by implementing Laser-Induced Incandescence (LII) measurements. In LLI, the laser is used to heat the particles at a high temperature so that the particles emit intense broadband light untiled they cool back to the surrounding gas temperature. Since heat transfer drives the timescales of the cooling process, we need to tune the camera gate times to collect all the emitted light from the particles. The time and the spectrally integrated value of the LII signal, $\overline{S_{LII}}$, is proportional to the $f_{v,p}$, (Eq.1).

$$\overline{S_{LII}} = \mathrm{C} \cdot \overline{\mathrm{f_{v,p}}} \tag{1}$$

During each laser experiment, samples of the synthesized particles are collected from the flames at distance from the nozzle L=250 mm. High-Angle Annular Dark-Field Scanning Transmission Electron Microscopy (HAADF-STEM) is used to capture high-resolution images of the collected particles, and ImageJ software is used to measure the particle size distributions (PSD) of the collected samples. Image analyses are performed on images from different parts of the sample with a small field of view ($4.2 \cdot 10^{-3} \mu m^2$), one image with an intermediate field of view ($8.3 \cdot 10^{-3} \mu m^2$), and other images with a large field of view ($122.5 \cdot 10^{-3} \mu m^2$). Image analysis involves the application of multiple Gaussian filters, brightness and contrast adjustments, and sharpening functions to allow for an easy and accurate determination of the particle edges. The comparison of the determined edges with the raw images confirms that the vast majority of the particles are accurately tracked by the implemented image analysis procedure, as shown in Figure 77. The automated particle detection function of the ImageJ software avoids any bias introduced from the manual analysis and measures the projected area, A_p, of nanoparticles larger than $0.196\ nm^2$ (i.e, d> $0.5\ nm$). The diameter of each detected nanoparticle is inferred under the assumption of spherical shape (i.e., $d = \sqrt{\frac{4}{\pi} A_p}$). The minimum diameter is set at $0.5\ nm$, because the critical size of the Pt nanoparticles at the edge of the flame is $0.3\ nm$, and we added $0.2\ nm$ to account for possible condition fluctuations at the edge of the flame. The samples collected from the Ir flame will be discussed in a separate paper that we are currently writing.

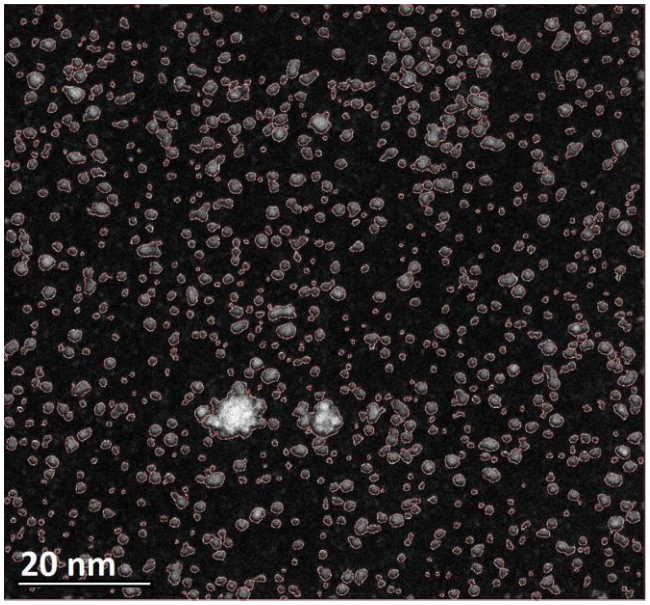

Figure 77. HAADF-STEM image of nanoparticles sampled in the Pt-Type 2 flame with the red line edges highlighting the nanoparticles identified and sized by the semi-automated ImageJ analysis procedure.

Figure 78 shows the excess signal of Pt-Type 1, Pt-Type 2, and Ir-Type 1 in terms of scattering coefficient (cm^{-1} sr^{-1}) as a function of the distance from the nozzle L. The excess signals of Pt-Type 1 and Pt-Type 2, presented in Figure 78 are the average signals of data collected on various deposition events. In the case of Ir-Type 1, the excess signal is the average of data collected from RSDT depositions performed at two different days. The value of $\overline{Q_{vv,p}}$ decreases at increasingly larger L in all (Pt-Type 1, Pt-Type 2, Ir-Type 1) flames due to the generated nanoparticles mixing and dilution into the surrounding gasses that cause the decrease in their concentration.

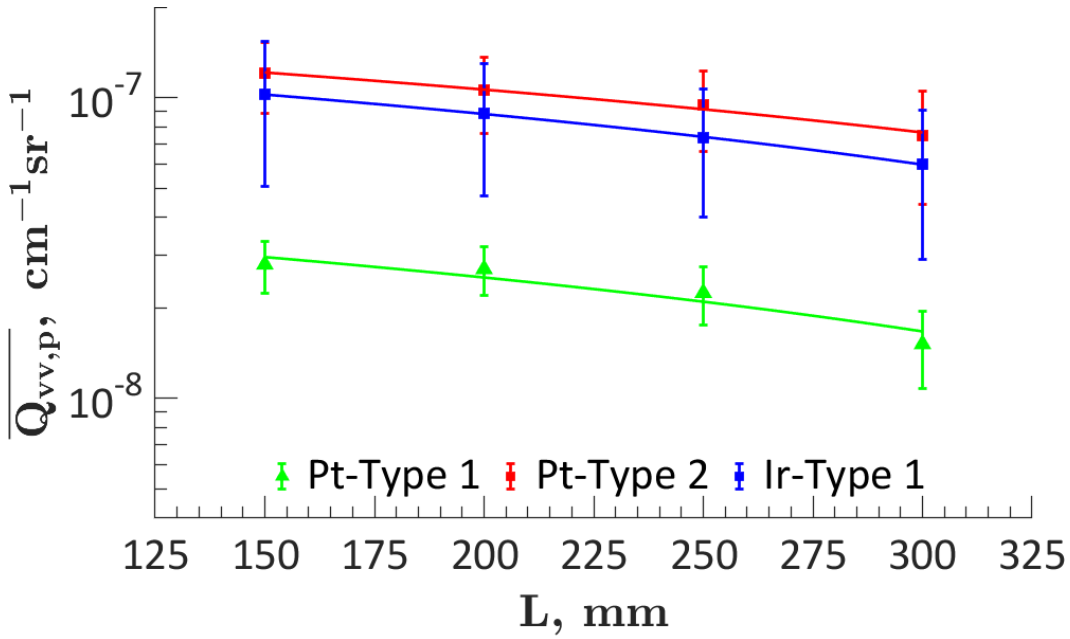

Figure 78. Excess scattering coefficient associated with the nanoparticles synthesized in the three investigated RSDT setups as a function of the distance from the nozzle.

Figure 79 presents the typical laser-induced spectral emission measured in the Pt-Type 2 and Pt-Blank 2 at L=150 mm. The products of the Pt-Blank flame cause a laser-induced emission between 565 and 590 nm and 600 nm and 615 nm. The blank flame emission includes the Stokes Raman scattering of the gas molecules (e.g., that of O_2, H_2, H_2O, CO_2, and N_2) and, possibly, fluorescence and Raman scattering of other carbonaceous flame products. We remove these undesirable signals by subtracting the spectrum measured in the blank flame from that measured at the same position in the corresponding metal precursor doped flame.

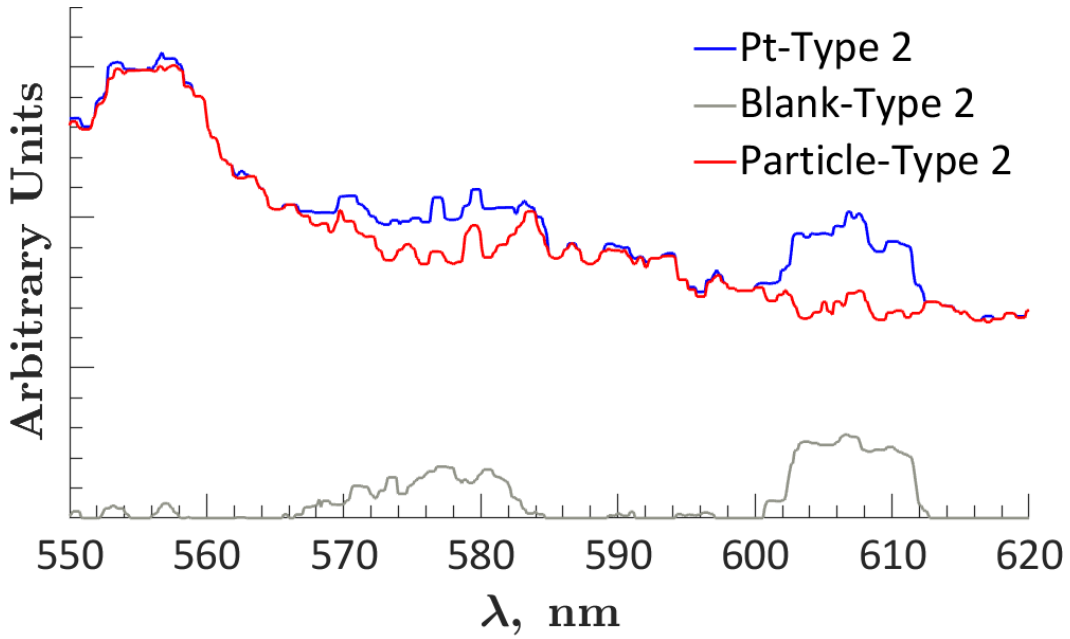

Figure 79. Laser-induced emission spectra of the Pt-Type 2 (blue line) and Pt-Blank 2 (gray line) flames at L=150mm measured with a fluence of 255 mJ/cm^2 and a gating time of 250 ns. The red line highlights the LII emission spectrum of the synthesized Pt nanoparticles obtained by subtracting the emission spectrum of Pt-Blank 2 from that of the Pt-Type 2 flame.

Earlier in the program, we performed LII measurements on the Pt-Type 1 and Pt-Type 2 flames using three values of camera gating times, namely, 150 ns, 250 ns, and 350 ns (Figure 80). We found that the signal measured with a gating time of 150 ns is approximately two times smaller than that measured with 250 ns and 350 ns, indicating that only a part of the LII signal was collected. In the investigated conditions, the relative signal at different positions in flames is independent of the value of the gating time. However, we perform measurements with the two longer gating times (250 ns and 350 ns) for a higher signal-to-noise ratio.

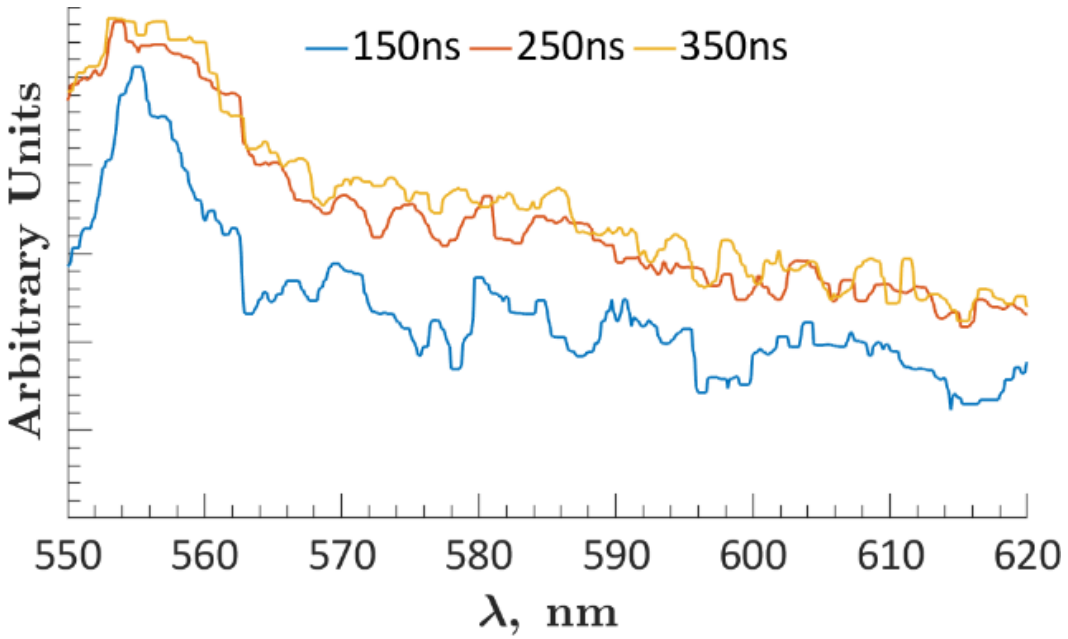

Figure 80. LII spectra measured in the Pt-Type 2 flame at L=150 mm with a fluence of 255 mJ/cm^2 and gating times of 150 ns, 250 ns, and 350 ns.

Figure 81 presents the average background-subtracted LII spectra emission of Pt nanoparticles in both the Pt-Type 1 and Pt-Type 2 flames as a function of L. It is seen that the maximum of the nanoparticle LII emission spectra present at 150 mm, disappears because it shifts toward shorter wavelengths at progressively larger L, eventually exiting the imaged spectral interval at the largest distances. This observation implies that Pt nanoparticles withstand progressively higher vaporization temperatures following the laser irradiation and/or modify their emissivity as they undergo aging into the flame. One can speculate that the enhancement in the thermal resistance and/or change in emissivity of the nanoparticles underly a structural change such as the conversion between two crystalline and/or amorphous phases. Figure 81 also shows that the intensity of the LII emission decreases as the nanoparticles travel downstream the flame. The decrease is due to the turbulent and diffusive mixing of the flame products with the surrounding gasses while they travel downstream, which is characteristic of the jet flame configuration and involves diluting the synthesized Pt nanoparticles at increasing L.

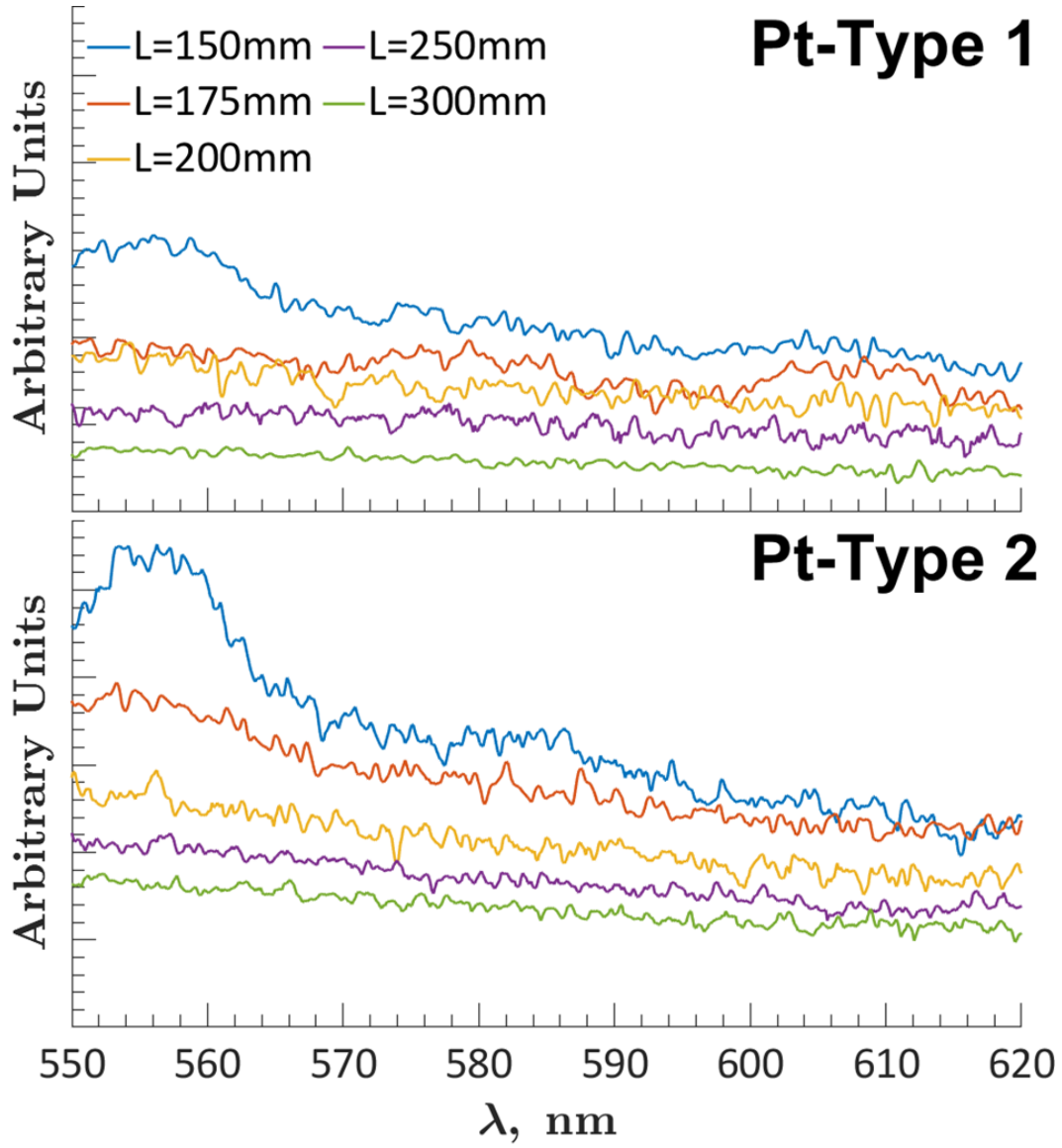

Figure 81. Average LII emission spectra of Pt nanoparticles measured at different distances from the nozzle L (see legend) in the Pt-Type 1 (top panel) and Pt-Type 2 (bottom panel) flames.

The decrease of the $f_{v,p}$ is quantified with Eq.1 from the $\overline{S_{LII}}$ calculation via spectral integration of the measured nanoparticle LII emission. The integration is performed in the three wavelength intervals (between 550 nm -565 nm, 590 nm -600 nm, and 615 nm – 620 nm) unaffected by the laser stimulated emission of the blank flame. These spectral intervals are chosen to minimize the noise from the un-subtracted light emissions not associated with Pt nanoparticles.

Figure 82 presents the measured $f_{v,p}$ of the two Pt flames normalized over its value at the tip of the flame $f_{v,p}(L_{edge})$ as a function of the non-dimensional distance $\frac{L-L_{edge}}{L_{edge}}$. The choice of the non-dimensional distance was performed to account for the different lengths of the luminous zones

of the two Pt flames (Ledge= 125 mm and 145 mm for Pt-Type 1 and Pt-Type 2 flames, respectively). A fitting of an exponential curve is performed by minimizing the mean square of the difference between fitted and experimental results, considering $\overline{S_{LII}}$ by integration in all three wavelength intervals; however, the results are essentially the same if one considers the three-wavelength intervals individually. The fitting curve provides a unified equation that can estimate the $f_{v,p}$ a priori at any distance for any RSDT configuration at least as long as the stoichiometry of the RSDT reactants is not changing dramatically.

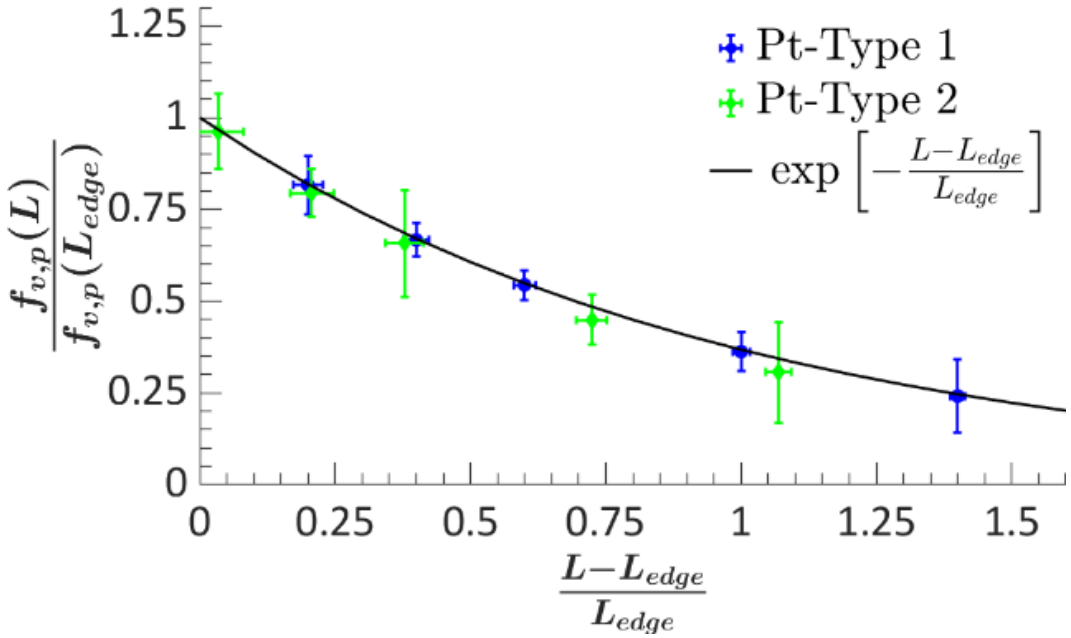

Figure 82. Exponential decay of the normalized measured volume fraction of Pt nanoparticle as a function of the non-dimensional distance from the spray nozzle $\frac{L-L_{edge}}{L_{edge}}$ in the Pt-Type 1 and Pt-Type 2 flames.

In addition, we analyzed the collected data assuming that the produced particles are PtO_2 and compared the results with the results of the Pt particle assumption. Figure 83 shows the measured Pt-Type 1 and Pt-Type 2 nanoparticle $\overline{d_{6,3}}$ as a function of L, assuming that the produced particles from the flame are only Pt particles or only PtO_2 particles. The results reveal that the assumption of only PtO_2 particles reduces the measured particle sizes for both Pt-Type 1 and Pt-Type 2 flames. Additionally, the higher flow rates of the Pt-Type 2 flame reactants compared to that of the Pt-Type 1 flame result in synthesizing Pt nanoparticles with significantly larger light scattering equivalent sizes throughout the flame. Moreover, the nanoparticles' diameter increases as they are convected downstream at larger distances L, due to ongoing coagulation. The increase is very mild in both flames but slightly more pronounced in the Pt-Type 2 than the Pt-Type 1 flame. In the case of the Ir-Type 1 flame, we assumed that the $f_{v,p}$ follows the same exponential decay we discovered for the Pt flames, with L_{edge}=150 mm, and that the produced particles are Ir particles. Following

the Pt flames, the Ir-Type 1 nanoparticles slightly increase their sizes as they age while being convected downstream of the flame.

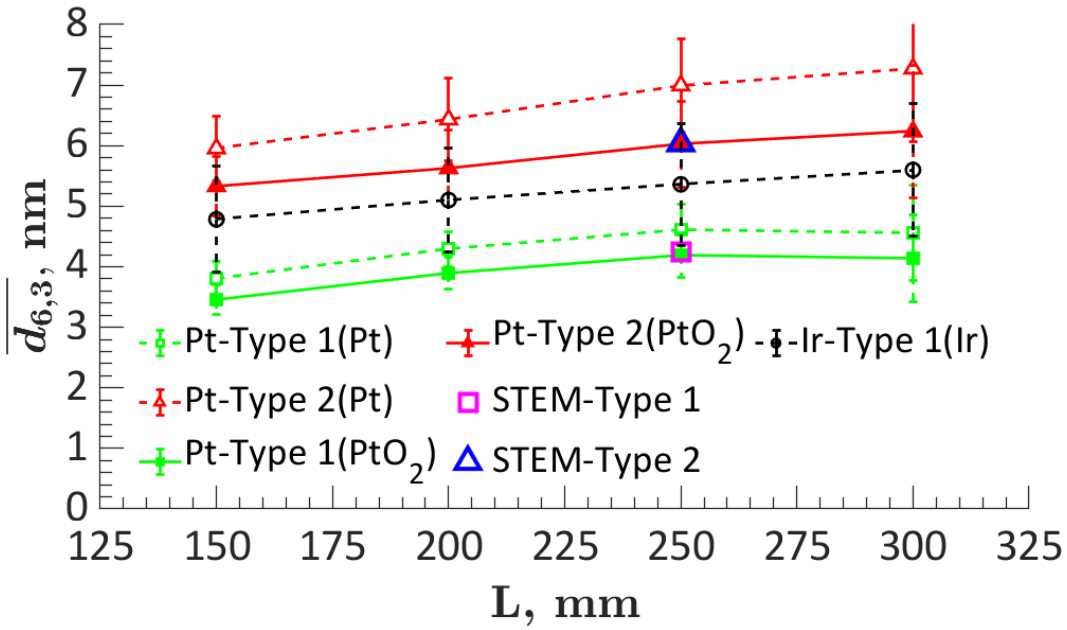

Figure 83. Axial profile of the nanoparticle $\overline{d_{6,3}}$ in the Pt-Type 1, Pt-Type 2, and It-Type 1 flames as a function of *L* assuming only Pt/Ir nanoparticles (dashed line) and only PtO_2 (solid line), and STEM-HAADF results (hollow markers).

To further investigate the results of the laser measurements, we performed HAADF-STEM microscopy image analysis of Pt nanoparticles collected in both Pt flames at L=250 mm using the methodology described above. In Figure 83, the nanoparticle $\overline{d_{6,3}}$ measured from microscopy is presented to correlate with the laser results under the assumptions of only PtO_2 particles. Specifically, the laser equivalent diameter $\overline{d_{6,3}}$ assuming the presence of only PtO_2 particles, at L=250 mm for Pt-Type 1 is 4.19 ± 0.37 nm and for Pt-Type 2 is 6.02 ± 0.7 nm, while the $\overline{d_{6,3}}$ diameter measured from microscopy for Pt-Type 1 is 4.25 nm and for Pt-Type 2 is 6.04 nm.

Figure 84 presents the histograms of the particle size distributions of the samples collected in the Pt-Type 1 and Pt-Type 2 flames. The nanoparticles synthesized in both flames show a bimodal particle size distribution (PSD) with the first mode located near 0.95 nm and the second one at approximately 6.05 nm and have very similar shapes.

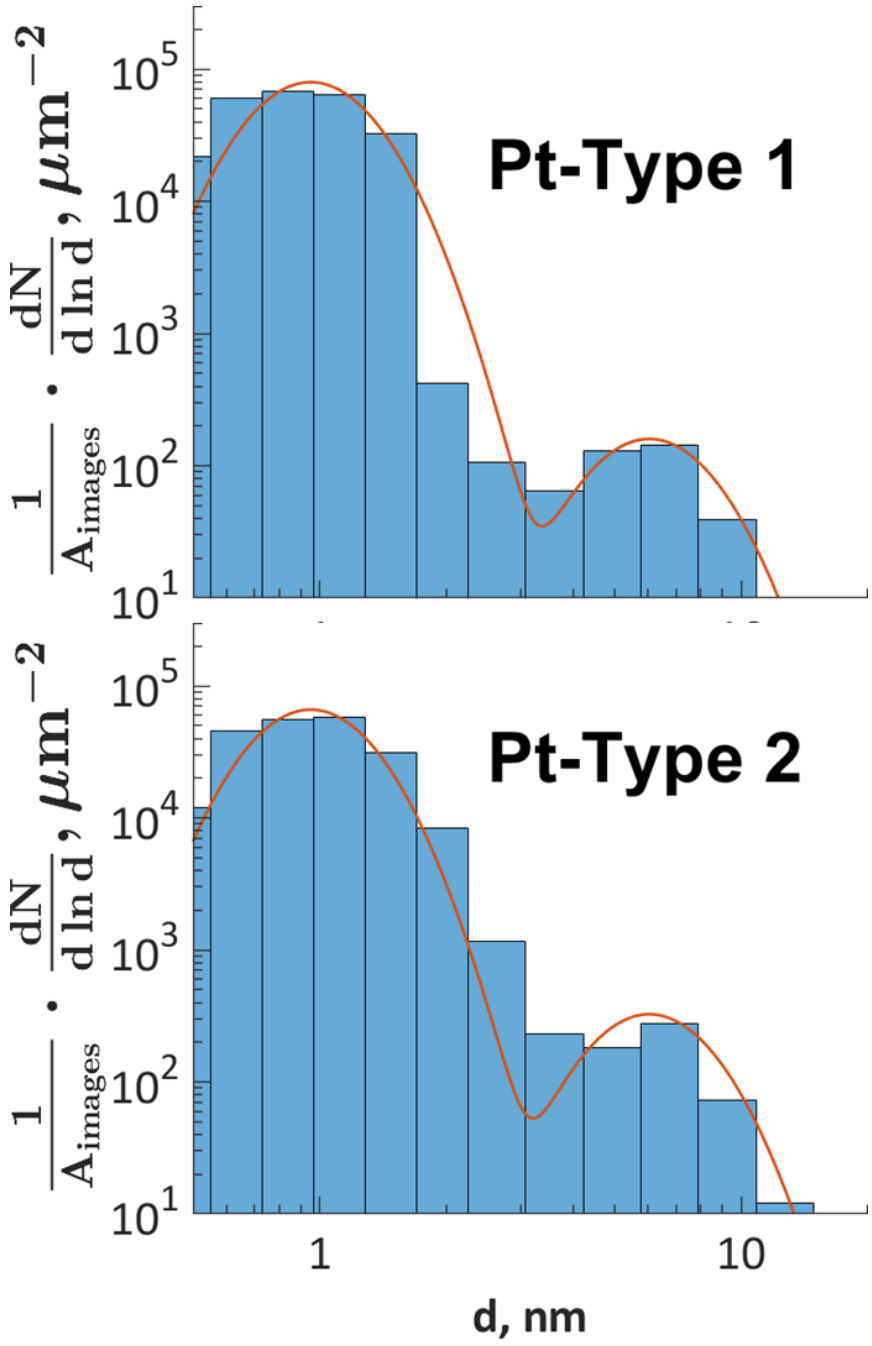

Figure 84. Particle size distribution (PSD) of nanoparticles collected at L = 250 mm in the Pt-Type 1 (top panel) and Pt-Type 2 (bottom panel) flames obtained via HAADF-STEM microscopy image analysis. The orange line shows the fitting of the measured PSD performed using the sum of two lognormal distributions with fixed σ=1.4 and modal diameters of 0.95nn and 6.05nm, respectively.

Given the similar bimodality of the two PSDs, we implemented the fitting of the results shown with a red line in the figure using the sum of two identical lognormal distributions weighted by considering the fraction of the total number of the particles belonging to the second mode compared to the total, n_2/n_p. The lognormal modes are chosen to have the same σ=1.35 typical of freshly nucleated particles and modal diameters of $d_{gm,1} = 0.95\,nm$ and $d_{gm,2} = 6.05\,nm$

selected by calculating the median diameters considering only the particles either smaller or larger than 3 nm in the HAADF-STEM imaged population. The values of $n_{2,Pt2}/n_{tot,Pt2}(L = 250\ mm)$ and $n_{2,Pt5}/n_{p,Pt5}(L = 250\ mm)$ are determined to minimize the error in reproducing the values of the diameters $\overline{d_1}$, $\overline{d_2}$, $\overline{d_3}$, $\overline{d_4}$, $\overline{d_5}$, $\overline{d_6}$, (with $\overline{d_n} = \sqrt[n]{\overline{d^n}}$) measured via image analysis and the values of the two Size Distribution Functions (SDFs) in Figure 85. Eq. 2 presents the sum of the two lognormal distributions.

$$\frac{d(n)}{\mathrm{d}\,(\ln d)} = \frac{1}{\ln \sigma\sqrt{2\pi}}\left\{(n_p - n_2)\exp\left[-\frac{\left(\ln d - \ln d_{gm,1}\right)^2}{2\cdot \ln \sigma}\right] + n_2 \exp\left[-\frac{\left(\ln d - \ln d_{gm,1}\right)^2}{2\cdot \ln \sigma}\right]\right\} \quad (2)$$

Since the same two modes can reproduce the experimental results in the two flames at a position that corresponds to significantly different residence times, one can assume that the same modes would be able to mimic the SDF throughout both flames if one can determine $n_{tot}(L)$ and $n_2(L)$ as a function of L. The results of laser diagnostics readily provide the needed information because the values of $\overline{f_{v,p}} = \overline{n_p}\cdot\frac{\pi}{6}\overline{d^3}$ and $\overline{d_{6,3}}$ of the interpolated SDF are univocally determined by $n_{tot} = n_p$ and n_2 when the values of $d_{gm,1}$, $d_{gm,2}$ and σ are fixed and given.

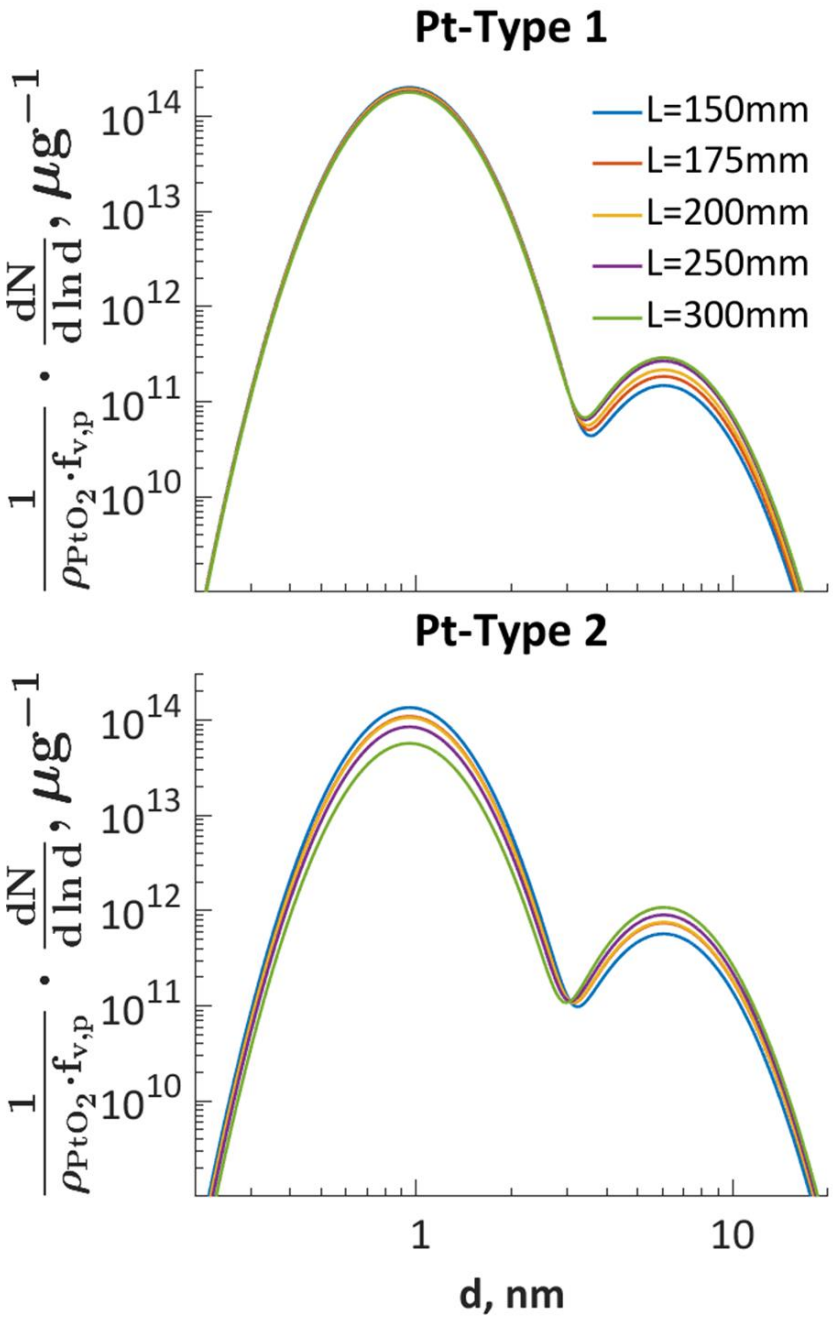

Figure 85. SDFs per unit mass of Pt nanoparticles synthesized in the Pt-Type 1 (top panel) and Pt-Type 2 (bottom panel) flames. The results are inferred from the results of laser diagnostics under the assumption of a bimodal lognormal distribution whose parameters ($d_{gm,1}$, d_{gm2}, and σ in Eq. 2) are inferred from HAADF-STEM image analysis.

In early-stage measurements of the Ir-Type 1 flame at a distance L=150 mm with a laser fluence of 281 mJ/cm^2, we detected a double Raman peak at 1815 cm^{-1} and 1829 cm^{-1} (Figure 86). To identify the Raman peak, we run density functional theory (DFT) calculations of ten candidate species products of the flame. The DFT results limited the candidates to the three most probable groups but unfortunately, we were not able to find Raman peaks of these candidates in the literature that are the same as the detected peak. The team continues with the efforts to achieve a higher signal-to-noise ratio of the peak by increasing the laser beam intensity, using a different grating, and maintaining the spectrograph, while exploring the literature for possible matches.

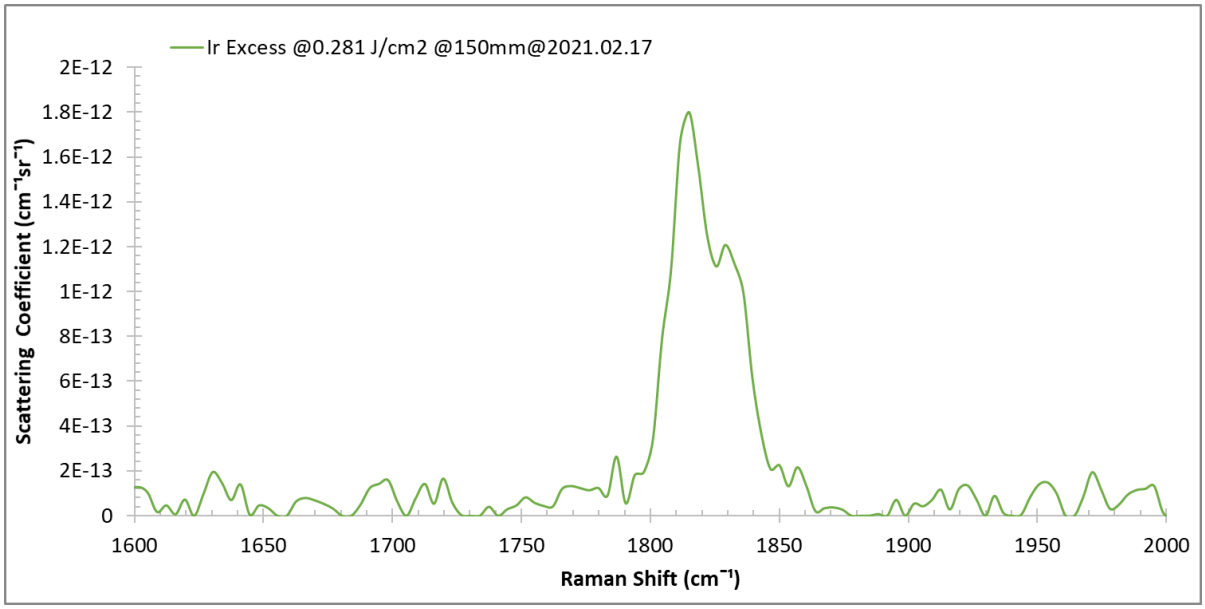

Figure 86. Raman spectrum of the excess light scattered by the iridium nanoparticles in terms of scattering coefficient measured with a laser fluence of 281 mJ/cm^2 at a distance of 150 mm from the nozzle.

Summary

In this project, we implemented laser diagnostics in the RSDT system and performed *in-situ* characterization of various platinum and iridium nanoparticles smaller than 10 nm, synthesized in RSDT flames at different deposition conditions. The combination of laser scattering (LS) and laser-induced incandescence (LII) enabled the measurement of the nanoparticle volume fraction, sizes, and (distribution of) number concentrations within the flames. In addition, we established a robust, repeatable methodology for analyzing the HAADF-STEM images with various magnifications. Also, we processed the data assuming the formation of PtO_2 instead of Pt nanoparticles from the flames. The results from HAADF-STEM microscopy advocate the PtO_2 assumption. We fitted a bimodal lognormal distribution in the microscopy results, and successfully calculated the PSDs profiles at various distances from the burner by correlating the laser with the microscopy measurements.

The analysis of the results for the RSDT fabricated Pt nanoparticles led to the following principal findings.[9]

1. The change in the shape of the measured LII spectra as the nanoparticle age in the flame between 150 mm and 300 mm from the nozzle indicates an increase in their vaporization temperature achieved as a result of the laser irradiation and/or change in their spectral emissivity (e.g., Armstrong exponent). This finding highlights possible changes in phase and/or degree of oxidation of the nanoparticle constituents.
2. The sizes of nanoparticles increase very mildly at increasing distances from the fuel nozzle, whereas their volume fraction decreases fourfold because of turbulent diffusion mixing of the flame products with the surrounding gasses. The decay of volume fraction can be inferred in a family of nanoparticles synthesizing flames with an exponential fitting mimicking the dilution of the flame products observed experimentally.
3. Complementary ex-situ analysis of High-Angle Annular Darkfield Scanning Transmission Electron Microscopy (HAADF-STEM) images of selected nanoparticle samples collected via thermophoresis validated the laser diagnostic results and allowed to infer the size distribution functions of the synthesized nanoparticles *in-situ* throughout both flames. The SDFs are composed of two lognormal modes centered at approximately 1 nm and 6 nm, with the relative number of nanoparticles belonging to the larger mode being sensitive to the RSDT flame flowrates.
4. The synthesized Pt nanoparticles appear to grow at rates that are orders of magnitude slower than that expected because of the collision rate of non-interacting Brownian nanoparticles. The mechanisms that cause low values of the coagulation efficiency observed experimentally should be further investigated.

The integration of the *in-situ* laser diagnostics system along with the *in-line* optical quality control system within the RSDT that has been achieved and demonstrated in this project, is an example for possibility of designing and building advanced manufacturing technologies that can meet the requirements of the future manufacturing. The RSDT is and advanced manufacturing technology that combines the catalysts synthesis and large scale CCMs fabrication in one step. The RSDT is the only technology that allows fabrication of CCMs for PEMWEs in hours rather than weeks. Staring from chemical precursors the RSDT fabricated CCMs with ultra-low PGM loadings and high activity and durability performance, are ready for assembly in stacks in hours. These advantages, combined with the precise operando control of the particles size, composition, loading, porosity, thickness, and the defects in the catalysts' layers, render this technology as the best candidate for manufacturing of cost effective CCMs for PEMWEs. By using RSDT we successfully met all project's milestones, Go/No-Go decision, objectives, goals, and deliverables.

Acknowledgement

This material is based upon work supported by the U.S. Department of Energy's Office of Energy Efficiency and Renewable Energy (EERE) under the Hydrogen and Fuel Cell Technology Office, Technology Acceleration, award number DE-EE0008427

LEGAL DISCLAIMER STATEMENT

References

1. G. Mirshekari, R.J. Ouimet, Z. Zeng , H. Yu, S. Bliznakov, L. Bonville, A. Niedzwiecki, C. Capuano, K.E. Ayers, R. Maric. High-performance and cost-effective membrane electrode assemblies for advanced proton exchange membrane water electrolyzers: Long-term durability assessment. *Int. J. Hydrogen Energy* **46**, 1526–1539 (2021).

2. J.M. Roller, J. Renner, H. Yu, C. Capuano, T. Kwak, Y. Wang, C.B. Carter, K.E. Ayers, W.E. Mustain, R. Maric. Flame-based processing as a practical approach for manufacturing hydrogen evolution electrodes. *J. Power Sources* **271**, 366–376 (2014).

3. J. M. Roller, S. Kim, T. Kwak, H. Yu, R. Maric. A study on the effect of selected process parameters in a jet diffusion flame for Pt nanoparticle formation. *J. Mater. Sci.* **52**, 9391–9409 (2017).

4. K. E. Ayers, J. N. Renner, N. Danilovic, J. X. Wang, Y. Zhang, R. Maric, H. Yu . Pathways to ultra-low platinum group metal catalyst loading in proton exchange membrane electrolyzers. *Catal. Today* **262**, 121–132 (2016).

5. R.J. Ouimet, A.M. Gado, S Bliznakov, L.J. Bonville, R. Maric. Advanced electrodes for electrochemical energy storage and conversion devices fabricated by reactive spray deposition technology. *Electrochem. commun.* **133**, 107162 (2021).

6. J.M. Roller, R. Maric. A Study on Reactive Spray Deposition Technology Processing Parameters in the Context of Pt Nanoparticle Formation. *J. Therm. Spray Technol.* **24**, 1529–1541 (2015).

7. H. Yu, N. Danilovic, Y. Wang, W. Willis, A. Poozhikunnath, L. Bonvilleb, C. Capuanoc, K. Ayersc, R. Maric. Nano-size IrOx catalyst of high activity and stability in PEM water electrolyzer with ultra-low iridium loading. *Appl. Catal. B Environ.* **239**, 133–146 (2018).

8. Z. Zeng, R.J. Ouimet, L. Bonville, A. Niedzwiecki, C. Capuano, K. Ayers, A.P. Soleymani, J. Jankovic, H. Yu, R. Maric, S. Bliznakov . Degradation Mechanisms in Advanced MEAs for PEM Water Electrolyzers Fabricated by Reactive Spray Deposition Technology. *J. Electrochem. Soc.* **169**, 054536 (2022).

9. E.K. Stefanidis, T.A. Ebaugh, S. Bliznakov, L. Bonville, F. Carbone, R. Maric. Laser Diagnostics to characterize the in-flame growth of Platinum Nanoparticles manufactured by the Reactive Spray Deposition Technology. *Combustion and Flame Journal* (accepted).